

AD-A216 005



# DEVELOP TECHNIQUES FOR ION IMPLANTATION OF PLZT FOR ADAPTIVE OPTICS

R. A. Craig, et al

Battelle  
Pacific Northwest Laboratory  
Richland, WA 99352

November 1989

Final Report

Approved for public release; distribution unlimited.

DTIC  
ELECTE  
DEC 18 1989  
S B D

Weapons Laboratory  
Air Force Systems Command  
Kirtland Air Force Base, NM 87117-6008

89 12 18 0 00

This final report was prepared by Battelle, Pacific Northwest Laboratory, Richland, Washington, under Contract DE-AC06-76RLO 1830, Job Order ILIR8705 with the Weapons Laboratory, Kirtland Air Force Base, New Mexico. Sylvia D. Mancha (AROF) was the Laboratory Project Officer-in-Charge.

When Government drawings, specifications, or other data are used for any purpose other than in connection with a definitely Government-related procurement, the United States Government incurs no responsibility or any obligation whatsoever. The fact that the Government may have formulated or in any way supplied the said drawings, specifications, or other data, is not to be regarded by implication, or otherwise in any manner construed, as licensing the holder, or any other person or corporation; or as conveying any rights or permission to manufacture, use, or sell any patented invention that may in any way be related thereto.


This report has been authored by employees and a contractor of the United States Government. Accordingly, the United States Government retains a non-exclusive, royalty-free license to publish or reproduce the material contained herein, or allow others to do so, for the United States Government purposes.

This report has been reviewed by the Public Affairs Office and is releasable to the National Technical Information Service (NTIS). At NTIS, it will be available to the general public, including foreign nationals.

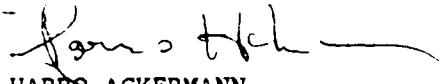
If your address has changed, if you wish to be removed from our mailing list, or if your organization no longer employs the addressee, please notify AFWL/AROF, Kirtland AFB, NM 87117-6008 to help us maintain a current mailing list.

This technical report has been reviewed and is approved for publication

  
SYLVIA D. MANCHA  
Project Officer

  
NICHOLAS R. PCHELKIN  
Chief, Semiconductor Laser  
Technology Branch

FOR THE COMMANDER

  
HARRO ACKERMANN  
Lt Colonel, USAF  
Chief, Laser Science & Technology Div

DO NOT RETURN COPIES OF THIS REPORT UNLESS CONTRACTUAL OBLIGATIONS OR NOTICE ON A SPECIFIC DOCUMENT REQUIRES THAT IT BE RETURNED.

UNCLASSIFIED

SECURITY CLASSIFICATION OF THIS PAGE

REPORT DOCUMENTATION PAGE				Form Approved OMB No 0704-0188	
1a. REPORT SECURITY CLASSIFICATION Unclassified			1b. RESTRICTIVE MARKINGS		
2a. SECURITY CLASSIFICATION AUTHORITY			3. DISTRIBUTION/AVAILABILITY OF REPORT Approved for public release; distribution unlimited.		
2b. DECLASSIFICATION/DOWNGRADING SCHEDULE			5. MONITORING ORGANIZATION REPORT NUMBER(S) WL-TR-89-26		
4. PERFORMING ORGANIZATION REPORT NUMBER(S)			7a. NAME OF MONITORING ORGANIZATION Weapons Laboratory		
6a. NAME OF PERFORMING ORGANIZATION Battelle		6b. OFFICE SYMBOL (if applicable)	7b. ADDRESS (City, State, and ZIP Code) Kirtland Air Force Base, NM 87117-6008		
6c. ADDRESS (City, State, and ZIP Code) Pacific Northwest Laboratory Richland, WA 99352			9. PROCUREMENT INSTRUMENT IDENTIFICATION NUMBER DE-AC06-76RL0 1830		
8a. NAME OF FUNDING/SPONSORING ORGANIZATION		8b. OFFICE SYMBOL (if applicable)	10. SOURCE OF FUNDING NUMBERS		
8c. ADDRESS (City, State, and ZIP Code)			PROGRAM ELEMENT NO 61101F	PROJECT NO. ILIR	TASK NO 87
			WORK UNIT ACCESSION NO 05		
11. TITLE (Include Security Classification) DEVELOP TECHNIQUES FOR ION IMPLANTATION OF PLZT FOR ADAPTIVE OPTICS					
12. PERSONAL AUTHOR(S) Craig, R.A.; Batishko, C.R.; Brimhall, J.L.; Pawlewicz, W.T.; Stahl, K.A.; Toburen, L.H.					
13a. TYPE OF REPORT Final		13b. TIME COVERED FROM Oct 85 to Mar 89		14. DATE OF REPORT (Year, Month, Day) 1989, November	
				15. PAGE COUNT 152	
16. SUPPLEMENTARY NOTATION					
17. COSATI CODES			18. SUBJECT TERMS (Continue on reverse if necessary and identify by block number)		
FIELD	GROUP	SUB-GROUP	Ion-implanted PLZT, Photosensitivity, Ferroelectric Ceramic, Adaptive Optics		
20	06				
19. ABSTRACT (Continue on reverse if necessary and identify by block number) Battelle Pacific Northwest Laboratory (PNL) conducted research into the preparation and characterization of ion-implanted adaptive optic elements based on lead-lanthanum-zirconate titanate (PLZT). Over the 4-yr effort beginning FY 1985, the ability to increase the photosensitivity of PLZT and extend it to longer wavelengths was developed. The emphasis during the last two years was to develop a model to provide a basis for choosing implantation species and parameters. Experiments which probe the electronic structure were performed on virgin and implanted PLZT samples. Also performed were experiments designed to connect the developing conceptual model with the experimental results. The emphasis in FY 1988 was to extend the photosensitivity out to diode laser wavelengths. The experiments and modelling effort indicate that manganese will form appropriate intermediate energy states to achieve the longer wavelength photosensitivity. Preliminary experiments were also conducted to deposit thin film PLZT. !					
20. DISTRIBUTION/AVAILABILITY OF ABSTRACT <input type="checkbox"/> UNCLASSIFIED/UNLIMITED <input type="checkbox"/> SAME AS RPT <input checked="" type="checkbox"/> DTIC USERS			21. ABSTRACT SECURITY CLASSIFICATION Unclassified		
22a. NAME OF RESPONSIBLE INDIVIDUAL Sylvia D. Mancha			22b. TELEPHONE (Include Area Code) (505) 844-0166		22c. OFFICE SYMBOL AROF

DD Form 1473, JUN 86

Previous editions are obsolete.

SECURITY CLASSIFICATION OF THIS PAGE

UNCLASSIFIED

# SUMMARY

In fiscal years 1985 and 1986, the Pacific Northwest Laboratory (PNL) conducted research into the preparation and characterization of ion implanted adaptive optic elements based on lead-lanthanum-zirconate-titanate (PLZT) technology. The objectives for FY 1985 were to acquire and/or adapt the necessary hardware and acquire the experience needed to implant PLZT following procedures provided by the Air Force and Dr. Cecil Land of Sandia National Laboratory.

The objectives for FY 1986 were to continue to develop the capability to ion implant and coat PLZT, to initiate implantations which would enhance the photosensitivity and extend it to longer wavelengths, to investigate stress behavior which leads to sample cracking, to prepare samples for delivery to the Air Force for use in its research, and to characterize the wafers for application as adaptive optical elements.

By the end of FY 1986,

- a total of 25 samples had been prepared and delivered to the Air Force for study
- a total of nine different species or combinations of species had been implanted
- stress cracking had been investigated and had been found not to be caused by the Indium Tin Oxide (ITO) electrode coating as originally hypothesized
- an alternative hypothesis for the stress cracking--crowding by the implanted ions and damage-induced voids--had been suggested
- a means of deducing implantation layer refractive index, thickness, and density from transmission measurements had been developed
- a preliminary experiment to deposit thin PLZT had been conducted.

During FY 1987, the primary thrust was a modeling effort aimed at providing a basis for choosing implantation species and parameters. A literature search showed that no fundamental models had been published for PLZT, but that some materials having similar structure could possibly provide a starting point from which a PLZT model could be derived. Many of the modeling task results

described in this report were extrapolated from other materials. Some experimental implantations provided data consistent with the findings reported.

An additional task for FY 1987 was to improve the implantation uniformity over the area of the 0.5-in square samples. Adjustments were made which resulted in a significant improvement.

During FY 1988, the primary thrust was to continue to develop the picture of what is happening in PLZT at the electronic level. Experiments which probe the electronic structure were performed on virgin and implanted PLZT samples. As part of this effort, experiments designed to connect the developing conceptual model with the very limited experimental results were performed. Fiscal year 1988 results established the value of spectral pyroelectric and photoconductivity-type measurements in understanding the optical response of these materials.

Accession For		
NTIS	GPA&I	<input checked="" type="checkbox"/>
DTIC	TAB	<input type="checkbox"/>
	Unannounced	<input type="checkbox"/>
Justification		
By		
Distribution/		
Availability Codes		
Serial and/or		
Dist	Serial	
A-1		

## CONTENTS

<u>Section</u>	<u>Page</u>
1.0 BACKGROUND AND INTRODUCTION	1
2.0 IMPLANTATION	5
2.1 EXPERIMENTAL TECHNIQUE	5
2.2 CALCULATION OF IMPLANTATION DAMAGE	6
2.3 ION IMPLANTATIONS	7
2.4 ACCELERATOR OPERATIONS	11
3.0 COATINGS	14
3.1 ITO COATINGS: PREPARATION AND CHARACTERIZATION	14
4.0 PLZT FABRICATION	15
4.1 THIN-FILM FABRICATION	15
4.2 BULK-PLZT PREPARATION	16
4.2.1 Experimental Procedures and Results	17
4.2.2 Discussion	19
5.0 CHARACTERIZATION	20
5.1 CAPABILITY DEVELOPMENT	20
5.2 MICROSTRUCTURE OF PLZT	21
5.3 MECHANICAL STRESS AND CURVATURE	23
5.4 PLZT CURVATURE VERSUS APPLIED VOLTAGE	24
5.5 TRANSMISSION MEASUREMENTS	27
5.6 IMPLANTED PLZT REFRACTIVE INDEX, DENSITY, AND THICKNESS	28
5.7 PHOTSENSITIVITY MEASUREMENT	30
5.8 OPTICAL PROPERTIES	33
6.0 MODEL DEVELOPMENT	39
6.1 LITERATURE SEARCH	39
6.2 THE CHEMICAL MODEL	40
6.3 THE ELECTRONIC MODEL	42
6.4 RELATIONSHIP TO EXPERIMENT	44
6.5 TECHNOLOGICAL IMPLICATIONS	45
7.0 CONCLUSIONS AND RECOMMENDATIONS	48
REFERENCES	135
ACRONYMS	137

## FIGURES

<u>Figure</u>		<u>Page</u>
1	Sample holder configuration.	50
2	Damage curves for implantation of $\text{Ne}^+$ and $\text{Ni}^+$ ions for sample 9/13 A-C.	51
3	Damage curves for implantation of $\text{Ne}^+$ and $\text{O}^+$ ions for samples C-13(4) M5.	51
4	Damage curves for implantation of $\text{Ne}^+$ and $\text{Al}^+$ ions for samples 7/25 A-D, 7/24 A,B.	52
5	Damage curves for implantation of $\text{Ne}^+$ and $\text{Cr}^+$ ions for samples 7/24 C,D, 7/23 A-D.	52
6	Damage curves for variable energy implant $\text{Ni}^+$ ions for samples 9/13 A-C.	53
7	Implantation uniformity sample before and after accelerator modifications.	54
8	Effects of raster scan speed on uniformity.	55
9	Thin film PLZT transmission.	56
10	Thin film PLZT X-ray diffraction.	57
11	X-ray diffractometer scan of PZT annealed at $1150^\circ\text{C}$ for 1 h.	58
12	X-ray diffractometer scan of PZT + Mn + La annealed at $1000^\circ\text{C}$ for 1 h.	59
13	Surface deformation examined using interferometer.	60
14	Steps in preparation of cross-section specimens for TEM.	61
15	TEM micrograph of PLZT showing featureless, defect-free grain structure.	62
16	Selected area electron diffraction pattern from structure shown in Fig. 15.	62
17	TEM micrograph of PLZT.	63
18	TEM micrograph of PLZT showing very fine micro-crystalline region.	63
19	Selected area electron diffraction pattern from the structure shown in Fig. 18.	64

## FIGURES (Continued)

<u>Figure</u>		<u>Page</u>
20	EDX elemental spectrum from perovskite region of the sample shown in Fig. 15.	65
21	EDX elemental spectrum from microcrystalline, (Zr,Ti)O <sub>2</sub> phase as shown in Fig. 18.	66
22	PLZT wafer after implant.	67
23	Interferogram showing the effect of 200°C, 10-h, air anneal on reducing curvature after implantation.	67
24	Implanted sample curvature hysteresis.	68
25	ITO stress (10 <sup>8</sup> dynes/cm <sup>2</sup> ).	69
26	Transmission of as-received wafer.	70
27	Transmission of annealed wafer.	71
28	Transmission of cut and annealed wafer.	72
29	Transmission of implanted and ITO-coated wafer.	73
30	Transmission of as-received 7/70/30 wafer.	74
31	Oscillations in IR-transmission of implanted PLZT.	75
32	O <sup>2+</sup> implanted sample B-8, first characteristic curve.	76
33	Photosensitivity test of 7/65/35/PLZT implanted with O <sup>+</sup> ions.	77
34	Diffraction of 3 mW HeNe beam by 300-line-per-inch Ronchi ruling printed on sample 9/18B.	78
35	Diffraction of 25 mW HeNe beam by 300-line-per-inch Ronchi ruling printed on sample 9/18B.	78
36	Sample 9/17C, O <sup>+</sup> + Ni <sup>+</sup> ; sensitivity run. No light to 4.5 MW at 476.2 nm.	79
37	Sample 9/17C; O <sup>+</sup> + Ni <sup>+</sup> ; sensitivity run, expanded. No light to 4.5 MW at 476.2 nm.	80
38	Sensitivity run, sample 9/13C; 1.5, 5.5, and 10 MW at 476.2 nm.	81
39	Sensitivity run, sample 9/13C; 1.5, 5.5, and 10 MW at 482.5 nm.	82



## FIGURES (Continued)

<u>Figure</u>		<u>Page</u>
40	Sensitivity run, sample 9/13C; 1.5, 5.5, and 10 MW at 520.8 nm.	83
41	USAF PLZT adaptive optics - sensitivity: 9/13C(a) and 9/22B.	84
42	USAF PLZT adaptive optics - sensitivity: 9/13C(e) and DP2-547.	85
43	Sensitivity run, sample 7/24A (1.3 MeV Al plus 1.3 MeV Ne); 0, 5, 10, and 20 MW at 476.2 nm.	86
44	USAF PLZT adaptive optics - sensitivity: 7/24A.	87
45	Sensitivity run, sample 7/24A (10- $\mu$ F capacitor) after reanneal; 0 and 20 MW at 476.2 nm.	88
46	USAF PLZT adaptive optics - sensitivity after anneal: 7/24A.	89
47	Sensitivity run, sample 7/23D, 7/70/30 (1.3 MeV Cr plus 1.3 MeV Ne); 0, 5, 10, and 20 MW at 476.2 nm.	90
48	Change in CV per change in beam power, sample 7/23D, file DCVIR1, combination of Kr <sup>+</sup> Laser and Xe lamp results.	91
49	Sensitivity run, sample 9/20A; 0 and 50 MW at 476.2 nm.	92
50	Sensitivity run, sample 9/20A; 0 and 50 MW at 676.4 nm.	93
51	Spectral photosensitivity of C <sup>+</sup> -O <sup>+</sup> coimplanted PLZT, sample 9/12C.	94
52	Spectral photosensitivity of C <sup>+</sup> -O <sup>+</sup> coimplanted PLZT, sample 9/11B.	95
53	Implantation profiles.	96
54	Preliminary test of spectral photoconductivity method for C <sup>+</sup> , O <sub>3</sub> <sup>+</sup> implanted PLZT.	97
55	Preliminary test of spectral photoconductivity method for C <sup>+</sup> , O <sup>+</sup> implanted PLZT.	98
56	Photoacoustic spectra of PZT and doped PZT.	99
57	Photoacoustic spectrum of neodymium-oxide.	100
58	Photoacoustic spectrum of crushed 70/65 unimplanted PLZT.	101

## FIGURES (Continued)

<u>Figure</u>		<u>Page</u>
59	Diffuse reflectance spectra of undoped and doped PZT.	102
60	Spectral content of Xenon-arc lamp/monochrometer combination.	103
61	Pyroelectric response for virgin PLZT sample 7/51.	104
62	Photoconductivity response for sample 7/51.	105
63	Pyroelectric response for sample 9/10B, $O^{3+}$ , $C^+$ dual implant.	106
64	Pyroelectric response for sample 9/21B, a triple- $Ni^+$ implant, nonimplanted side.	107
65	Pyroelectric response for sample 7/21B, a triple- $Ni^+$ implant, implanted side.	108
66	Pyroelectric response for sample 9/18B, an $Ne^+$ , $Ni^+$ dual-implant, nonimplanted side illuminated.	109
67	Pyroelectric response for sample 9/18B, an $Ne^+$ , $Ni^+$ dual-implant, implanted side illuminated.	110
68	Pyroelectric response for sample 9/10A, an $O^+$ , $C^+$ dual-implant, nonimplanted side illuminated.	111
69	Pyroelectric response for sample 9/10A, an $O^+$ , $C^+$ dual-implant, implanted side illuminated.	112
70	Photoconductivity-mode spectrum of sample 9/10B, an $O^{3+}$ , $C^+$ dual-implant, nonimplanted side illuminated.	113
71	Photoconductivity-mode spectrum of sample 9/10B, an $O^{3+}$ , $C^+$ dual-implant, implanted side illuminated.	114
72	Photoconductivity-mode spectrum of sample 9/21B, a triple- $Ni^+$ implant, nonimplanted side illuminated.	115
73	Photoconductivity-mode spectrum of sample 9/21B, a triple- $Ni^+$ implant, implanted side illuminated.	116
74	Photoconductivity-mode spectrum of sample 9/18B, an $Ne^+$ , $Ni^+$ dual-implant, nonimplanted side illuminated.	117
75	Photoconductivity-mode spectrum of sample 9/18B, an $Ne^+$ , $Ni^+$ dual-implant, implanted side illuminated.	118
76	Photoconductivity-mode spectrum of sample 9/10A, an $O^+$ , $C^+$ dual-implant, nonimplanted side illuminated.	119

## FIGURES (Concluded)

<u>Figure</u>		<u>Page</u>
77	Photoconductivity-mode spectrum of sample 9/10A, an $O^+$ , $C^+$ dual-implant, implanted side illuminated.	120
78	Photoconductivity-mode spectrum of virgin PLZT sample 7/51, lock-in amplifier set for autophase.	121
79	Photoconductivity-mode spectrum of virgin PLZT sample 7/51, lock-in amplifier not set for autophase.	122
80	Photoconductivity-mode spectrum of virgin PLZT sample 7/51 as a function of bias voltage.	123
81	Electrical setup for pyroelectric and photoconductivity-mode measurements.	124
82	DC-photoconductivity signal for sample 9/10B at 488 nm.	125
83	Source of pyroelectric response.	126
84	Result of doping PZT with La and Mn (Ref. 7).	127
85	APW results along the line for several perovskite-type compounds and $ReO_2$ .	128
86	LCAO band structure and density of states for $SrTiO_3$ .	128
87	Adjusted LCAO band structures for $SrTiO_3$ and $KTaO_3$ (adjusted to include optical and cyclotron resonance results).	129
88	Density of states and joint density of states curves for the adjusted LCAO band-structure models for $SrTiO_3$ and $KTaO_3$ and a comparison with the experimental $\epsilon_2$ (dashed curves).	130
89	Conceptual model for density of electronic states of PZT.	131
90	Results for doping PZT with La (Mn removed) (Ref. 7).	132
91	Spectral transmittance of unimplanted PLZT.	133
92	PZT structure.	134

## TABLES

<u>Table</u>		<u>Page</u>
1	Ion. implantation in FY 1986.	8
2	Implantation uniformity test.	10
3	Dual implantations.	11
4	Sample irradiations.	12
5	XES compositional analysis of 9065 PLZT target films (atomic percent).	17
6	PLZT curvature (mechanical stress) versus processing step case: $1.0 \times 10^{15}/\text{cm}^2$ 500 KeV $\text{Ne}^+$ plus $1-1.7 \times 10^{15}/\text{cm}^2$ 1.4 MeV $\text{Ni}^+$ .	25
7	Reduction of implant-induced wafer curvature by 200°C, 10-h, air anneal. (Curvatures in micrometers per quarter inch.)	25
8	PLZT implanted-layer characterization	29

## 1.0 BACKGROUND AND INTRODUCTION

The Weapons Laboratory (WL) at Kirtland Air Force Base initiated the research which is the subject of this report at the Pacific Northwest Laboratory (PNL) in the second quarter of FY 1985. The purpose of this work was to provide support for the development of the lanthanum-doped lead-zirconate/titanate (PLZT) adaptive-optical components needed for phase correction. The primary objective of the project at that time was providing the Air Force with implanted PLZT samples for use in experimental adaptive-optics work. Fiscal year 1985 was characterized by a learning process during which the hardware was adapted and characterization capabilities developed. Samples implanted were intended to establish and demonstrate capability by duplicating work done previously at Sandia National Laboratory (SNL) (Refs. 1 to 3). Fiscal year 1985 closed with the implantation capability having been successfully demonstrated, but with few delivered.

The FY 1986 objectives were considerably more ambitious and were driven by a need to deliver usable samples. A coatings task was added to the project team. The leader of this task was charged with developing an optimum Indium Tin Oxide (ITO) coating, investigating stress cracking hypothesized as being caused by the mechanical mismatch between the ITO coating and the PLZT substrate, and attempting to fabricate thin-film PLZT.

Additionally, characterization task objectives emphasized replicating the characterization capabilities at SNL so that comparisons could be made, and also defining some areas in which additional characterization would be attempted.

The plan for FY 1987 was to expand the implantation hardware to accommodate larger samples and greater numbers of samples, to continue the thin-film PLZT research, to continue producing material for the Air Force's research, and to develop a conceptual model of PLZT based on first principles.

Because of a change in Air Force priorities, funding in FY 1987 was significantly smaller than that needed for continuing the project with the planned scope, or even with the same scope as in FY 1986. A reduced proposal was prepared which shifted the project emphasis from producing samples for the Air Force to basic research. The principal activity was an attempt to develop

a first-principles conceptual model of the behavior of PLZT to replace the heuristic guidelines being used. This was intended to provide a basis for implantations that would extend the photosensitivity to longer wavelengths.

The implantation task was to include some work aimed at improving implantation uniformity, but all other tasks were limited to supporting the modeling activity.

During FY 1987 some progress was made in understanding the relationship between the stoichiometry and electronic structure of the PLZT material. A tentative conceptual model for what was happening was proposed, and implantations based on that model showed improved sensitivity. It was also determined that there was little experimental information about the actual optical properties of this material either in the virgin or implanted state. Some preliminary optical experiments were performed which indicated that relevant information might be accessible optically.

For FY 1988 it was determined that the first priority would be optical characterization of the PLZT electronic spectrum which would support the development of an improved conceptual model of the electronic structure and the supporting calculations.

This report summarizes the results of the research conducted during the course of the work. It describes the processing of PLZT samples for a range of implantation species and parameters and presents representative data characterizing those samples. Finally, it presents the conclusions reached by analyzing and interpreting the data.

The report is organized according to the technical areas that the work explored: Implantation, Coatings, Thin-Film Fabrication, Characterization, and the Conceptual Model.

The overall objective of this program has been to develop techniques for the fabrication of adaptive optical components with high photosensitivity using ion implantation of PLZT. Supporting objectives have been to develop an understanding of the factors that govern the photosensitivity of these materials, to fabricate sputtered transparent electrodes, and to evaluate the

samples for spectral photosensitivity, contrast, and resolving power, with principal emphasis on understanding the photosensitivity.

Optical beams propagating through an inhomogeneous medium are aberrated by point-to-point phase differences across the wavefront, resulting in decreased efficiency in transmitting a focused beam through the medium. By introducing equal and opposite phase differences into the transmitted beam before propagation, medium-induced phase differences will cancel those introduced by transmission resulting in formation of a diffraction-limited focal spot. Near real-time correction of the medium-induced phase differences may be achieved with optical-phase conjugation using adaptive optical components fabricated from ion-implanted PLZT. A sampling beam passing through the medium interferes with a reference beam at the PLZT wafer to form a hologram which stores medium-induced phase shifts. The beam to be transmitted is used to reconstruct the hologram, introducing the compensating phase shifts, and resulting in a diffraction-limited focal spot at the sample beam position. This phenomenon, using ion-implanted PLZT, has been demonstrated by investigators at the WL (Ref. 4).

Storage of phase information in PLZT, as used for hologram storage, was initially investigated by workers at Motorola\* and SNL (Refs. 2 and 3), who were involved in some of the early work leading to the concepts described here. These investigators developed a successful model for the field-assisted photorefractive effect in this material. Their model (Ref. 1) for the optical structure of the material and how this might be affected by implantation was empirical and heuristic.

As-fabricated PLZT is capable of storing optical data, but is relatively insensitive to the visible through infrared parts of the electromagnetic spectrum. Ion-implantation of the material results in changes in the damage zone. These changes result in more efficient device switching and an improved sensitivity to electromagnetic energy at visible and longer wavelengths.

---

\*Albuquerque, New Mexico.

This research initially focused on ion implantation of PLZT to enhance the photosensitivity at wavelengths of interest. In the process, related areas of implantation-induced stress cracking, optically transparent electrode design, and optical characterization of resulting samples have been addressed. During the course of the work, the research effort was redirected to focus on developing a fundamental understanding of the electronic behavior of the PLZT material so that a rational selection of implantation species and parameters could be implemented.



## 2.0 IMPLANTATION

Approximately 50 specimens of PLZT were ion-implanted during FY 1986. Ions of neon, aluminum, chromium, nickel, nitrogen, and oxygen in various combinations were used. Both the type of ion and ion energy were varied in the multiple-ion implants. In this report, the technique used in the implantations is described, the expected damage distribution from the implantations is calculated, and a listing of all implants and the parameters is presented.

During FY 1987, the accelerator tube and irradiation chamber were modified to improve implantation uniformity. Apertures and other possible protuberances were enlarged or removed so as not to intersect the beam during raster scanning. Samples were implanted to test the improvements resulting from the modifications.

No implantations were performed during FY 1988. Experimental analyses of implanted samples were performed on samples prepared in previous years. Preparation of bulk PLZT samples for the photoacoustic experiments is reported in Section 4.0, PLZT Fabrication.

### 2.1 EXPERIMENTAL TECHNIQUE

Prior to implantation, a 1-in square sheet of PLZT would be cut into four smaller sheets 0.5 in on a side. One side was coated with a thin ( $\approx 10$  nm) layer of ITO to dissipate charge buildup during implantation. Six specimens were mounted on the copper block shown in Fig. 1 and held in place by clamping at opposite corners. The copper block was mounted on a rotatable shaft which had vertical and horizontal motion.

During implantation, the beam was aligned through the hole in the copper block. This hole was exactly centered on the 1 x 1 in face of the copper block. Once the maximum current was aligned through the hole, the holder was rotated 45 deg or a multiple thereof to bring the specimen into the beam. An estimate of beam size was made by comparing the current through the 0.25-in diam hole to the current in a 0.5-in diam Faraday cage.

Beam lines from two separate accelerators were brought into the specimen chamber so that a variety of implants could be done without moving the specimen from the vacuum chamber. Inert-gas ions were accelerated up to  $\approx 1.8 n$  MeV with a van der Graaff accelerator, where  $n$  is the charge on the ion. A 2-MeV tandem accelerator was used for all other ions. Depending on the charge state of the ions, energies up to 8 MeV can be obtained on the tandem. The vacuum in the specimen chamber was typically  $< 1 \times 10^{-7}$  torr when using the tandem, but only in the  $10^{-8}$  torr range when using the van der Graaff.

During implantation, the beam was moved in a serpentine pattern across the surface to provide uniform implantation. The beam current was also monitored on the specimen during irradiation. The sample holder was not suppressed for electron scatter, so the current read higher than actual beam current. The beam current is checked periodically with the Faraday cage located behind the holder, and this is used to get the integrated dose of the specimen. The beam can also be observed visually in the darkened chamber because of the fluorescence from the specimen. Beam current densities ranged from 0.02 to 0.5  $\mu\text{A}/\text{cm}^2$ . The surface temperature was monitored periodically by an infrared pyrometer when using large beam currents. The temperature was always  $< 160^\circ\text{C}$ , the smallest temperature measured by the pyrometer.

## 2.2 CALCULATION OF IMPLANTATION DAMAGE

The damage distribution produced by the ions was calculated using the EDEP program (Ref. 5). This program determines the energy deposited into the material during the ion-atom interaction. Both electronic and nuclear energy losses are calculated. It is only the nuclear energy loss that produces displaced atoms. The fraction of displaced atoms (dpa) can be computed from the following expression:

$$\text{dpa} = [\beta \text{SD}(x) \Phi t / (2T_D N_D)] \quad (1)$$

where

$SD(x)$  = nuclear energy loss in MeV/mm

$T_D$  = energy required to permanently displace atom from its site  $\approx 40$  eV

$\beta$  = numerical factor  $\approx 2$

$\Phi_t$  = ion fluence in ions/cm<sup>2</sup>

$N_D$  = atomic density in atoms/cm<sup>3</sup>

The dpa value gives a measure of the magnitude of the damage produced in the lattice in terms of atom defects. The range and range straggling of the ions are also computed in the EDEP program.

The concentration of deposited ions can be calculated from the expression:

$$C_i = (\Phi_t / 2\pi\sigma) \exp[-(x - x_o)^2 / 2\sigma^2] \quad (2)$$

where

$C_i$  = atom concentration of deposited ions at point  $x$

$\Phi_t$  = ion fluence

$\sigma$  = standard deviation of the distribution of deposited ion

$x_o$  = projected range of ions

This assumes a Gaussian distribution with a maximum at the projected range. For ion fluences of  $1 \times 10^{15}$  and energies near 1 MeV, the maximum concentrations are  $<0.1$  percent. The standard deviation,  $\sigma$ , is a direct function of the ion penetration so high-energy ions will have a large  $\sigma$  and hence a broader distribution.

### 2.3 ION IMPLANTATIONS

A list of the implantations completed during FY 1986 is shown in Table 1. Representative damage curves calculated from the EDEP program using actual implantation conditions are shown in Figs. 2 through 5. All the curves show a maximum near the end of the damage region. The range of the ions,  $x$ , is always just beyond the maximum in the damage curve. As shown by the curves, lighter ions will give a greater depth of damage but less damage per unit fluence than heavier ions for comparable ion energies. For multiple implants,

TABLE 1. Ion implantation in FY 1986.

Specimen	Implant	Dose (ions/cm <sup>2</sup> )	No. of Specimens
(1)	1.4 MeV O <sup>+</sup>	3 x 10 <sup>15</sup>	1
#4 A <sub>1</sub> B	500 KeV Ne <sup>+</sup> (impure beam)	1 x 10 <sup>15</sup>	2
#5 (A-D)	Diffused Al <sup>+</sup> (vac) 500 KeV Ne <sup>+</sup>	1 x 10 <sup>15</sup>	4
C-13(1,2,3)	500 KeV Ne <sup>+</sup> 1.4 MeV Ni <sup>+</sup>	1 x 10 <sup>15</sup> 1 x 10 <sup>15</sup>	3
C-13(4, M5)	500 KeV Ne <sup>+</sup> 1.4 MeV O <sup>+</sup>	1 x 10 <sup>15</sup> 2 x 10 <sup>15</sup>	2
B7(1,2,3)	1.4 MeV O <sup>+</sup> 1.4 MeV Ni <sup>+</sup>	2 x 10 <sup>15</sup> 1 x 10 <sup>15</sup>	3
9/22(A-D)	Diffused Al <sup>+</sup> in Air +500 KeV Ne <sup>+</sup>	1 x 10 <sup>15</sup>	4
9/13(A-C)	500 KeV Ne <sup>+</sup> 900 KeV Ne <sup>+</sup> 1.4 MeV Ni <sup>+</sup>	1 x 10 <sup>15</sup> 1.5 x 10 <sup>15</sup> 5 x 10 <sup>14</sup>	3
9-13D 9-14A,B	500 KeV Ne <sup>+</sup> 900 KeV Ne <sup>+</sup> 1.4 MeV Ni <sup>+</sup>	1 x 10 <sup>15</sup> 1.5 x 10 <sup>15</sup> 7 x 10 <sup>14</sup>	3
7/25(A-D) 7/24(A,B)	1.3 MeV Ne <sup>+</sup> 1.3 MeV Al <sup>+</sup>	2.5 x 10 <sup>15</sup> 1 x 10 <sup>15</sup>	6
7/24(C,D) 7/23(A-D)	1.3 MeV Ne <sup>+</sup> 1.4 MeV Cr	2 x 10 <sup>15</sup> 8 x 10 <sup>14</sup>	5
9/20(A,B,D)	5 MeV Ni <sup>++</sup> 2.4 MeV Ni <sup>+</sup> 1.3 MeV Ni <sup>+</sup>	1 x 10 <sup>15</sup> 4 x 10 <sup>14</sup> 2.5 x 10 <sup>14</sup>	3
9/21(A-C)	4.5 MeV Ni <sup>++</sup> 2 MeV Ni <sup>+</sup> 1.3 MeV Ni <sup>+</sup>	5 x 10 <sup>14</sup> 2 x 10 <sup>14</sup> 1.25 x 10 <sup>14</sup>	3

the individual curves can be summed to produce a total damage curve. The total damage curves can appear to be very inhomogeneous, but by proper choice of energy and fluence, a relatively uniform damage region can be generated as demonstrated by the triple implant of nickel in Fig. 6.

After implantations, the surface of the PLZT shows a slightly foggy appearance. In earlier irradiations, some nonuniformity across the width of the sample was visible. With increasing experience, uniformity of implantation improved. Unimplanted regions will always be present at the corners where the samples are clamped to the sample holder.

The inherent nonuniformity in damage as a function of depth as shown by the damage curves has not as yet been measured. One measure of the total depth of damage is obtained from the changes in the index of refraction. Although a uniform damage region is assumed in the measurement, the measured damage depth agrees quite well with the calculated value. It is possible that changes in the index of refraction reach a maximum at a small, critical fluence. All the doses used so far in the experiments may be greater than this critical fluence, so that variations in damage distribution are not detected.

During FY 1987, modifications were performed on the accelerator tube and irradiation chamber to improve implantation uniformity. All apertures were enlarged to a minimum of 1 in in diameter.

A number of Ni-ion implantations were carried out using various raster scanning parameters to test uniformity after the modifications. The PLZT was implanted with  $\approx 2$  MeV  $\text{Ni}^+$  ion at doses ranging from 3 to  $7 \times 10^{14}$  ions/cm<sup>2</sup>. The times to complete one cycle varied from 2 s to  $\approx 2$  min (Table 2). A total of eight specimens were implanted under various conditions of dose and scanning. The implanted wafers were then placed in a biasing circuit and photographed as they underwent domain switching. This is an effective qualitative method since implanted and unimplanted areas on an unevenly implanted wafer switch at slightly different bias voltages and so a transmission photograph of the wafer during this switching reveals the regions of differing implant dose. Typical results showing poor uniformity before beam-line modifications and good uniformity after modifications are shown in Figs. 7(a) and (b). The irradiation uniformity was much improved after the

TABLE 2. Implantation uniformity test.

Specimen	Ion	Dose (Ions/cm <sup>2</sup> )	Raster Scan Cycle
9/15A	2.0 MeV Ni+	$2.8 \times 10^{14}$	8.5 s
9/16C	2.0 MeV Ni+	$3.0 \times 10^{14}$	2.2 s
9/16D	2.0 MeV Ni+	$3.0 \times 10^{14}$	8.5 s
9/12A	2.4 MeV Ni+	$5.8 \times 10^{14}$	2.2 s
9/12B	2.4 MeV Ni+	$9.4 \times 10^{14}$	8.5 s
9/14C	2.4 MeV Ni+	$7.5 \times 10^{14}$	25 s
9/12D	2.4 MeV Ni+	$7.5 \times 10^{14}$	104 s
9/15B	2.0 MeV Ni+	$1.0 \times 10^{14}$	22 s
		plus $1 \times 10^{15}$	No raster

modifications, although the slowest scan continued to show evidence of non-uniformity. On one specimen where the beam was not moved, a dense spot due to the steady beam was plainly evident on the specimen. These nonuniformities are shown in Figs. 8(a) and (b).

Some PLZT specimens were dual-implanted with  $C^+$  and  $O^+$  ions. Dual implantations of 2.0 MeV  $O^+$  and 1.8 MeV  $C^+$  were planned so that the  $O^+$  and  $C^+$  ions would come to rest in the same region. After the irradiation was complete, it was discovered that the accelerator readings were in error and that  $O^{3+}$  was implanted. This corresponds to an ion energy of  $\approx 4.5$  MeV. The result is that the  $O^+$  was implanted deeper than the  $C^+$  and the dose was only one-third of the planned dose. The O lies at  $2.7 \mu m$  and the C at  $1.5 \mu m$  from the surface. Considerable cracking was evident in these specimens which could have been caused by excessive heating from the high-energy  $O^+$  beam.

The implantations were repeated using the correct  $O^+$  energy. Unfortunately, there were only three PLZT specimens remaining, some of which already had some initial cracks. Table 3 summarizes the parameters of the dual implantations.

TABLE 3. Dual implantations.

Specimen	O <sup>+++</sup>	Dose (ions/cm <sup>2</sup> )	C <sup>+</sup>	Dose (ions/cm <sup>2</sup> )
9/12C	4.5 MeV	3.1 x 10 <sup>14</sup>	1.8 MeV	9.3 x 10 <sup>14</sup>
9/20C	4.5 MeV	3.0 x 10 <sup>14</sup>	1.8 MeV	9.3 x 10 <sup>14</sup>
9/10B	4.5 MeV	3.1 x 10 <sup>14</sup>	1.8 MeV	9.1 x 10 <sup>14</sup>
9/11C	4.5 MeV	3.1 x 10 <sup>14</sup>	1.8 MeV	9.3 x 10 <sup>14</sup>
9/10C	4.5 MeV	3.1 x 10 <sup>14</sup>	1.8 MeV	9.4 x 10 <sup>14</sup>
9/10D	4.5 MeV	3.1 x 10 <sup>14</sup>	1.8 MeV	9.4 x 10 <sup>14</sup>
9/11D	2.0 MeV <sup>a</sup>	1-1.3 x 10 <sup>15</sup>	1.8 MeV	9.5 x 10 <sup>14</sup>
9/11B	2.0 MeV <sup>a</sup>	1.0 x 10 <sup>15</sup>	1.8 MeV	1.0 x 10 <sup>15</sup>
9/14D	2.0 MeV <sup>a</sup>	9.3 x 10 <sup>14</sup>	1.8 MeV	1.0 x 10 <sup>15</sup>

<sup>a</sup>O<sup>+</sup> ions.

Several other PLZT specimens were implanted with O<sup>+</sup>. These were used for investigations of the microstructure and microstructural damage induced by the implantation. Preparation for examination in the electron microscope is destructive, so these specimens were not available for optical analysis.

#### 2.4 ACCELERATOR OPERATIONS

During the course of this work, accelerator operations were organized separately from the implantation task, primarily for organizational convenience and accounting purposes. Most of the other work within this task was inseparable from the implantation task. One accelerator operation was to prepare, install, and test a velocity selector which was to be used for separating ion species in a contaminated beam. Installation took place early in FY 1986. The contamination present at that time was found to be from the bottled gas and so a new bottle was installed. The velocity selector was not tested or used until late in the year when the nitrogen implant appeared to require better separation of species in the beam. At that time, it was still not certain that the selector would or could resolve the problem.

The other part of the accelerator operations work was in support of implantation. Table 4 contains a list of the irradiations performed in FY 1986 in support of the program. Of particular interest are the relative times for various species. The amount of implantation time required per unit area

TABLE 4. Sample irradiations.

Date	Beam/Energy	Accelerator	Time (h)
25 Nov 1985	1.4 MeV O <sup>+1</sup>	Tandem	3
3 Jan 1986	1.0 MeV Ne	VDG	1
7 Jan 1986	0.5 MeV Ne	VDG	2
23 Jan 1986	0.5 MeV Ne	VDG	4
10 Feb 1986	0.5 MeV Ne	VDG	4
13 Feb 1986	1.4 MeV Ni <sup>+1</sup>	Tandem	8
25 Feb 1986	1.4 MeV O <sup>+1</sup>	Tandem	7
28 Feb 1986	1.4 MeV Ni <sup>+1</sup>	Tandem	6
16 Apr 1986	0.5 MeV Ne	VDG	4
17 Apr 1986	0.5 MeV Ne	VDG	4
5 May 1986	0.9 MeV Ne	VDG	4
16 May 1986	1.4 MeV Ni <sup>+1</sup>	Tandem	6
19 May 1986	1.4 MeV Ni <sup>+1</sup>	Tandem	7
4 Jun 1986	1.3 MeV Ne	VDG	4
11 Jun 1986	1.3 MeV Al	Tandem	8
12 Jun 1986	1.3 MeV Al	Tandem	4
16 Jun 1986	1.3 MeV Al	Tandem	8
17 Jun 1986	1.3 MeV Al	Tandem	8
1 Jul 1986	1.3 MeV Ne	VDG	4
7 Jul 1986	1.4 MeV Cr(Tr)	Tandem	4
8 Jul 1986	1.4 MeV Cr	Tandem	8
14 Jul 1986	1.4 MeV Cr	Tandem	4
22 Jul 1986	5.0 MeV Ni <sup>+2</sup>	Tandem	8
23 Jul 1986	5,4,1.3 MeV Ni <sup>+1,+2</sup>	Tandem	7
24 Jul 1986	1.3 MeV Ni <sup>+1</sup>	Tandem	4



of a sample depends on the beam current which can be generated for that species. Of those species implanted that year, Al gave the lowest beam current and required the longest beam times.

### 3.0 COATINGS

#### 3.1 ITO COATINGS: PREPARATION AND CHARACTERIZATION

Indium-Tin Oxide coatings were applied by dc-magnetron reactive sputtering techniques (Ref. 6) in a 28-in box chamber outfitted with a planetary substrate holder. An air-cast metal target (20 weight-percentage-tin) was sputtered in an Ar/O<sub>2</sub> atmosphere. The optically monitored transmission loss with increasing thickness was used to control stoichiometry so that sheet resistance was held at the minimum value. The PLZT wafer temperature was  $\approx 40^{\circ}\text{C}$  during coating application.

The ITO coating thickness was always 160 nm (three quarter waves at 425 nm monitoring wavelength). Sheet resistance measured by the 4-point van der Pauw method (Ref. 7) averaged 85  $\Omega/\text{square}$  and was always within the range of 60 to 130  $\Omega/\text{square}$ . Coating both sides, on the average, maintained 91 percent of the implanted PLZT transmission at 425 nm and a greater percentage ( $>100$  percent in some cases, because the ITO coating reduces the optical mismatch) at longer wavelengths (Fig. 9).

Some PLZT wafers received a thin ITO coating before implantation to dissipate static charge. These coatings were  $\approx 20$  nm thick with sheet resistances of  $\approx 1000$   $\Omega/\text{square}$ . The thin coatings were optically monitored for a transmission drop from 92 to 80 percent at 425 nm on fused-silica witness substrates. This thickness just exceeded that required for electrical continuity.

Air annealing of ITO-coated PLZT improves ITO sheet resistance by  $\approx 20$  percent at  $150^{\circ}\text{C}$ ,  $\approx 40$  percent at  $200^{\circ}\text{C}$ , and  $\approx 50$  percent at  $300^{\circ}\text{C}$ . Transmission either stays the same or increases  $\approx 1$  percent. Thus, it appears that thermal erasing of a voltage-cycled wafer will not harm the ITO and may actually improve it.

#### 4.0 PLZT FABRICATION

Six preliminary PLZT experiments were conducted to assess the level of difficulty and to determine the principal issues governing successful fabrication of thin-film PLZT with adaptive-optics-device potential. Additionally, bulk PLZT was fabricated in order to perform photoacoustic spectroscopy measurements on samples similar to those reported in Ref. 8.

##### 4.1 THIN-FILM FABRICATION

The thin-film fabrication experiments were performed in an RF-diode sputtering system with a 4-in diam Motorola 9065 hot-pressed wafer target, Ar and  $O^+$  sputtering gases, fused silica and sapphire substrates, and a temperature-variable (20 to 400°C) substrate-heater platform. Experiments were guided by important previous experimental results gleaned from a review of published papers.

Thin films made were characterized spectrophotometrically (thickness, refractive index, and qualitative assessment of stoichiometry) by X-ray diffraction (crystallinity, grain size, preferred orientation, and phase) and X-ray energy spectroscopy (absolute composition and comparison with starting target material).

The PNL preliminary experiments were very productive and resulted in the following conclusions:

- RF-diode sputtering of PLZT is straightforward; no technical difficulties were encountered in fabricating thin films.
- Deposition rates are very good, 85 Å/min or 1  $\mu\text{m}/2$  h for medium target power levels.
- Oxidation appears to be complete based on the visible transmission edge measured spectrophotometrically. Examples for a thin (0.355  $\mu\text{m}$ ) and a thick film (1.76  $\mu\text{m}$ ) are shown in Fig. 9.
- Refractive index is small--1.92 at 1000 nm compared to 2.55 for the starting Motorola 9065 hot-pressed wafer.

- Low substrate-temperature (ca. 200°C) thin films are smooth and glass-like in appearance.
- High substrate-temperature (ca. 500°C) thin films are noticeably scattered.
- Both low and high substrate-temperature thin films appear amorphous under X-ray diffraction, although some sign of emerging crystallization is apparent for the 500°C film (Fig. 10). Very high temperatures (600°C or higher) will be required for crystallinity.
- Target composition is maintained in the thin film for La, Zr, and Ti (Table 5).
- Pb content is reduced and must be compensated for in future sputtering (Table 5).
- Pb loss may be slightly greater at higher temperatures (Table 5).
- Adhesion to silica and sapphire is excellent.
- Mechanical stress is small to medium because no mechanical failures (cracking or peeling) were observed in any thin films, even for thicknesses of 4  $\mu\text{m}$ .

The experiments also provided important guidance for future work. Experimental procedures recommended for similar work include:

- Use PLZT sputtering targets with ferroelectric composition (plus compensation for expected Pb loss).
- Use a very high-temperature substrate holder platform (>600°C).
- Use substrates which promote crystallization, grain growth, and possibly epitaxy--(0001)-oriented sapphire--for example.

#### 4.2 BULK-PLZT PREPARATION

This effort was devoted to preparing bulk lead-zirconate titanate (PZT) material samples with varying types and amounts of impurities. These samples were intended for use in optical experiments to obtain information about the electronic structure in the material.

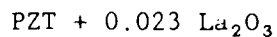
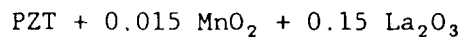
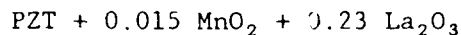
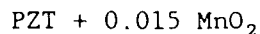
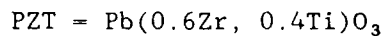
All of the sample material was prepared by a calcining-type process followed by various heat treatments. The structure was analyzed by standard X-ray diffraction methods (Fig. 10). The chief experimental variables that appeared to affect the phase composition and structure were the furnace atmosphere and temperature.

TABLE 5. XES compositional analysis of 9065 PLZT target films (atomic percent).

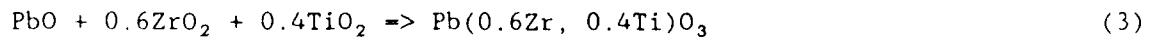
	Pb	La	Zr	Ti
Target (Nominal)	90	10	65	35
Target (Measured)	89.6	10.4	64.1	35.9
Film #1C (200°C)	84.0	16.0	65.3	34.7
Film 1#F (500°C)	82.3	17.7	67.5	32.5

#### 4.2.1 Experimental Procedures and Results

Fine powders of 99.8 percent  $\text{TiO}_2$ , 99 percent  $\text{ZrO}_2$ , 99.99 percent  $\text{PbO}$ , 99 percent  $\text{MnO}_2$  and 99.99 percent  $\text{La}_2\text{O}_3$  were used as starting material. The powders were weighed in the proper stoichiometric ratios and well-mixed in a ball mill. The powders were mixed wet using  $\text{ZrO}_2$  grinding pellets. The PZT materials, identical in composition to those in Ref. 8, were as follows:



After mixing, the powder slurry was dried and calcined at high temperature. Calcining involves heating the powder to an elevated temperature and allowing a solid-state reaction to take place, producing the desired structure and composition. An example is



Initial calcining was done at 950°C for 1 h. Some of the powder material was cold-pressed prior to calcining, but this seemed to have little effect on the nature of the final reaction product. The structure of the calcined powder was analyzed and shown to be mainly the hexagonal/rhombohedral phase within

the perovskite structure of PZT with small but significant amounts of PbO and ZrO<sub>2</sub> present. The calcined powders of pure PZT and those containing La were yellowish in color. Those containing Mn were gray to black.

The calcined powders were pressed into pellets and given various heat treatments to make samples suitable for subsequent optical measurements. A diffractometer scan of PZT annealed at 1150°C for 1 h is shown in Fig. 11. This pattern is typical of most of the analyses. The standard X-ray patterns for the constituents are shown below the experimental pattern. Heat treating at different temperatures and in different atmospheres mainly changed the relative amounts of free PbO and ZrO<sub>2</sub> in the structure. For example, heating in air resulted in a greater PbO content than heating a pellet surrounded by PbO powder. Heating of the material containing Mn and La at temperatures >1000°C did produce the tetragonal phase of PZT. Figure 12 is a diffractometer scan of the material after a 1000°C heat treatment. Heating the same material at 600°C did not produce the tetragonal phase. These particular compositions containing La and Mn did show somewhat more free ZrO<sub>2</sub> after the high-temperature annealing. The compositional changes resulting from loss of Zr from PZT could push it into the tetragonal part of the phase diagram.

When examination of the optical properties showed minimal effects in these materials, a new batch of the PZT with the various additives was made. In this case, the experimental procedures as outlined in Ref. 8 were followed as nearly as could be determined from the written description. A fresh supply of PbO powder was also used. In this case, a large amount of the PbO-ZrO<sub>2</sub>-TiO<sub>2</sub> mixture was prepared. This mixture was then used as a base for adding the small amounts of MnO<sub>2</sub> and La<sub>2</sub>O<sub>3</sub>. Therefore, all of the different compositions were prepared using the same PZT powder base. The powder mixtures were calcined in a closed box at 1000°C for 1 h. The powder was then pressed at 70 MPa and annealed at 600°C for 30 min. In Ref. 8, this 600°C anneal was used to remove organic plasticated residues. This experiment did not use these plasticated residues but performed the annealing in order to match the histories of the samples to those of Ref. 8. The annealing atmosphere was not described in Ref. 8 so air was used. The optical properties of this new batch of material were subsequently tested and the results are reported in Section 5.8 in this report.

#### 4.2.2 Discussion

Although a number of different heat treatments and sample configurations were tried, a single-phase PZT material was not obtained in this work. Some PbO and ZrO<sub>2</sub> were always present to a lesser or greater degree. In the preparation of the PZT for actual application, considerable caution must be used in the sintering process to avoid the loss of PbO and subsequent compositional changes. However, because there were no identifiable phases that could be associated with Mn or La, these elements were presumably in solution in the PZT structure. Incorporating these impurities was the primary objective in preparing these particular compositions. Reference 8 did not report any minor phases although they may have been present in small amounts and were essentially ignored. It is unlikely that the small amounts of PbO and ZrO<sub>2</sub> in the material prepared here would have perturbed the subsequent measurements in the PZT, but this is not certain.

According to the phase diagram reported in Ref. 9, the rhombohedral/hexagonal phase is the stable phase for PZT containing 60 percent Zr. The analysis agrees with this. Reducing the Zr content below  $\approx 55$  percent will cause a transformation to the tetragonal phase. This was qualitatively confirmed in the material with Mn and La that was annealed at high temperature. These materials showed a tetragonal phase and had an increased amount of free ZrO<sub>2</sub>. Because the overall composition met the desired stoichiometry, the presence of isolated ZrO<sub>2</sub> would correlate to a reduced Zr content in the PZT phase. The material in Ref. 8 showed a perovskite structure, and presumably this was in the rhombohedral/hexagonal crystal class. A composition of 8 to 10 percent La is required to bring the structure into the cubic phase.

## 5.0 CHARACTERIZATION

Optical characterization objectives for FY 1986 were defined in a draft annual report submitted to the Air Force under a cover letter dated 24 September 1986. These were:

- investigate methods of characterizing implantation parameters
- improve writing system to give better control of parameters
- provide SNL with implanted samples for comparison
- provide a means for measuring quantum efficiency
- evaluate and try to improve spatial resolution of samples

Subsequent to the redirection of the project, the objectives became focussed on providing information to develop and to calibrate the conceptual model for this material.

### 5.1 CAPABILITY DEVELOPMENT

Early in FY 1986, a number of characterization techniques were investigated. One technique used for determining photosensitivity was the use of an interferometer to evaluate surface deformation caused by a stored hologram. Several samples were exposed and examined using a Mach-Zehnder interferometer. A typical sample interferogram pair is shown in Fig. 13. Surface deformation provides precise measurements of photosensitivity, but it was not explored further because of more pressing priorities and because there were no means for quantitatively evaluating the interferograms. Commercial hardware and software were available to implement the measurement, but the value of such a measurement could not be justified.

Samples continued to be characterized primarily by exposing them to a relatively uniform beam from either a Kr-ion laser or an arc lamp and tracing the hysteresis curve to obtain photosensitivity data.

A computer-controllable, bipolar, high-voltage power supply was obtained and installed. The installation of the power supply provided automatic cycling of the bias voltage for the optical-characterization system and eliminated the need for manual switching during the cycle.



Early in FY 1987, the Air Force modified its software for biasing the samples during write cycles. These changes were incorporated into PNL's system.

A motor-driven sample holder was assembled for use in scanning samples. This could be used to measure uniform implementation and was also available to measure the modulation transfer function (MTF).

A significant improvement in the PNL characterization system occurred following an on-site study of the SNL system. However, the PNL equipment has not been directly calibrated with the SNL equipment.

In late FY 1987 and FY 1988, more and different types of characterization were needed as the project emphasis was redirected toward examination of the microscopic properties of these materials. Therefore, a capability for performing photoacoustic spectroscopy and spectral photoconductivity measurements was developed.

## 5.2 MICROSTRUCTURE OF PLZT

An attempt was made to observe damaged regions in implanted PLZT using transmission electron microscopy (TEM). Although direct observation of the damage was not successful, the study did provide indirect information about radiation damage and stability in PLZT.

It is desirable to observe the damage zones in cross-section; i.e., to view the specimen in a direction perpendicular to the implantation direction. The preparation procedure for cross-section viewing is quite involved. The irradiated PLZT was first cut into narrow slabs  $\approx 2$  mm wide and the implanted sides pressed and bonded together face-to-face as shown in Fig. 14(a). The bonded slabs were sealed in a tube filled with epoxy (Fig. 14b) and thin sections ca. 250  $\mu\text{m}$  thick cut from the tubes to produce the disks shown in Fig. 14(c). This disk was mechanically polished down to ca. 10  $\mu\text{m}$  thickness and finally thinned to perforation by ion milling (Fig. 14d). The specimens were ion-milled with 5 to 6 KeV Ar ions operating at 1 to 2 mA. It was intended that a thin area  $< 100$  nm thick would form in the specimen near the damaged region.

The microstructure of PLZT as observed by TEM is relatively featureless. A grain-boundary triple junction is pointed out in Fig. 15. The light and dark regions are a result of uneven thinning during ion milling. In spite of repeated tries, it was not possible to produce foil that was thin enough in the region where the ions were implanted for TEM analysis.

The electron-diffraction pattern from a region similar to the one in Fig. 15 is shown in Fig. 16. The bright spots are typical of crystalline materials and can be indexed to fit the perovskite phase. The diffuse ring is typical of the diffraction pattern from an amorphous structure. It is surmised that the amorphous structure results from ion milling damage. Argon ions of 5 to 6 KeV would produce damage to a depth of perhaps 50 Å. As the foil was ion-milled from both sides, a 100-Å thick total layer of amorphous material could be produced. Since the total thickness of a foil such as that in Fig. 15 may only be 500 Å, this represents 20 percent of the thickness. This would definitely be revealed in the electron diffraction pattern. The implication of this observation is that ion implantation of higher energy ions could transform crystalline PLZT into an amorphous structure. The dose and energy dependence of the transformation remains an unresolved issue.

The other significant observation in this study was a phase transformation caused by the loss of Pb or PbO from the specimen. Upon repeated thinning cycles in the ion-milling machine, a change in structure was observed. Small dark areas appeared in some grains (Fig. 17) eventually leading to the fine microcrystalline structure shown in Fig. 18. The electron-diffraction pattern from the region of Fig. 18 shows a series of concentric rings, typical of very fine crystallites (Fig. 19). This pattern was indexed as a tetragonal  $(\text{Zr,Ti})\text{O}_2$ . The energy dispersive X-ray analysis (EDX) of the structure shows a loss of Pb. The spectrum for the perovskite phase is shown in Fig. 20. The spectrum for the  $(\text{Zr,Ti})\text{O}_2$  phase is shown in Fig. 21. The Pb concentration is drastically reduced in the microcrystallite region. The Mo and Cu peaks are system peaks not associated with PLZT.

It is believed that heating of the specimen during ion milling caused the loss of PbO from the near-surface region. In some cases, transformations occurred while the specimens were under observation in the electron microscope. In that case, beam heating of the specimen could have been the cause. These

observations have implications for annealing experiments on PLZT. If annealing is used to diffuse certain elements into the structure, then care must be taken to assure no loss of Pb and subsequent transformation of the structure.

### 5.3 MECHANICAL STRESS AND CURVATURE

The PLZT-wafer curvature was measured interferometrically using a grazing-incidence laser interferometer with variable fringe sensitivity from 0.1 to 5  $\mu\text{m}/\text{fringe}$ . A vacuum pen holds the fragile wafer and allows tilting as well as translation of the wafer toward and away from the optical flat to produce the most symmetric (and hence simplest to interpret) fringe pattern. Fringe spacing was calibrated using NBS specifications. The interferograms were displayed on a TV monitor and could be photographed for permanent records.

Curvature measurements can be used to deduce mechanical stress distribution in a coating or implanted layer using the following relation (Refs. 10 and 11):

$$S = [E_p/3(1 - \nu_p)] [t_p^2/t_c r_p^2] d \quad (5)$$

where

$S$  = the stress in the coating or implanted layer

$E_p$  = Young's Modulus for PLZT ( $6.3 \times 10^{11}$  dynes/cm)

$\nu_p$  = Poisson's ratio for PLZT (0.3)

$t_p$  = the PLZT thickness

$t_c$  = the coating or implanted layer thickness

$r_p$  = the PLZT ratio

$d$  = the PLZT deformation (edge displacement versus center) caused by stress in the coating or the implanted layer.

The same equation was also used later to estimate stress in the ITO coating when the deformation,  $d$ , was caused by application of a voltage to the two ITO electrodes. A concave curvature of the coated or implanted side corresponds to a tensile stress in the coating, and a convex curvature to a compressive stress. Curvature could be determined by the inward or outward motion of the fringes when the substrate was moved away from the optical flat. The substrate deformation,  $d$ , was measured by counting fringes and multiplying by the fringe sensitivity.

Curvature measurements were made during the processing steps on selected wafers from several implantation batches. Wafers were examined as-received (new condition) and after the following processing steps: dicing, implant, anneal, and ITO coating applications. Table 6 summarizes the results for three wafers from one implantation batch. The results and those obtained for other batches of wafers lead to the following conclusions:

- As-received, 1-in square, new, hot-pressed wafers have a slight curvature before dicing. All are saddle-shaped, with curvatures ranging from 0.25 to 3.3  $\mu\text{m}/0.25$  in. The implant-introduced curvature could be reduced by identifying and implanting the concave side of each wafer.
- Implants introduce a large curvature. The implanted side of the wafer is always convex, indicating a compressive stress in the implanted layer. The magnitude of the compressive stress is dependent on ion species, energy, and implant flux. Values observed ranged from 10 to 50  $\mu\text{m}/0.25$  in. Figure 22 is a sketch of how the implanted layer appears if these curvature results are combined with the results of the spectrophotometric studies.
- An ITO coating on the implanted face adds a small tensile stress which partially cancels the curvature introduced by the implanted layer, but it is not large enough to help much. The implanted-layer compressive stress is typically 100 times larger than the ITO-tensile stress. The ITO coating the other side of the wafer cancels the effects of ITO on the first side coated so that the ITO has no net affect on wafer curvature.
- The PLZT and ITO are well matched in thermal-expansion coefficient ( $\approx 5 \times 10^{-6}/^\circ\text{C}$ ), so that there is no temperature-dependent curvature of the wafer expected from the ITO coating.

A 10-h, 200°C, air anneal removes the very large and significant implant-induced curvature. Table 7 and Fig. 23 illustrate the beneficial effects with numbers and interferograms. Curvature (stress) is reduced to the level of new wafers.

#### 5.4 PLZT CURVATURE VERSUS APPLIED VOLTAGE

The interferometer described above was adapted for measurement of wafer deformation when a cyclic voltage (ca. 400 V) is applied to the ITO coatings. The ITO-coated wafer was held by the center of one face with the vacuum pen, close to and parallel to the optical flat. One lead of a dc-voltage supply was attached to the vacuum pen, which in turn contacted the ITO coating on one

TABLE 6. PLZT Curvature<sup>a</sup> (Mechanical Stress) versus Processing Step Case:  $1.0 \times 10^{15}/\text{cm}^2$  500 KeV  $\text{Ne}^+$  plus  $1-1.7 \times 10^{15}/\text{cm}^2$  1.4 MeV  $\text{Ni}^+$ .

Wafer <sup>b</sup> Number	Initial <sup>c</sup>	After <sup>d</sup> Implant	After ITO <sup>e</sup> on Implant	After ITO <sup>f</sup> on Other Side
C-13(1)	+1.3	-10.2	-9.4	-10.9
C-13(2)	+1.2	-10.4	-10.2	-10.2
C-13(3)	-1.5	-10.8	-10.1	-10.8

<sup>a</sup>Micrometer deflection edge versus center. (-) means implanted side convex, (+) means concave.

<sup>b</sup>0.5 x 0.5 inch, 90/65 PLZT.

<sup>c</sup>All are identical. Side selection is arbitrary at this point.

<sup>d</sup>May vary with implant species, density, and energy.

<sup>e</sup>Expected ITO contribution is +0.2.

<sup>f</sup>Coating both sides with same thickness produces no net change in curvature.

TABLE 7. Reduction of implant-induced wafer curvature by 200°C, 10-h, air anneal. (Curvatures in micrometers per quarter inch<sup>a</sup>.)

WAFER NUMBER	STEP	CX	C-X	CY	C-Y	CAVE
9/13A	BEFORE	-6.66	-5.33	-30.0	-18.6	-15.1
	AFTER	+2.80	+3.20	+3.20	+3.12	+3.08
9/14B	BEFORE	-3.39	-1.70	-27.1	-20.3	-13.1
	AFTER	+4.16	+6.00	+4.00	+4.80	+4.74

<sup>a</sup>The - means implant side convex, + means implant side concave.

side of the wafer. The other lead was attached to a thin flexible lead cut from copper adhesive tape and attached to the corner of the ITO coating on the other side of the wafer. When a voltage was applied, the wafer distortion was immediately recorded in the displayed interferogram.

Three wafers from different implant batches were examined. Figure 24 shows the recorded interferograms and the measured curvatures (in micrometers per quarter inch) for a wafer cycled from 0 to +400 V, back to 0 V, from 0 to -400 V, and finally back to 0 V again. Two other wafers showed similar results.

The initial curvature is  $\approx 4 \mu\text{m}/0.25 \text{ in}$  (convex), the residual curvature after the 10-h, 200°C, air anneal. The wafer flattens with increasing voltage applied to the implanted side as the ferroelectric domains align. The polarization remains when the voltage is reduced to zero. With increasing negative voltage, the polarization is cancelled, and the convex curvature returns. The hysteresis behavior associated with polarization and depolarization of the ferroelectric material thus manifests itself in the curvature-versus-applied-voltage curve. Instead of returning to the starting curvature when the voltage is reduced from -400 to 0 V; however, an abnormal flip/flop occurs at large negative voltages which abruptly changes the wafer curvature. In at least one case, the curvature abruptly changed from convex to concave.

The stresses experienced by the ITO coatings as the wafer changes curvature ( $\pm d$ ) with applied voltage can be calculated using Eq. 5. Figure 25 shows the results for the ITO-coated wafer of Fig. 24. This particular wafer was annealed after the ITO coatings were applied. Thus, the ITO coatings experience a stress of  $\approx 200 \times 10^8 \text{ dynes/cm}^2$ , even before the voltage is applied, because of the anneal-induced wafer-curvature change. It should be noted that when one coating is put into compression, the other is put into tension. The curves are not exactly symmetric about zero stress because of the  $20 \times 10^8 \text{ dynes/cm}^2$  tensile, intrinsic stress in the ITO coating. As the voltage is cyclically varied, the ITO coatings experience varying values of compressive and tensile stresses.

The following important conclusions were obtained from these curvature-versus-voltage measurements:

- During a normal hysteresis loop, the ITO stress is controlled by the PLZT curvature's voltage dependence. The ITO stress can be minimized only by minimizing the + and - voltages used.
- Implantation-induced stress does not affect ITO stress during the normal hysteresis loop. However, it may be responsible for the abnormal and potentially catastrophic mechanical flip/flop which occurs at high voltages.
- The ITO coatings on opposite PLZT surfaces experience almost equal stresses of opposite sign.
- The ITO in compression will buckle or lift off if the PLZT/ITO adhesion is exceeded. The ITO in tension will crack and pull apart if the ITO tensile strength is exceeded. No ITO failures were observed. This means ITO/PLZT adhesion was good, and the tensile stresses did not exceed the tensile strength of ITO.

### 5.5 TRANSMISSION MEASUREMENTS

Transmission measurements were performed on the PLZT for several purposes. In FY 1986, a series of transmission measurements of substrates was performed to determine the uniformity of the raw material and the materials at various processing steps. These measurements were performed on 70/65 samples provided by the Air Force. Selected transmission plots in Figs. 26 through 29 show the expected 70/65 transmission cutting off at  $\approx 400$  nm and relatively flat at  $\approx 70$  percent. Implanted samples show a 90 percent transmission peak at  $\approx 1100$  nm to 1200 nm, and a gradual falloff to  $\approx 40$  percent to 50 percent at 2500 nm. For comparison, Fig. 30 shows the transmission of the 70/30 raw material.

Additionally, transmission studies were performed to evaluate the effects of implantation. For this purpose, transmission scans from 350 to 800 nm were done on a number of wafers at several key processing points: initial (new) condition, after implant, after anneal, and after ITO coating on both sides. Scans from 800 to 2800 nm were used on one sample from each implantation batch to characterize the implanted layer. Transmission measurements were made with a spectrophotometer.

Transmission after implant was always smaller than it was when the wafer was in the as-received condition, with the greatest differences in the 350 to 500 nm range and almost no difference beyond  $\approx 800$  nm. The transmission spectra of implanted samples always displayed a small amplitude ( $< 2$  percent) oscillation

because of the different refractive index of the implanted layer. The oscillation was easiest to discern and analyze at wavelengths from 1000 to 2000 nm (Fig. 31).

A 10-h anneal at 200°C in air always restored transmission to as-received values and in some cases improved transmission in the 350 to 500 nm range. The effect of the ITO coatings on transmission is described in Section 3.0, Paragraph 3.1.

#### 5.6 IMPLANTED PLZT REFRACTIVE INDEX, DENSITY, AND THICKNESS

After ion implantation of a PLZT wafer, an oscillation is observed in the wafer's transmission spectrum. The oscillation is caused by the differing refractive indices of the implanted and unimplanted regions and results from constructive and destructive interference of light reflected from the air/layer and layer/wafer interfaces whenever the implanted-layer optical thickness equals quarter wavelength multiples. The refractive index and thickness of the implanted surface layer on the PLZT wafer can be estimated quickly and reliably from spectrophotometer scans.

If the implanted layer is assumed to be altered uniformly in depth, any of the many analysis techniques for a single-layer optical coating on a substrate of known optical properties can be used. Using the envelope technique (Ref. 12), for example, the refractive index of the implanted layer can be calculated from simple equations using the maximum and minimum transmission values in the oscillatory spectrum (Fig. 31) plus the refractive index of the unimplanted PLZT (2.55 near 1000 nm). Transmission spectra in the infrared region of 1000 to 2800 nm are best to use to avoid short wavelength dispersion and any transmission loss introduced by implantation.

Once the refractive index,  $n$ , is calculated, the depth or thickness,  $t$ , of the implanted layer can be estimated by numbering the transmission spectrum extrema according to the relation:

$$4nt = m\lambda_m \quad (m = 1, 2, 3, \dots) \quad (6)$$

where  $\lambda_m$  is the wavelength of the extremum. The extremum numbering is simplified by remembering that transmission peaks are even integers when the



layer has higher refractive index than the unimplanted PLZT and odd integers for the reverse situation.

The density of the implanted layer relative to unimplanted PLZT can be crudely estimated from the refractive index using the simple relation:

$$\% \text{ density} = (n - 1)/(n_0 - 1) \quad (7)$$

where  $n_0$  is 2.55 at 1000 to 2000 nm. More accurate estimates could be made using the results of effective-medium theory (Ref. 13).

In all wafers examined, wafer transmission was enhanced over unimplanted PLZT and maxima occurred at odd-numbered wavelengths. Thus, the implanted layer was always lower in refractive index and density than unimplanted material. Representative values for some of the implants are listed in Table 8.

TABLE 8. PLZT implanted-layer characterization.

PLZT SAMPLE NUMBER	IMPLANTS	REFRACTIVE <sup>a</sup> INDEX		RELATIVE DENSITY (%)	THICKNESS ( $\mu\text{m}$ )	STRESS <sup>b</sup> ( $10^8$ dynes/cm <sup>2</sup> )
B7(1)	1.4 MeV O+ 1.4 MeV Ni+	( $2 \times 10^{15}$ ) ( $1 \times 10^{15}$ )	2.44	94	1.18	570(C)
M5	500 KeV Ne+ 1.4 MeV O+	( $1 \times 10^{15}$ ) ( $2 \times 10^{15}$ )	2.45	94	1.14	612(C)
4B	500 KeV Ne+	( $1 \times 10^{15}$ )	2.29	83	0.67	250(C)
7/23A	1.3 MeV Ne+ 1.4 MeV Cr+	( $2 \times 10^{15}$ ) ( $8 \times 10^{14}$ )	2.45	93	1.20	22(C)
7/25B	1.3 MeV Ne+ 1.3 MeV Al+	( $2.4 \times 10^{15}$ ) ( $1 \times 10^{15}$ )	2.43	92	1.2	18(C)

<sup>a</sup> Index for unimplanted wafer is 2.55  
<sup>b</sup> C = compressive

Implanted-layer refractive indices range from 2.29 to 2.45 compared to unimplanted values of 2.55. These reduced indices correspond to densities of 83 to 94 percent, suggesting that ion implantation introduces a considerable network of voids.

Thicknesses estimated from the interference patterns agree well with those estimated from stopping-range calculations for energetic ions impinging on a solid. The optically determined depth is just beyond the maximum in the calculated damage-versus-depth curve.

### 5.7 PHOTOSENSITIVITY MEASUREMENT

In January, 1987, a sample of 7/65/35 PLZT was implanted with  $O^+$  ions in a test to determine if photosensitivity was enhanced. At that time, PNL was not prepared to make measurements of the type being made at SNL. A single 1-cm<sup>2</sup> sample was produced and sent to the Air Force for evaluation by SNL. It showed not only an enhanced photosensitivity, but also a flatter spectral response. The plot shown in Fig. 32 is a characteristic curve of the implanted sample. An image of a 50-line per inch Ronchi grating was recorded on this sample. The image and its interferogram are shown in Fig. 33.

Some experiments were performed to measure diffraction efficiency using a Ne/Ni coimplant, sample number 9/18B [previously numbered C13(2)]. A 300-line-per-inch Ronchi grating was contact printed to the sample using a 90-mW exposure at 468 nm to 200 V and 25 percent integrator voltage. This gave a faint image which, when used to diffract a 3-mW HeNe beam, resulted in the diffraction pattern shown in Fig. 34. The first diffraction peak is at  $\approx 1$  cm at a distance of 104 cm giving a diffraction angle of  $\approx 10$  mrad. The second order was not visible, and, as seen in the figure, was not recorded. In subsequent similar tests, comparable results were obtained. In one instance, measurement of the relative optical power yielded  $\approx 3$  to 5 percent. In another test, the sample was lightly coated with Al to enhance reflection and the relative optical powers were 1.5 to 1.8 percent on reflection compared to 2.2 to 2.3 percent for transmission through the uncoated sample.

In a third test, using the  $Ne^+/O^+$ -implanted sample 9/19B, 30 mW/cm<sup>2</sup> at 468 nm, the voltage was ramped to 200 V and held for 2 min. The center of the sample was probably overexposed, but the outer portions recorded the 300-line-per-inch Ronchi grating. Figure 35 shows the diffraction pattern using a 25-mW HeNe laser. The second-order diffraction peaks are clearly visible. Previous samples were rechecked with the 25-mW laser and the second orders were still not visible. The relative power of the orders was not measured with this sample.

The first measurements made using the the clone of the SNL system were of sample number 9/17C, an  $O^+/Ni^+$  implanted sample. The data are shown in Fig. 36 and expanded in Fig. 37. Since this was part of an early experimental series for the development of the measurement system, no detailed analysis was performed.

Beginning in May, 1987, most of the implants were characterized for photosensitivity by a series of hysteresis-curve traces at several wavelengths and several laser intensities. Figures 38 through 40 show three of these sets of curves, each of which represents a single wavelength at zero and three non-zero laser intensities for sample 9/13C, a  $Ne^+/Ni^+$  implant. Figure 41 shows a summary of the data, plotted as coercive-voltage-versus-exposure-level, along with sample 9/22B, a  $Ne^+$ -diffused- $Al^+$  implant, for comparison. Later, Fig. 42 was generated repeating the data on sample 9/13C, but adding other wavelengths and a plot of SNL data.

In July, 1987, 7/70/30 composition samples in the 7/24 series were implanted with  $Al^+$  and  $Ne^+$ , and sample number 7/24A was characterized for photosensitivity. The characterization was done at zero and three other nonzero intensities at seven wavelengths from 476 nm to 676 nm. The hysteresis curve at 476 nm is shown in Fig. 43, for reference, and the summary plot for the sample showing change in coercive voltage as a function of wavelength is shown in Fig. 44.

The previous sample was then annealed for 1 h at 300°C in air, and a set of sensitivity data was taken. Figure 45 shows the data for 476 nm for reference and Fig. 46 shows the summary curve. Notice the difference in the shape of the curve and that only 0 and 20 mW exposures were used. Also notice in the summary curve that the sensitivity has dropped overall, but that there is also a single anomalous point.

In August, 1987, the second set of 7/70/30 samples was completed with an  $Ne^+/Cr^+$  implant. Sample 7/23D was characterized. Again, Fig. 47 for a wavelength of 476 nm is shown for reference, and Fig. 48 gives a summary of the photosensitivity. It is important to note that, in this case, the vertical axis is the change in coercive voltage per unit change in recording-beam intensity. The result is that these numbers should be multiplied by 20 mW to be directly comparable to those in previous figures. In this case, the data were extended

to 1500 nm by using an arc lamp for wavelengths beyond 676 nm. From this plot, it is clear that the sensitivity vanishes at  $\approx 1000$  nm.

Characterization of the triple-implanted Ni samples, series 9/20, was attempted; but it was clear that the saturation voltage could not be attained without taking special care to avoid arcing. Figure 49 shows the characteristic curves at 0 and 50 mW at 476 nm. The curve represents a maximum applied voltage of 500 V. Figure 50 shows the equivalent curve at 676 nm.

In FY 1988, the Characterization Task was primarily intended to provide characterization of implanted samples, to support the modeling effort, and to verify improvements in implantation uniformity resulting from adjustments in the implantation hardware.

As discussed in the section on the Implantation Task, there were two major groups of samples implanted in FY 1987. The first were implanted with Ni ions having energies of  $\approx 2$  MeV. This implantation was intended to test modifications in the beam line which were implemented for better implantation uniformity over the area of the wafer. Figures 6 and 7 show some of the results of those implantations, illustrating various degrees of uniformity.

The second set of implants were dual implants of  $C^+$  and  $O^+$ . Carbon was selected as representing a relatively easy implantation with electronic properties that should improve photosensitivity. Oxygen was implanted partly based on past improvements caused by  $O^+$  and partly in support of early FY 1987 findings.

The spectral photosensitivity of samples from both batches was measured using the previously established technique of measuring coercive voltage versus input optical power at each of a set of selected wavelengths. The optical source was a Kr-ion laser providing a selection of spectrally pure, high-power spectral lines throughout the visible spectrum. Selected plots of results are shown in Figs. 51 and 52.

Compared to results performed in FY 1986, sample 9/12C shows ca. 50 percent smaller peak sensitivity (at  $\approx 480$  nm) than sample 7/23D, but sample 9/11B shows ca. 50 percent greater sensitivity. The host materials differ slightly, and the implant species differ. Sample 7/23D is 7.6/70/30 PLZT implanted with

Ne and Cr, while 9/11 and 9/12 (in spite of the numbering convention which implies 9/65/35 material) are both 7/65/35 material, coimplanted with  $C^+$  and  $O^+$ . Samples 9/11B and 9/12C were implanted with  $O^+$  ions at differing energies, and thus to different depths. Sample 9/11B, with the better photosensitivity, was implanted with  $O^+$  at 2.0 MeV resulting in its coming to rest at about the same depth as the  $C^+$ ,  $\approx 1.5 \mu m$ .

The cause of the difference in responsivity between samples 9/11B and 9/12C is not obvious. The difference appears to be a result of the difference in implantation energies of the  $O^+$  ions. The energy for the  $O^{3+}$  ions used for the 9/12C sample is more than twice as large as for the  $O^+$  ions used for sample 9/11B. The result is that the damage region is deeper for the 9/12C sample than for the 9/11B sample, as shown in Fig. 53, but the damage induced along the path of the ions is less for the higher energy  $O^{3+}$  ions. It is known that (1) the maximum damage level in the  $C^+-O^+$  implants is still less than in sample 7/23B, a  $Cr^+-Ne^+$  implant, and (2) the depth of damage is much greater in the  $C^+-O^+$  implants. Apparently both the magnitude and the spatial extent of the damage must be important; but the relative significance of these two factors in photosensitivity enhancement is not yet understood.

If all other parameters were equal, according to SNL model, the switching potential in illuminated areas would be greater for the 9/12C than for the 9/11B, at a given applied potential. Relative photoconductivity curves for the two samples look quite similar, but the photocurrent for a given incident optical power is measurably greater over the region of the spectrum for which the sensitivity measurements were made.

## 5.8 OPTICAL PROPERTIES

In addition to the photosensitivity measurements in FY 1987, the utility of measuring spectral photoconductivity and photoacoustic-like response was tested. For these measurements, a 150-W, Xe-arc lamp was used as a source, providing a continuous spectrum from 300 to 2500 nm. Individual wavelength regions were isolated using narrow band-pass interference filters throughout the range from 300 to 1050 nm. Samples from both coimplant batches were measured to provide a test of the method and to provide data to support the modeling activity. Sample data are shown in Figs. 54 and 55. In the case of

the  $C^{+}-O^{+}$  coimplants, cracking of the substrate limited the number of samples which might actually be useful for additional experiments.

In FY 1988, a direct test of the conclusions from Ref. 8 (Model Development) was performed. To provide this test, photoacoustic spectroscopy measurements were performed on PZT and PZT doped with La and Mn prepared according to Ref. 8 (PLZT Preparation). In order to provide a direct comparison with those results, diffuse-reflectance measurements were also performed in the same fashion. Although the samples appear grossly different, ranging in color from grey to yellow, the photoacoustic spectroscopy measurements (Fig. 56) show no particular structure. (These should be compared with a neodymium-oxide spectrum, Fig. 57, which is used as a standard because of its rich spectrum, with peaks throughout the visible.) No distinctive features identifiable as resulting from the dopants are seen although there are slight inflections in the curves which may be interpreted as indicating the presence of broad peaks. It is clear from these spectra, that the addition of Mn at the 1.50 percent concentration level increases the long-wavelength optical response of both PZT and PZT doped with La, generally flattening out the response. Since photoacoustic spectroscopy measurements are strictly relative, no comparison between individual spectra is possible. Repetition of the experiment with newly prepared samples gave similar results. Photoacoustic spectra were also taken of powdered 70/65, unimplanted PLZT. An extremely clean spectrum was found (Fig. 58). There is no structure other than a single peak. These results are consistent with the photothermal-deflection spectroscopy results of Ref. 14 in that the two spectra are basically featureless. (The Ref. 13 data are redisplayed in logarithmic form so the main peak is also washed out; however, careful inspection of the figure shows that a peak is there, also.)

The diffuse-reflectance spectra are shown in Fig. 59. These are similar to those of Ref. 8. Again there is some weak, reproducible structure. These data confirm that the addition of Mn increases the long-wavelength absorption of the material.

As a result of these experiments, it became evident that better information on the electronic effects of substituents can be obtained by the photoconductivity and pyroelectric approaches tested in FY 1987. The pyroelectric measurement is, basically, an extremely sensitive photoacoustic measurement.

In the more conventional photoacoustic spectroscopy (for instance, that which was used above) the absorbed light heats the sample and the heated sample heats the surrounding gas resulting in a pressure wave. This pressure wave is detected by a microphone in the cell. In the case of the pyroelectric measurement, the absorbed light changes the polarization of the poled sample, creating a signal directly.

Consequently, measurements on virgin and implanted samples of PLZT were initiated. The experimental system consisted of a 1-kW Xe-arc lamp, a double monochromator, a rotary chopper, a pyroelectric radiometer, and a lock-in amplifier. The monochromator and data collection functions were computer controlled. The spectrum of the Xe-arc lamp was monitored and the data corrected for the intensity of the lamp. A spectrum of the lamp is shown in Fig. 60. The pyroelectric and photoconductivity measurements were performed in the plane of the sample; the sample was poled in the conventional geometry (perpendicular to the plane of the sample) and illumination was perpendicular to the plane of the sample. Electrical contact was effected using conducting paint. This geometry allowed a large number of degrees of freedom so that the results of the pyroelectric experiments were neither amenable to interpretation nor particularly repeatable.

Thus, the geometry was changed. The sample was gold-coated on both sides (not connected) with a masked area (smaller than the sample thickness) which would be illuminated. The sample was then poled in the plane of the sample. Experiments were performed with illumination perpendicular to the sample. This geometry gave reliable and repeatable results with virgin samples. Figures 61 and 62 show the experimental results for one of these samples, 7/51. These results were repeatable over a period of several months if the sample was repoled to a standard condition. Additional assurance of the accuracy of this method is provided by the fact that the spectrum is independent of the side being illuminated.

For the virgin sample, the pyroelectric spectrum shows two reasonably distinct peaks at  $\approx 365 \mu\text{m}$  and  $475 \text{ nm}$ . The photoconductivity spectrum shows one distinct peak at  $\approx 365 \text{ nm}$  with a much weaker peak at  $475 \text{ nm}$ . There is a hint of a smaller peak at  $\approx 400 \mu\text{m}$ .

Figure 63 shows the pyroelectric spectra for sample 9/10B, an  $O^{3+}$  and  $C^+$  double implant from both the implanted and nonimplanted side. The non-implant-side spectrum is that characteristic of the virgin sample; the implanted-side spectrum shows a shift of the two peaks, the higher energy peak being shifted to lower energies and the lower energy peak being shifted to slightly higher energies. There is a suggestion of the ca. 410 nm peak in the nonimplanted side. Figures 64 and 65 show the pyroelectric spectrum from the nonimplanted and the implanted side, respectively, of sample 9/21B, a triple- $Ni^+$  implant. The low-energy peak in each signal is less distinct than in the other samples. In this case, the higher-energy (shorter-wavelength) peak is also shifted to lower energy, but it is difficult to make any definitive statement about a shift of the lower-energy peak. Figures 66 and 67 show the pyroelectric spectra of sample 9/18B, an  $Ne^+$ ,  $Ni^+$ , double-implant. Here again, the higher-energy peak is shifted, broadened, and reduced in peak amplitude in the implanted-side signal compared to that in the nonimplanted side signal. Figures 68 and 69, respectively, show the pyroelectric spectra for sample 9/10A, a  $O^+$ ,  $C^+$  coimplant. The spectra show that this sample and 9/18B were mislabeled somewhere along the line. The original labeling interchanged the implanted and nonimplanted sides. Depending on when the mislabeling occurred, this may explain the poor sensitivity of sample 9/18B to writing of a Ronchi grating. See the discussion relating to Fig. 34.

These spectra are similar to those for the other samples with the exception that the ca. 475 nm peak appears to have split into two peaks in the non-implanted side. For the implanted side, the lowest-energy peak appears to be the survivor and the higher-energy peak is significantly shifted to longer wavelength.

The pyroelectric spectra are extremely informative, but yield limited specific information as to what is actually happening in the material. Additional information is obtained by examining the photoconductivity spectra. Figures 70 through 77 show the photoconductivity spectra of the nonimplanted and implanted sides, respectively, of samples 9/10B, 9/21B, 9/18B, and 9/10A. The photoconductivity spectra were measured for 50, 0, and -50 V applied for each sample. A clear characteristic of each of these spectra is that the higher-energy peak is sensitive to the sign of the applied voltage while the lower-energy peak does not display this characteristic. These spectra were measured with the lock-in amplifier using autophasing and thus show the absolute value



of the signal. Measurements which give the sign of the photoconductivity measurement signal show that the signal is positive for positive applied voltage and is negative for negative applied voltage (Figs. 78 and 79). Note also that the location of this peak is sensitive to the applied voltage (Fig. 80). To understand this behavior, it is appropriate to consider exactly what the experiments are measuring.

The schematic electrical layout for the pyroelectric measurements is shown in Fig. 81(a); that for the photoconductivity measurements is shown in Fig. 81(b). The poled ferroelectric PLZT has a permanent polarization. When there is no voltage applied to the sample, the electrical displacement across the sample vanishes so there is an electric field in the direction opposite to the polarization. Normally, this field (and the associated voltage) is compensated by charges from the environment (Ref. 15). When the sample is heated, the crystal expands, the polarization changes, the associated field changes, along with the potential across the sample. The last potential is the pyroelectric signal that is measured.

In the photoconductivity mode, the sample is in series with a variable voltage power supply. The observed signal is proportional to the current through the load resistor. The voltage driving the current through the load resistor is a sum of that provided by the power supply and that provided by the pyroelectric effect. (The currents involved in these experiments are extremely small, on the order of tens to hundreds of picoamps. Thus, distributed impedances and input impedances of the measuring equipment are not negligible.) In an attempt to disentangle these, the light chopping was performed manually and the lock-in amplifier was replaced by an electrometer. Typical results are shown in Fig. 82. These show that there is no dc photoconductivity.

In view of these experimental observations, the data can be explained by the following. A poled ferroelectric develops a shielding surface charge  $\sigma$ , positive on the positive pole, just cancelling the "displacement charge"

$$\sigma_o = P \cdot n \quad (8)$$

where  $p$  is the polarization and  $n$  is the outward normal to the surface (Fig. 83a). In the interior of the ferroelectric, there is an electric field,  $E$ ,

opposing  $P$ , so that the displacement  $D = E + 4\pi P$  is zero. When the ferroelectric is heated, the original lattice expands,  $P$  changes to  $P'$ ,  $E$  changes to  $E'$  (to oppose  $P$ ), and  $\sigma_o$  changes to  $\sigma'_o = P \cdot n$ . The shielding surface charge  $\sigma$  does not balance the displacement change and a voltage signal appears (Fig. 83b). This is the pyroelectric signal.

Now consider the situation in which a voltage is applied across the poled ferroelectric (Fig. 83c). Inside the ferroelectric, the polarization is

$$P = P_o + \alpha E_I \quad (9)$$

where  $E_I$  is the interior field. Now, the electrical displacement  $D$  (identical to the applied field) is related to the polarization and interior electric field by

$$D = E + 4\pi P \quad (10)$$

where

$$P = \frac{P_o + \alpha D}{1 + 4\pi\alpha} \quad (11)$$

Thus, when the light is adsorbed, two outcomes are possible. The first possibility is one in which the excitation (absorption) changes the induced moment, but does not affect the polarizability. In this case, the signal will be independent of the applied potential. In the second case, the excitation changes the polarization as well as the induced moment. In this case, the signal will be sensitive to (the magnitude and sign of) the applied voltage.

The conventional understanding of the perovskites is that the remanent polarization is associated with displacement of the  $O^+$  ions. Because Pb and  $O^+$  vacancies provide room for the implanted ions to reside, either of these can be associated with the peak at ca. 365 nm. An interpretation of the experimental results is given in Model Development Section.

## 6.0 MODEL DEVELOPMENT

The approach to developing a working model for the behavior of this material focussed on a literature search, an attempt to construct a crude conceptual model of the electronic-band structure of PLZT, and experimental work to provide calibration of that conceptual model. Because the chemistry of this material is very complicated and is a significant determinant of the electronic structure and behavior, a working model for the chemistry of the material is integral to an understanding of the optical behavior. The experimental work is reported in Section 5.0 of this report. The driving force behind this effort was the goal of understanding the behavior of PLZT at the electronic level so as to identify ways of improving the long-wavelength sensitivity of this material for use in a phase-conjugation mode.

### 6.1 LITERATURE SEARCH

An extensive literature search was conducted to identify prior theoretical or experimental work which analyzes the electronic-band structure of PLZT or PZT, or work from which this information might be obtained. The latter search category included a search for studies of the optical properties--refractive index, dielectric response, optical absorption, photoconductivity, or similar properties--as a function of wavelength from which information about the electronic structure may be inferred.

A large amount of information referred to how applications (including optical applications) of these materials were affected by composition and other factors; wavelength did not appear significant as a variable. Several references (notably, Ref. 16) on the electronic structure of materials similar to PZT ( $\text{BaTiO}_3$  and  $\text{SrTiO}_3$ ) called attention to the dearth of theoretical guidance for understanding the optical properties of these materials and especially those with substituted atoms (dopants).

Reference 8 specifically dealt with the influence of dopants (La and Mn) on the electronic-band structure of PZT. References cited in Ref. 8 either appeared to be not specifically applicable to the objectives of this work or were published in Czechoslovakian journals. Since there is no evidence that those references would significantly contribute to an understanding of PZT, they were not pursued. The experiments mentioned in Ref. 8 were repeated

using a more direct measure of the electronic absorption with somewhat differing results.

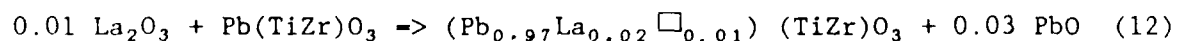
Several works were found that referred to the electronic band structure of similar perovskite materials. Some useful information related to the chemistry of these materials. These sources provided the basis for constructing a conceptual model of the electronic structure of PLZT.

Based on what was learned from these references, direct calibration of the conceptual model by measuring the optical absorption of PLZT and implanted PLZT was performed. These are discussed in Section 6.3.

## 6.2 THE CHEMICAL MODEL

The presence of the empty impurity band needs some explanation. This requires an understanding of what happens when the La--or some other dopant--is added to the PZT during fabrication. Note that during fabrication, the material is brought to equilibrium at temperatures of  $\approx 1300$  K to effect mixing. Cooling freezes in many of the effects of this high temperature equilibrium, including nonstoichiometries. If it were possible, low-temperature fabrication could change the situation described here.

Reference 17 claims that the stoichiometry of PZT self-compensates by the adjustment of Pb and  $O^+$  numbers (through self-compensating vacancy formation). This view is supported by the fact that there is no evidence of B-position vacancies in  $ABO_3$  compounds. The  $ABO_3$  compounds are well-known to be highly tolerant of A- and O-position vacancies. The reaction upon the addition of La (for instance) is:



The essential feature of this reaction is the volatility of the PbO, released during the firing process. Support for this reaction is provided by the fact that PLZT grain boundaries appear to be Pb-rich. Since unmodified PZT is p-type (the conductivity drops by about three orders of magnitude through the addition of 0.1 atom percent of La and changes little on addition of greater quantities of La), the reaction described above is interpreted as a differential one, occurring after the acceptor states have been filled (after the

first 0.1 atom percent of La is added). This reaction can be changed. Reference 18 determined that, in an environment in which the PbO is free to evolve, addition of 8 molar percent of La to PZT results in extrinsic lattice vacancies forming on both the Pb and Ti/Zr sublattices in a 10:3 ratio; intrinsic vacancies form on both the Pb and O sites. Reference 19 also found that the vacancy location could be controlled by controlling the atmosphere. In a PbO-rich environment, Pb loss was reduced and charge neutrality was maintained by formation of Ti/Zr vacancies in addition to the Pb vacancies. In a PbO-poor environment, the vacancies locate only on Pb sites.

The situation is further complicated. The addition of trivalent materials in place of tetravalent materials (Ti,Zr) tends to increase the hole concentration. Experimentally, it is found that this increase is limited to about an order of magnitude by the formation of  $O^+$  vacancies according to the reaction:



Reference 17 likens this situation to a doubly buffered aqueous system formed by a weak acid and a weak base: Adding '...a strong base leads only to moderate "basicity" [electron concentration] as the weak "acid" Pb is neutralized and expelled. Addition of a strong acid leads only to moderate acidity [hole concentration] as the "base"  $O^+$  is expelled.'

According to Ref. 17, doping PZT does not appear to be an effective method for creating additional occupied optically absorbing states below the cutoff. There is some evidence to counter this general dictum. As noted, Ref. 8 considered the situation in which PZT is lightly doped with La (replacing Pb) and Mn (replacing Zr,Ti). Four stoichiometries were considered. (1) Nominally pure PZT, (2) PZT + 0.015 Mn, (3) PZT + 0.015 Mn + 0.015 La, and (4) PZT + 0.015 Mn + 0.045 La (i.e., PZT doped at the 1.5 and 4.5 percent levels). The interpretation of the Ref. 8 reflection measurements is as shown in Fig. 84. Many special efforts were made to limit the release of PbO during material fabrication. This may clarify the apparent conflict between the Ref. 8 results and the Ref. 17 observation of self-compensation.

The important point to note is that when the La concentration is equal to or greater than the Mn concentration, the  $Mn^{+3}$  state appears to be at least partially occupied.

### 6.3 THE ELECTRONIC MODEL

Based on work related to the electronic-band structure of similar materials (principally,  $\text{BaTiO}_3$  and  $\text{SrTiO}_3$ ), the electronic-band structure of perovskite materials have some simplifying features. The electronic structure in  $\text{ABO}_3$  compounds (e.g., PZT) is such that the  $\text{BO}_3$ -complex wave functions, originating as d-states of the B ion and p-states of the O ion, overlap little with the A atom. Thus, the bands originating from the A ions are, to a first approximation, simply additive (taking into account the Madelung potential) to the  $\text{BO}_3$  electronic states.

There is yet another simplification. As noted, band structures have been calculated for some of the  $\text{ABO}_3$  materials. This simplification appears when the results of those calculations are studied. The general method used in such calculations "...are carried out in three stages. In the first stage, the augmented-plane-wave (APW) method is applied to calculate the energy-band results at symmetry points in the Brillouin zone. These APW results are then used to determine various parameters in the Slater Koster Linear Combination of Atomic Orbitals (LCAO) interpolation scheme which is applied to fit the valence- and lowest-conduction-band states. Finally, the LCAO parameters which determine the p-d band gaps in these compounds are adjusted in accordance with optical and cyclotron-mass data" (Ref. 20). Some results adopted from that reference are shown in Figs. 85 through 88.

Figure 85 shows that there is little qualitative difference between quite different materials with the  $\text{ABO}_3$  structure. The primary difference is the totally unsurprising result that if an ion is not present, there are no bands arising from the electronic states associated with the ion. As noted in Fig. 85, the  $\text{O}^{+}$  s-bands and p-bands (that is, the bands arising from the s and p electronic states, respectively, of the  $\text{O}^{+}$  ions) are in approximately the same location for each of the materials. The 3p A bands (that is, bands arising from the 3p electronic states of the A ions) are similarly located in approximately the same relative location. For  $\text{SrTiO}_3$ , for which the 4p states are the relevant ones, the band lies somewhat lower. A reasonable extrapolation to PZT for which the 5p state is the relevant one would be that the band is somewhat lower still. In any event, since the highest-lying valence band will be the  $\text{O}^{+}$  p-band, the A-p bands are almost irrelevant, lying below the valence band.

The electronic-band structure around the band gap then is, simplistically, independent of the B ion (the B-atom-derived states either becoming deep valence states or high-lying conduction-band states). A crude description of the density of states looks something like Fig. 89. Actually, the A and B ions are important in that the number of electrons they contribute determines the filling of the bands. (For instance, the claim is made that the  $O^+$  p states become the valence band. In PZT this is true, but if the band were not filled, the material would be metallic and the band would be the conduction band.)

To see how PZT becomes an insulator, consider Fig. 89. The  $O^+$  2-p states evolve into nine bands capable of holding 18 electrons per unit cell. The Pb 5-p states evolve into three bands capable of holding six electrons per unit cell. The  $O^+$  2-s states evolve into three bands capable of holding six electrons per unit cell. Thus, ignoring the core states, these three band groupings are capable of accepting 30 electrons per unit cell. The Pb contributes two electrons per unit cell; the three O contribute 24 electrons per unit cell, and the Zr and Ti contribute four electrons per unit cell for a total of 30 electrons per unit cell. Thus, the O 2-p band would be just-filled for PZT.) The lowest conduction bands, in each case, evolve from the B atom d-states.

The result is a substantial band gap, the value of which is relatively insensitive to the chemical composition. Reference 17 observes that the PZT conductivity is p-type. The p-type conductivity of unmodified PZT indicates the presence of acceptor states lying near or below the  $O^+$  2-p bands. The addition of La (up to 0.1 atom percent) reduces the hole concentration.

States do lie in the band gap. Even if these states are unoccupied, impurity states will exist. Additionally, there will be electronic states associated with the vacancies in the material. For instance, an  $O^+$  vacancy can trap up to two electrons, thereby forming a  $V_o$ -center.

Progress was made in developing a method for understanding the electronic structure of these materials. Reference 21 developed what amounts to a generic model of the band structure of perovskites. Others have used this theory as a basis for investigating the electronic states of  $O^+$  vacancies and of impurities in these materials. It had been the intent in this work to

build on this approach to: (1) investigate the electronic spectrum of the  $O^+$  vacancy in PZT, (2) determine the effect on the electronic structure of PZT by substitution of La for Pb, (3) investigate the electronic spectra of transition metal substituents at various sites in PZT, and (4) investigate the conductivity of PZT and substituted PZT, as a function of composition, by constructing a Hubbard-like model (derived from the Ref. 21 tight-binding model of the perovskites). It was intended to address, as progress occurred, lattice relaxations and Jahn-Teller effects. This was an ambitious program that would have involved several years of effort; it was intended to incorporate this into the PNL Molecular Science Research Center (MSRC) program. Investigators in that program determined that the effort required to achieve the desired results exceeded the results to be obtained and so this integration did not occur.

#### 6.4 RELATIONSHIP TO EXPERIMENT

Reference 8 examined the reflectance spectrum of PZT lightly doped with La (replacing Pb) and Mn (replacing Zr,Ti). The level structure is reproduced in Fig. 90 (Mn-doping-induced states removed for clarity). Transmittance measurements on unimplanted PLZT samples done by PNL resulted in the data shown in Fig. 91. The transmittance shows a cutoff at ca. 370 nm, consistent with the 365 nm peak seen in the pyroelectric and photoconductivity results.

The FY 1988 pyroelectric and photoconductivity experiments on virgin and implanted samples of PLZT help to calibrate this conceptual model further (Figs. 61 through 77). With minor exceptions, all the nonimplanted-side spectra are similar and appear to be identical to the spectra for the virgin samples. The exceptions are sample 9/21B for which the long-wavelength peak (at ca. 480 nm) is much weaker than the others and sample 9/10A for which this long-wavelength peak is split into two peaks at ca. 460 nm and ca. 490 nm. Pyroelectric spectra of the implanted side are also similar with minor exceptions in that each shows a suppression of the short-wavelength peak and the appearance of a longer-wavelength peak at  $\approx 410$  nm. An exception is sample 9/10A for which the short-wavelength peak is shifted by a greater amount to  $\approx 430$  nm. Based on these data, such a peak shift may be the result of two phenomena or a mix thereof. First, the peak may be moving as a result of the implantation or, second, the peak may simply be suppressed, allowing a weaker peak to appear.



The photoconductivity measurements provide some guidance for distinguishing between these possibilities. (Note that the term "photoconductivity" is a term of convenience and is descriptive of the experimental setup as opposed to the phenomenon being investigated.) For samples 9/10B, 9/21B, and 9/18B (Figs. 70 through 75), there is a hint of a ca. 410 nm peak in the unimplanted-side spectrum, but it is unclear if this is sensitive to the applied bias. On the implanted side, the 365 nm peak is gone and the 410 nm peak is clearly bias-sensitive. For sample 9/10A, the behavior of the two shorter wavelength peaks is quite similar, but the appearance of the strong 460 nm peak in the unimplanted spectrum confounds the interpretation somewhat. These data can be interpreted thusly:

- The ca. 365 nm and ca. 410 nm peaks are both bias-sensitive
- The ca. 365 nm peak disappears as a result of the implantation
- Since the ca. 365 nm peak disappears for all implant species studied, it is a peak associated with a  $V_o$ -center (i.e.,  $O^+$ -vacancy color center)
- Since the ca. 410 nm peak remains for all implant species studies, it is associated with the  $La^{3+}$  substituent.
- The peak in sample 9/10A at ca. 465 nm is unexplained. Because the PLZT is nearly transparent at this wavelength, the appearance of this peak on the nonimplanted side may be an artifact caused by light passing through the sample and exciting a species on the implanted side.

## 6.5 TECHNOLOGICAL IMPLICATIONS

It may be well to recall, at this point, that the overall objective of this project was to increase the wavelength (reduce the photon energy) of the light required to switch the material. This is equivalent to saying that the goal was to increase the wavelength to produce photoconductivity or dielectric relaxation. Briefly, it is appropriate to review why this equivalence exists.

According to Ref. 1, unmodified PLZT has too great a conductivity to apply sufficient field to effect switching. Therefore, ion implantation has been used to cause disorder in the material and, thereby, create traps, in turn reducing the conductivity in the implanted region. An empirical, conceptual model for this behavior has been described in this report, together with the physical implementation of the model. This model appears reasonable and well

justified by experiment. When an area of the material is exposed to light, electrons in that area undergo a transition from the valence to the conduction band, generating photoconductivity in that area and, according to the Ref. 1 model, allowing an image to be stored. As noted, the goal is to increase the wavelength (reduce the energy) of the light required to produce the photoconductivity.

To achieve photoconductivity at longer wavelengths requires the creation of occupied electronic states lying in the band gap. Unoccupied states in the band gap would change the optical absorption by allowing valence-band-to-empty state transitions but would provide no carriers for photoconductivity. In attempting to consider possibilities for introducing mid-band gap states, it is helpful to note first that relatively little flexibility is available for introduction of interstitial ions--there is simply not enough room. Thus, to a large extent, the Madelung potentials experienced by the ions are large. That is, one cannot move  $O^{+}$  2-p states up much by introducing disorder. Similarly, the  $O^{+}$  atoms are well-separated from one another (Fig. 92) so that an  $O^{+}$  vacancy does not change the potential experienced by another  $O^{+}$  atom except in second order.

Recalling that the Pb (and La) states are well-buried, the change in potential associated with  $O^{+}$  vacancies probably does not affect these. A best guess as to the effect of vacancies is that the bands remain nearly unchanged.

Two potential approaches subject to constraints can be identified for creating occupied interband gap states: doping and implantation. As noted above, doping by fabrication at high temperature is accompanied by self-compensation. The Ref. 7 result (and that of Refs. 10 and 19) suggests that, with care, co-doping might be successful. Recent work (Ref. 16) on impurity energy levels in  $BaTiO_3$ , taken together with that of Ref. 8, suggests that Cr and Mn would be interesting choices to co-dope with La.

Regardless of the potential for success of co-doping, implantation will be necessary to reduce the material conductivity. Depending on the nature of the implanted ion and its final resting place, implantation can also affect the absorption of light at wavelengths greater than the cutoff wavelength. Since the perovskite cell is crowded, with little room for added atoms, it is probable that, during heat treatment following implantation (at considerably lower

temperatures than the fabrication temperature), these end up in existing lattice vacancies.

## 7. 0 CONCLUSIONS AND RECOMMENDATIONS

Through the course of this work, a number of conclusions were reached on various aspects of the project. These are as follows:

- Implanted ions locate at  $O^+$  vacancies.
- The biased spectral pyrometry measurements provide a powerful tool for studying the electronic structure of implanted PLZT.
- Sample-to-sample variations may be significant.
- Oxygen implants seem to show enhanced and flattened spectral photosensitivities.
- Stress cracking earlier hypothesized to be caused by a mismatch between ITO and PLZT mechanical properties appears to be due entirely to implantation-induced damage.
- Producing thin-film PLZT of the correct crystalline structure will require elevated substrate temperatures and carefully controlled target composition.
- No fundamental models of the electronic structure for PLZT have been published, but some materials having similar structure may provide an adequate starting point from which an understanding of PLZT may be derived.
- If the published electronic structure of similar materials adequately approximates PLZT, then occupied interband electronic states need to be induced to provide lower energy transitions which will provide conduction electrons resulting from lower energy (i.e., redder) photons.
- Indications are that Mn forms an appropriate intermediate state in similar materials.

For future work in this area, it is noted that the biased spectral pyrometry presents a powerful way of probing the electronic structure of PLZT. This material is extremely complicated, having five elemental constituents. In order to get the kind of information required to understand the electronic structure, a detailed study of compositions varying over the stability range would be appropriate, with a sufficient number of samples to eliminate sample-to-sample variations. Additionally, implanted, doped, and/or diffused samples should also be studied but with one substituent at a time to reduce the probability of confounding interpretation. Because there is a possibility that light may be passing through the samples, thicker samples might be used.

Finally, the cause of the ca. 460 nm peak in sample 9/10A should be determined. The original reason for the implant with  $C^+$  was that neutral  $C^+$  has the same electronic configuration as  $O^{2+}$ , thus, substituting neutral  $C^+$  into an  $O^+$  vacancy may give a red-shifted  $V_O^{2+}$ -center (because of the repulsion by the C core electrons). If interest remains in shifting the response of PLZT to the red, the anomaly of sample 9/10A should be pursued.

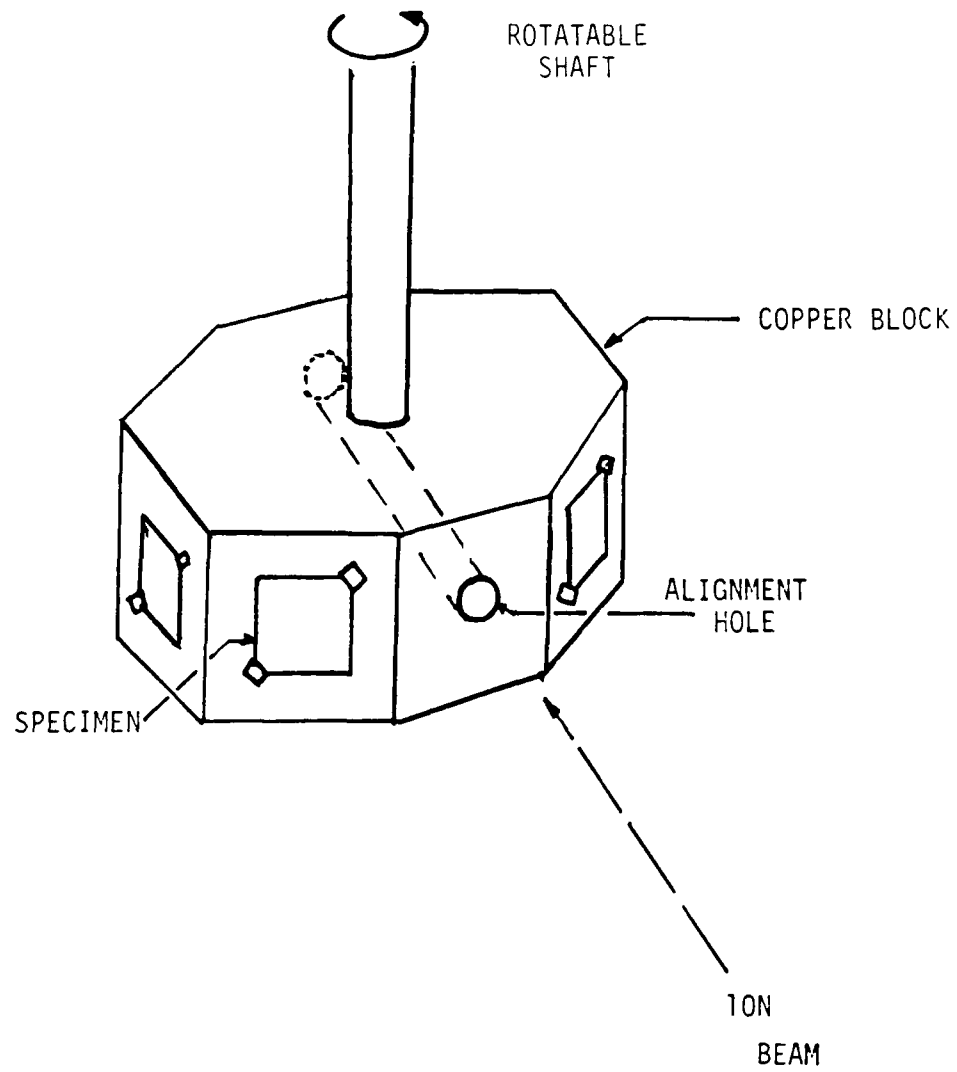


Figure 1. Sample holder configuration.

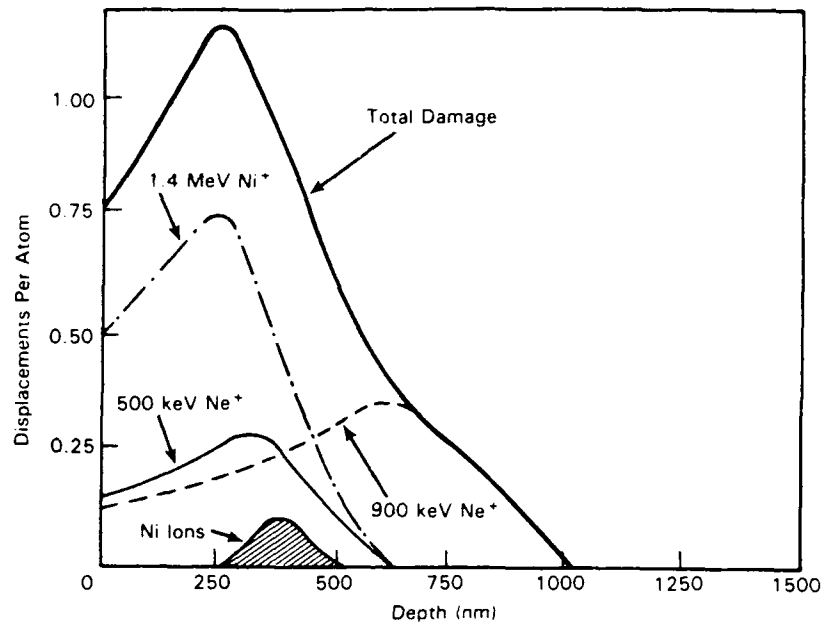


Figure 2. Damage curves for implantation of  $\text{Ne}^+$  and  $\text{Ni}^+$  ions for sample 9/13 A-C.

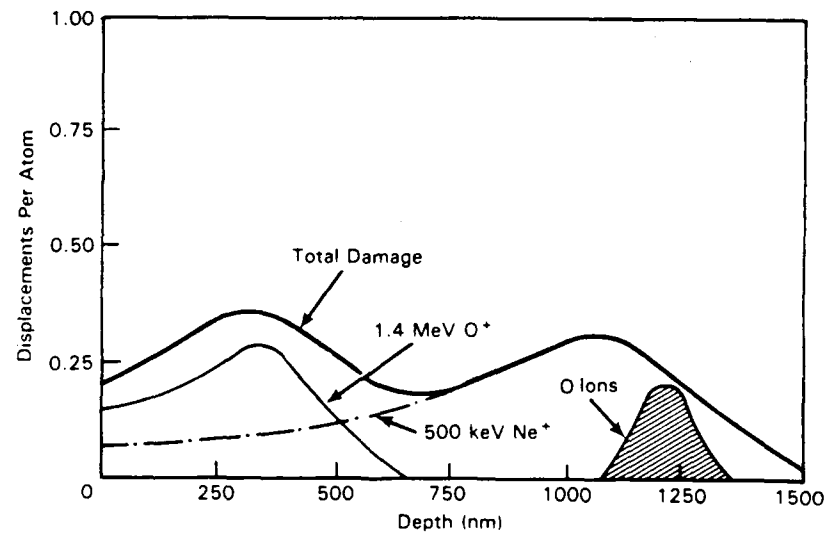


Figure 3. Damage curves for implantation of  $\text{Ne}^+$  and  $\text{O}^+$  ions for samples C-13(4) M5.

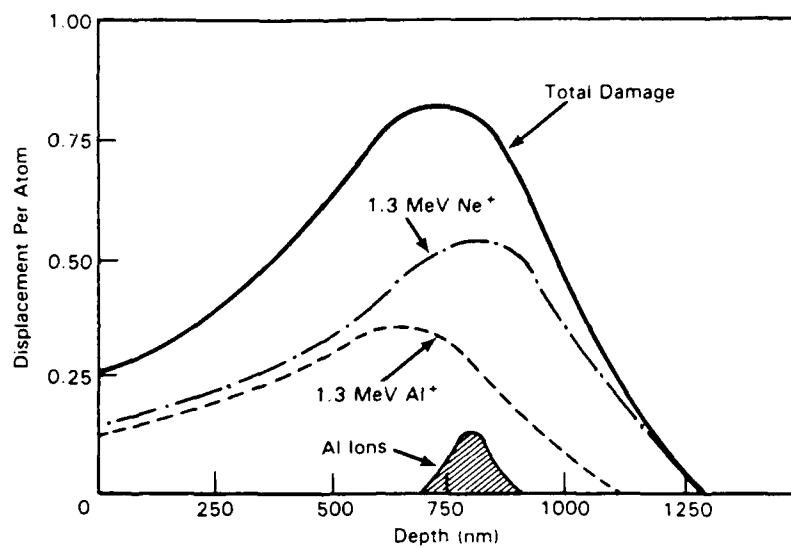


Figure 4. Damage curves for implantation of Ne<sup>+</sup> and Al<sup>+</sup> ions for samples 7/25 A-D, 7/24 A,B.

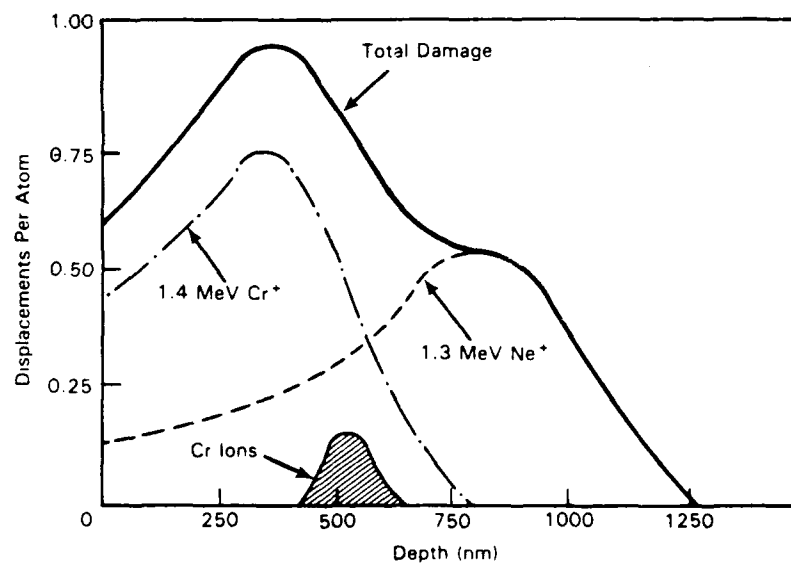


Figure 5. Damage curves for implantation of Ne<sup>+</sup> and Cr<sup>+</sup> ions for samples 7/24 C,D, 7/23 A-D.



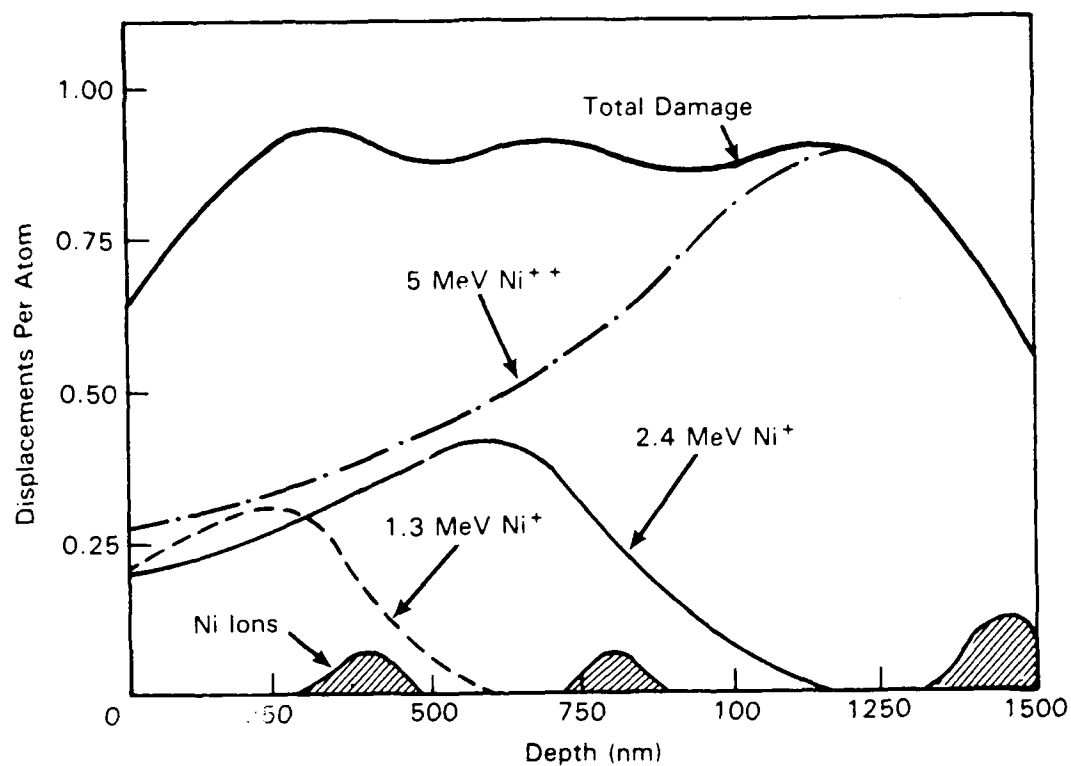
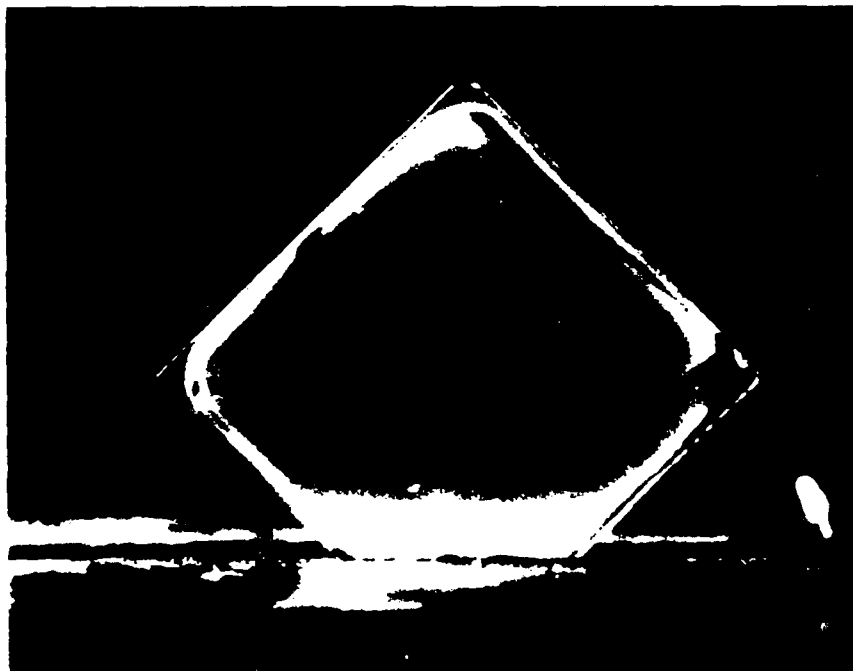


Figure 6. Damage curves for variable energy implant Ni<sup>+</sup> ions for samples 9/13 A-C.



(a) Before modifications--poor uniformity.



(b) After modifications--improved uniformity.

Figure 7. Implantation uniformity sample before and after accelerator modifications.



(a) Very slow raster scan beam.



(b) Stationary beam.

Figure 8. Effects of raster scan speed on uniformity.

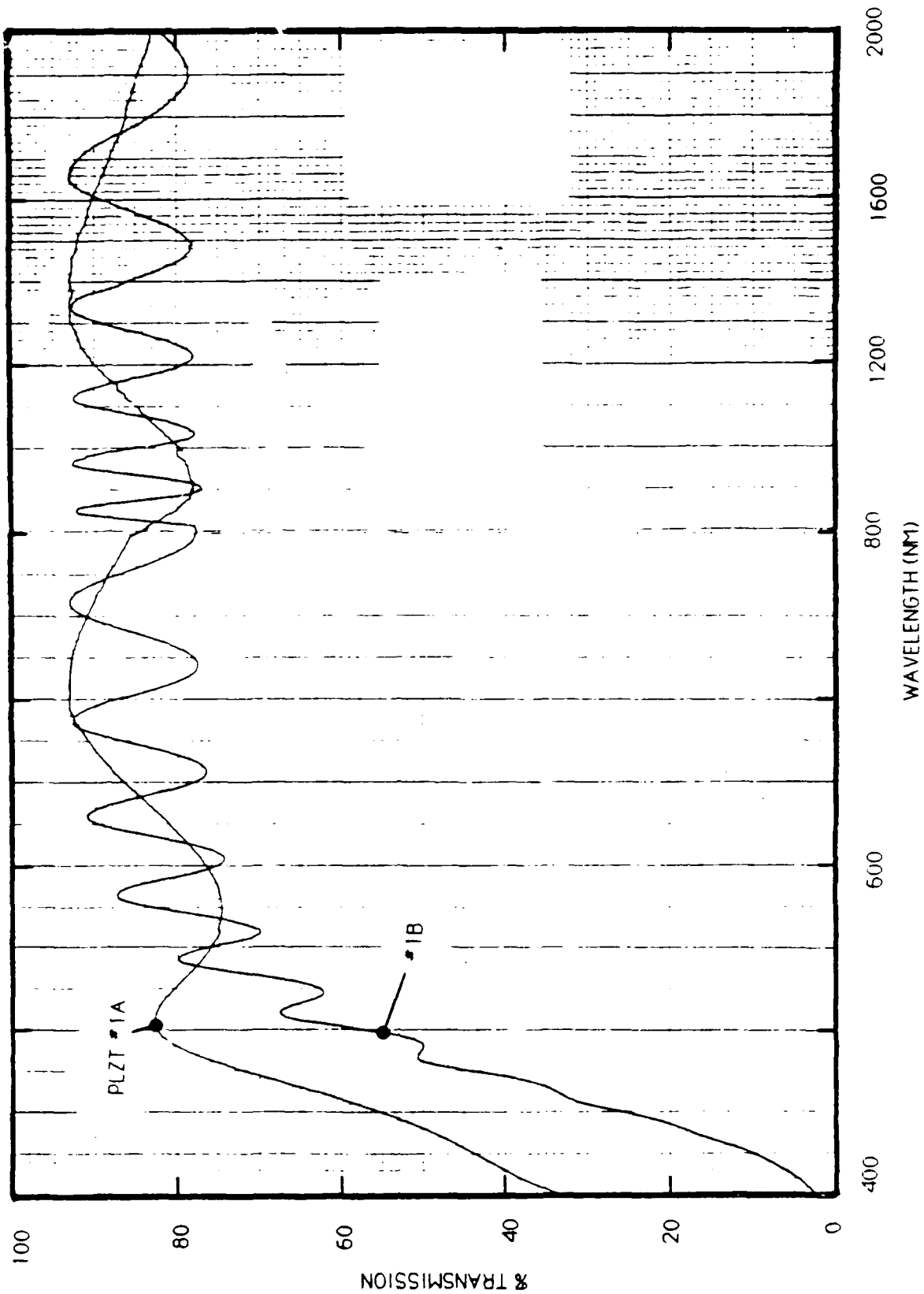


Figure 9. Thin film PLZT transmission.

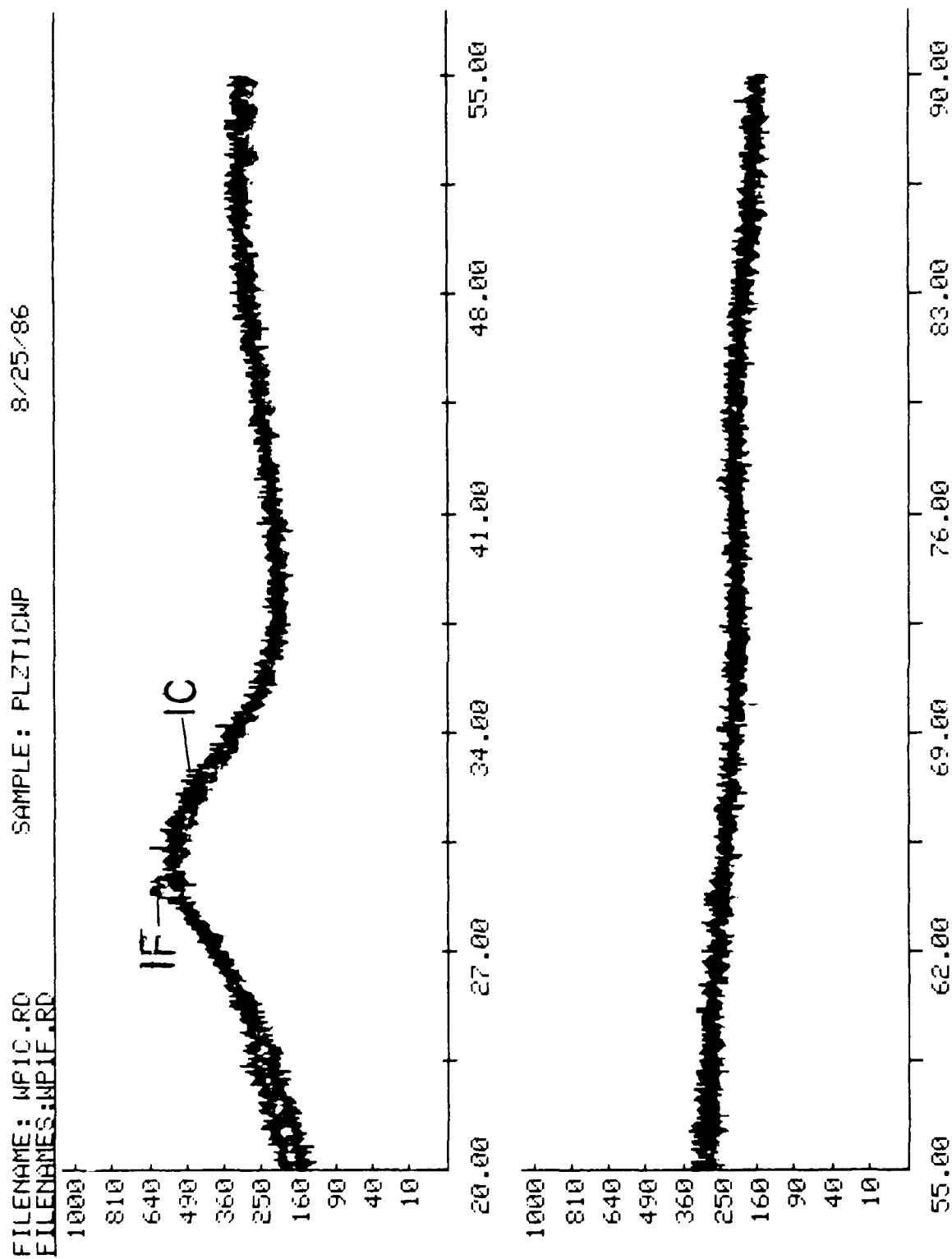


Figure 10. Thin film PLZT X-ray diffraction.

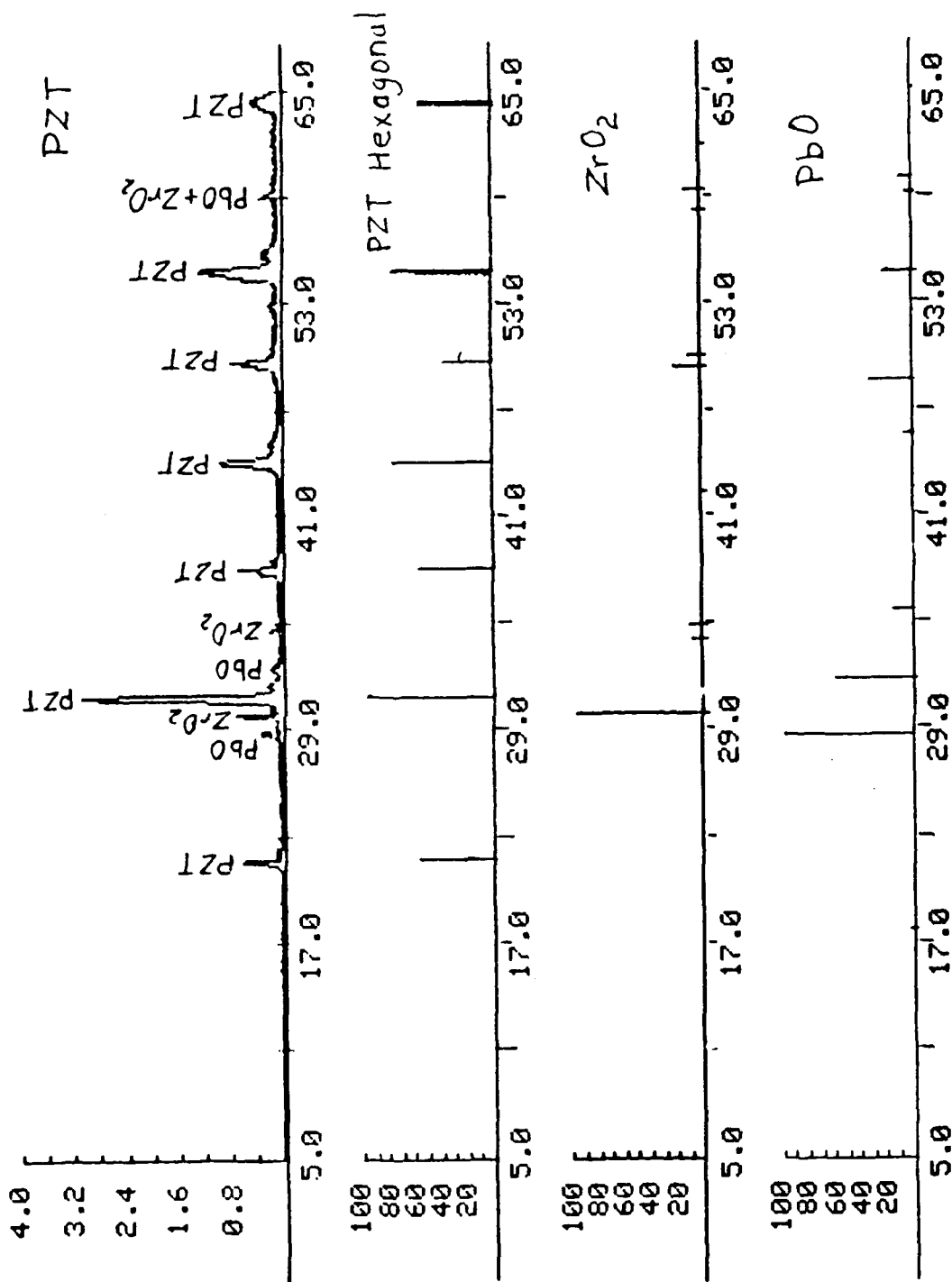


Figure 11. X-ray diffractometer scan of PZT annealed at 1150°C for 1 h. The individual peaks are labeled based on the standard X-ray patterns for the constituent phases as shown below the experimental results.

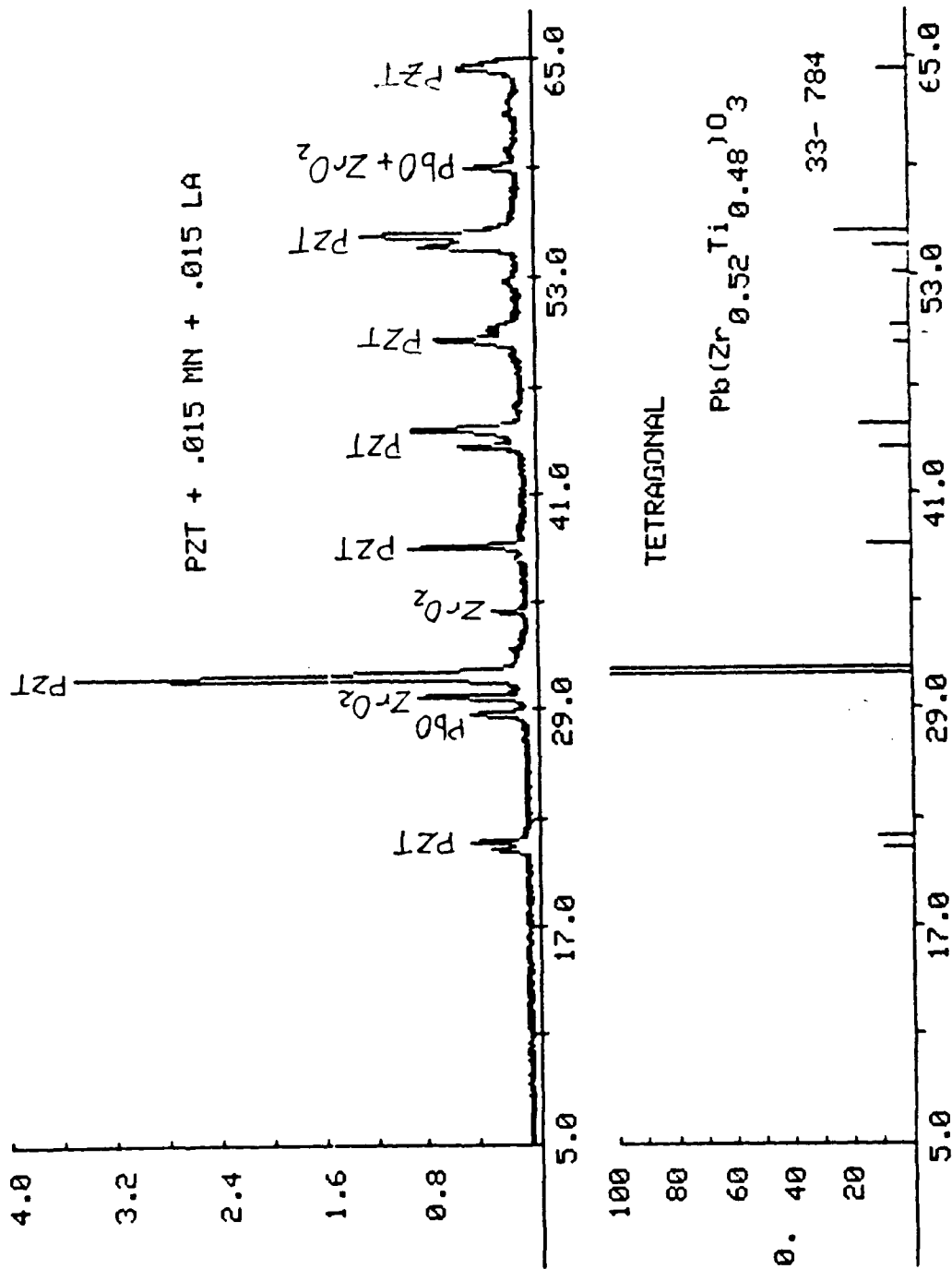
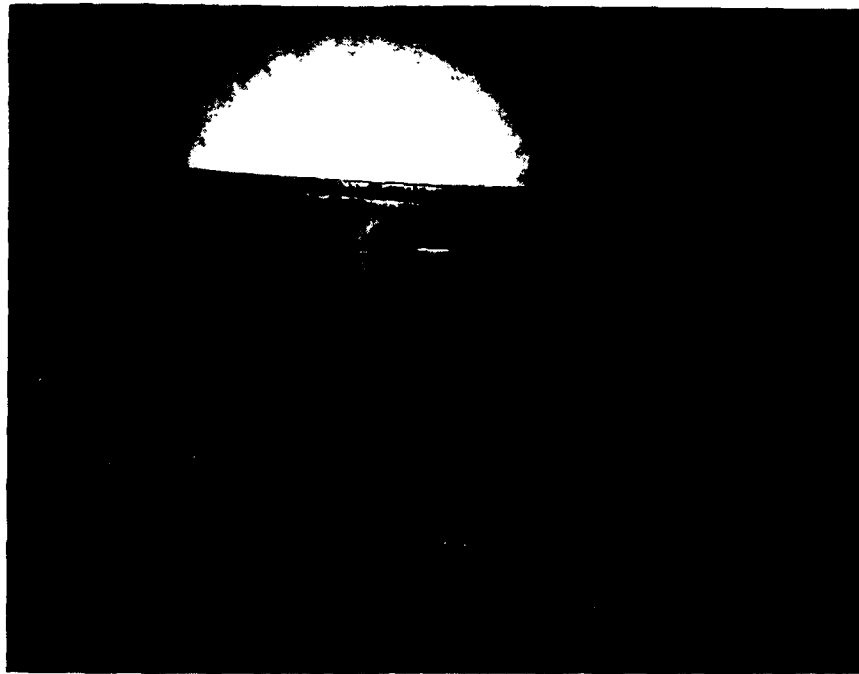
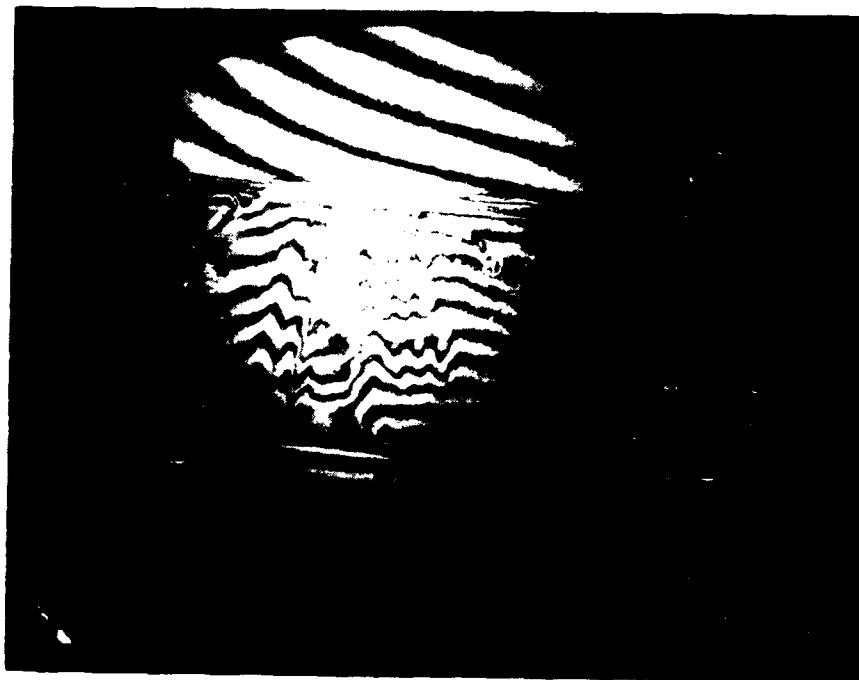


Figure 12. X-ray diffractometer scan of PZT + Mn + La annealed at 1000°C for 1 h. The splitting of the peaks in the PZT is indicative of the tetragonal phase. Note the rather strong peaks of the ZrO phase.



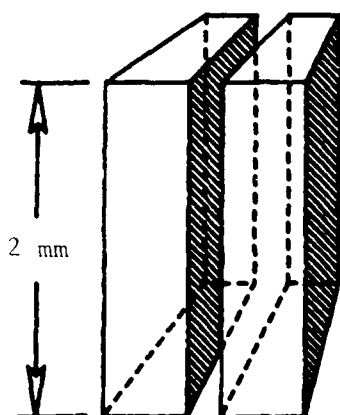
(a) Sample photographed in transmission.



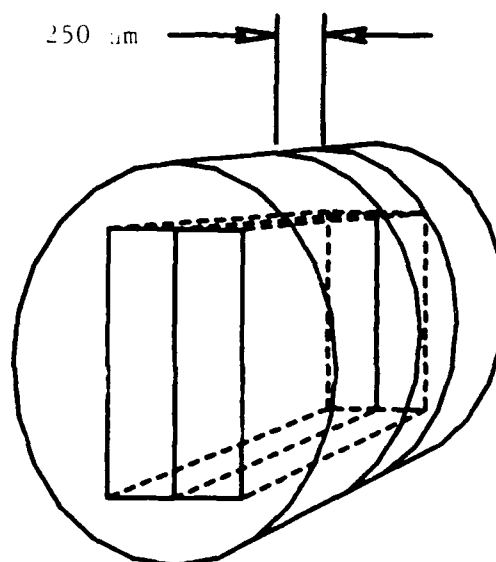
(b) Interferogram.

Figure 13. Surface deformation examined using interferometer.

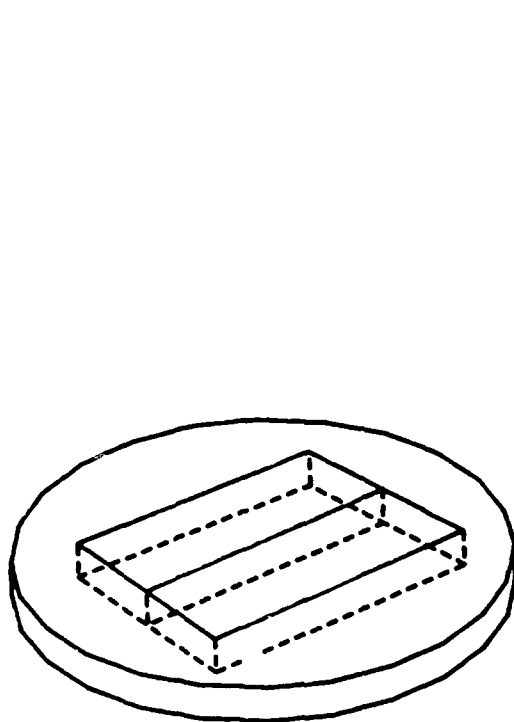




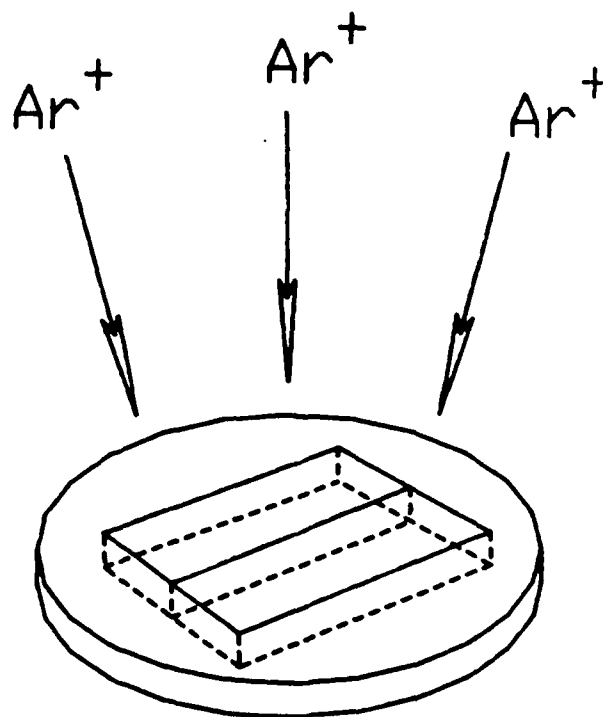
(a) Bonding irradiated PLZT slabs.



(b) Bonded slabs sealed in an epoxy-filled tube.



(c) Disk cut from the tube.



(d) Polished and thinned disk.

Figure 14. Steps in preparation of cross-section specimens for TEM.

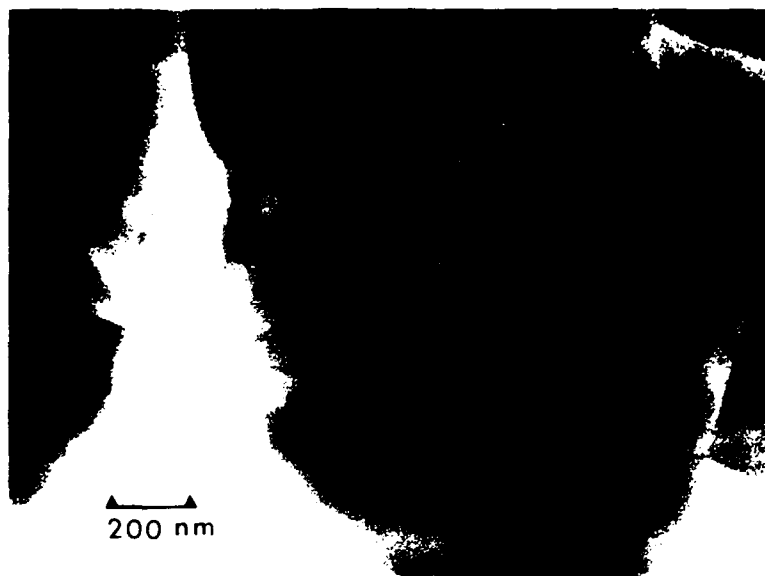


Figure 15. TEM micrograph of PLZT showing featureless, defect-free grain structure. Arrow points to grain boundary junction.

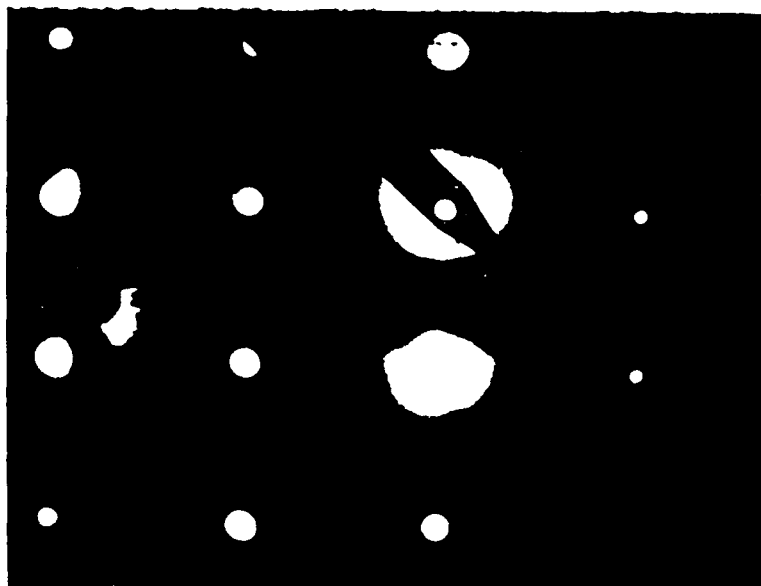


Figure 16. Selected area electron diffraction pattern from structure shown in Fig. 15. Spot pattern is caused by crystalline perovskite.

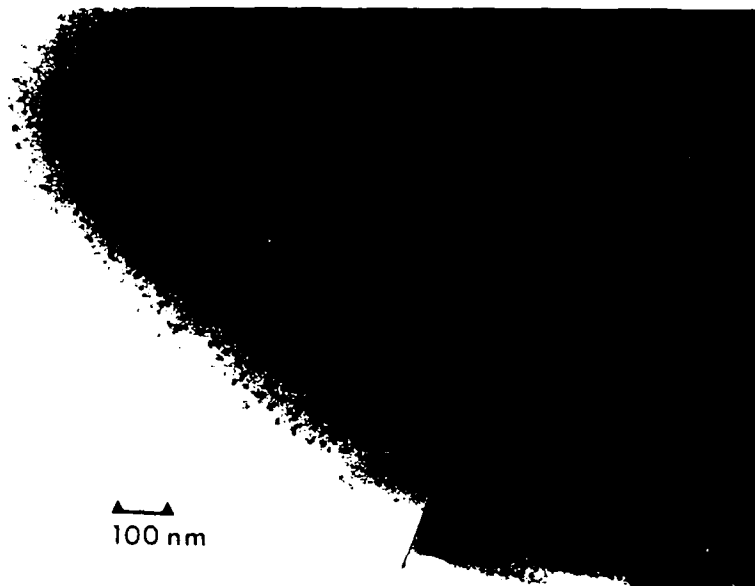


Figure 17. TEM micrograph of PLZT. Dark regions indicating structural transformation are beginning to occur.

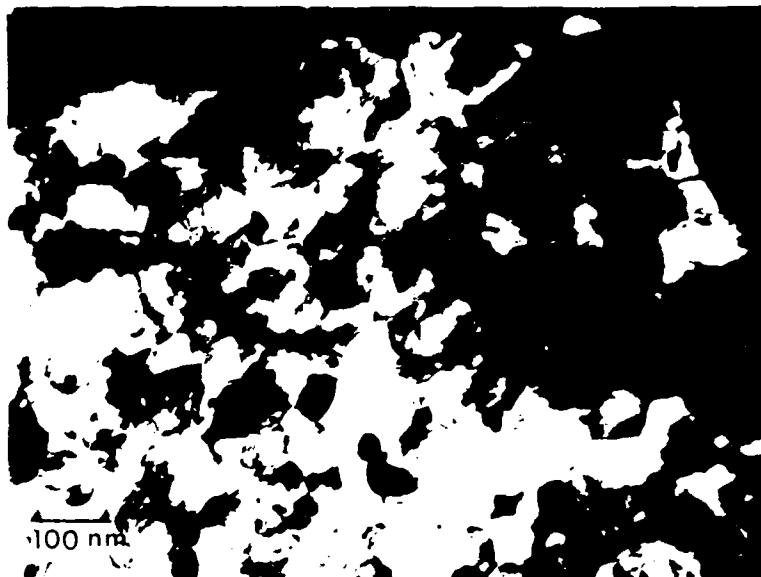


Figure 18. TEM micrograph of PLZT showing very fine microcrystalline region. Complete transformation of the structure has occurred in this region.

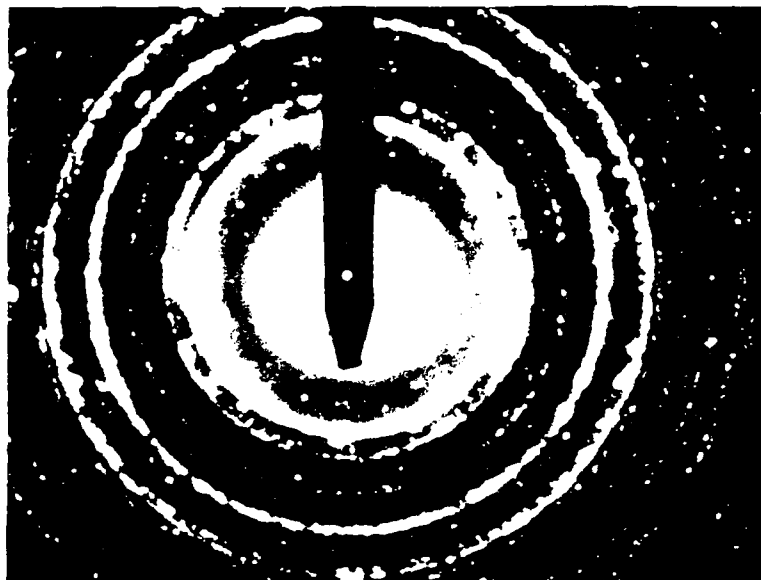


Figure 19. Selected area electron diffraction pattern from the structure shown in Fig. 18. Spotty ring pattern can be indexed as the tetragonal  $(\text{Zr, Ti})\text{O}_2$  structure. Diffuse rings are caused by amorphous layers at the surface of the structure.

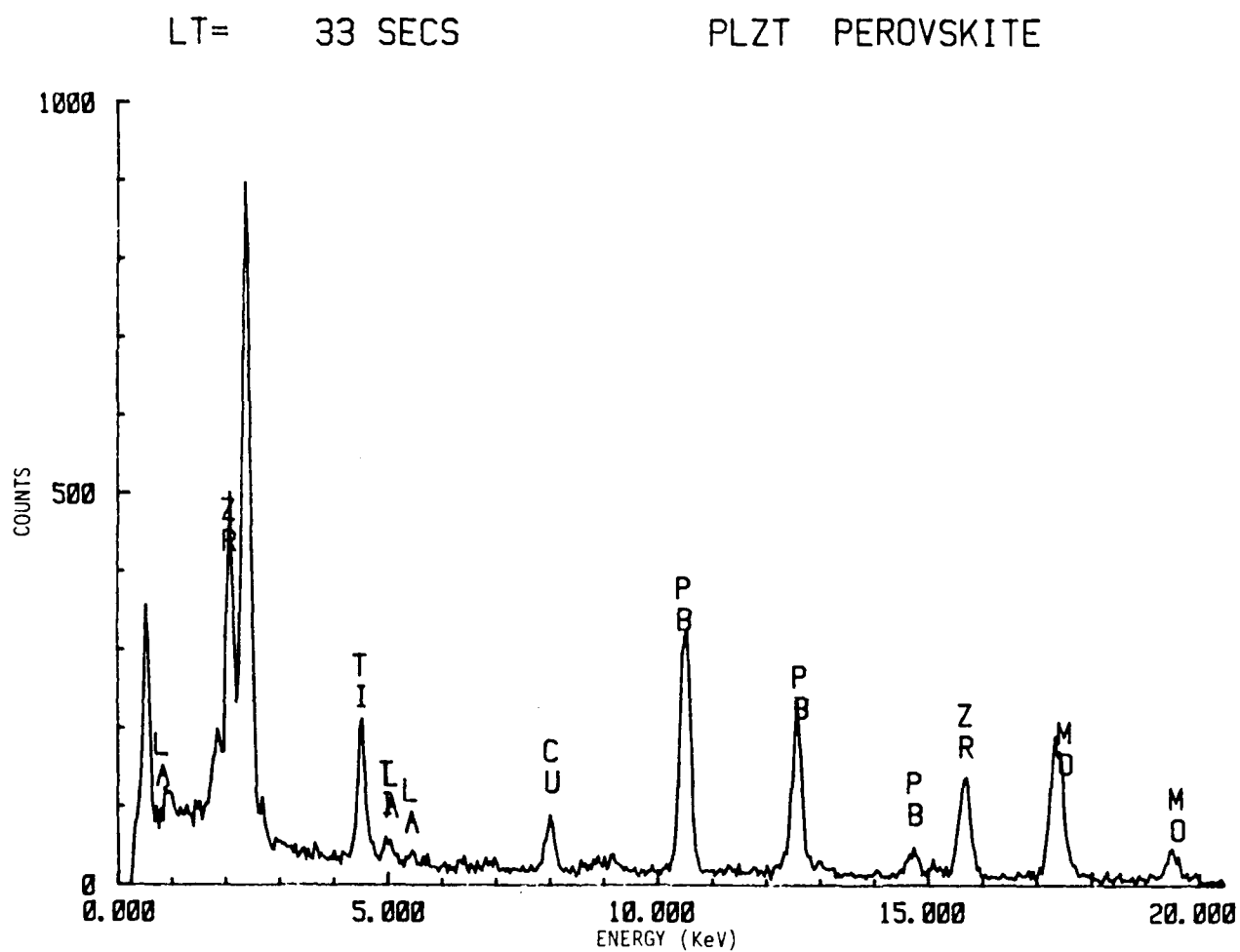


Figure 20. EDX elemental spectrum from perovskite region of the sample shown in Fig. 15.

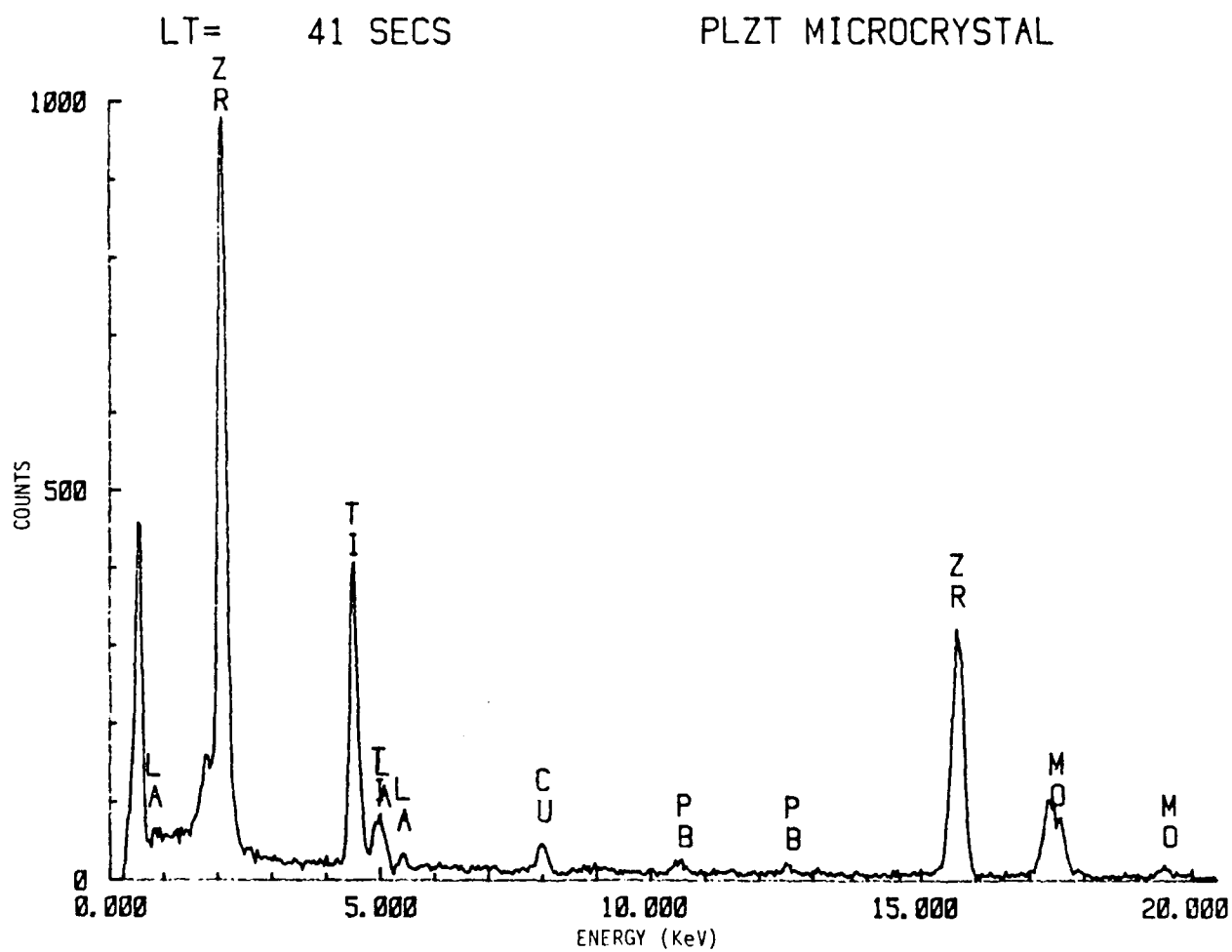


Figure 21. EDX elemental spectrum from microcrystalline,  $(\text{Zr,Ti})\text{O}_2$  phase as shown in Fig. 18.

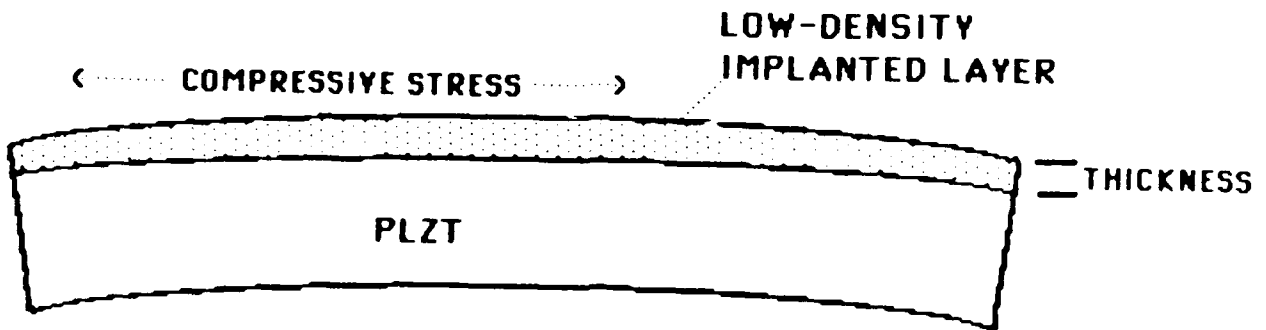


Figure 22. PLZT wafer after implant.

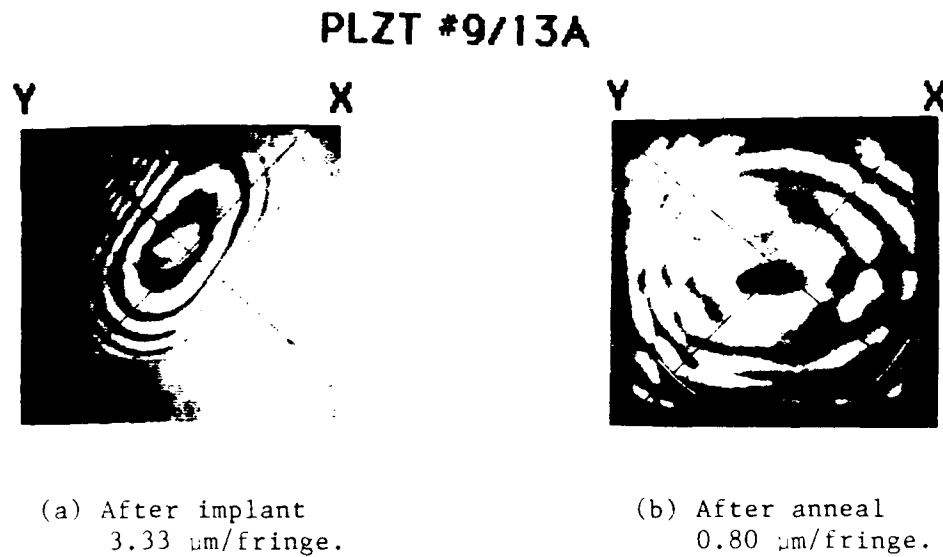


Figure 23. Interferogram showing the effect of 200°C, 10-h, air anneal on reducing curvature after implantation.

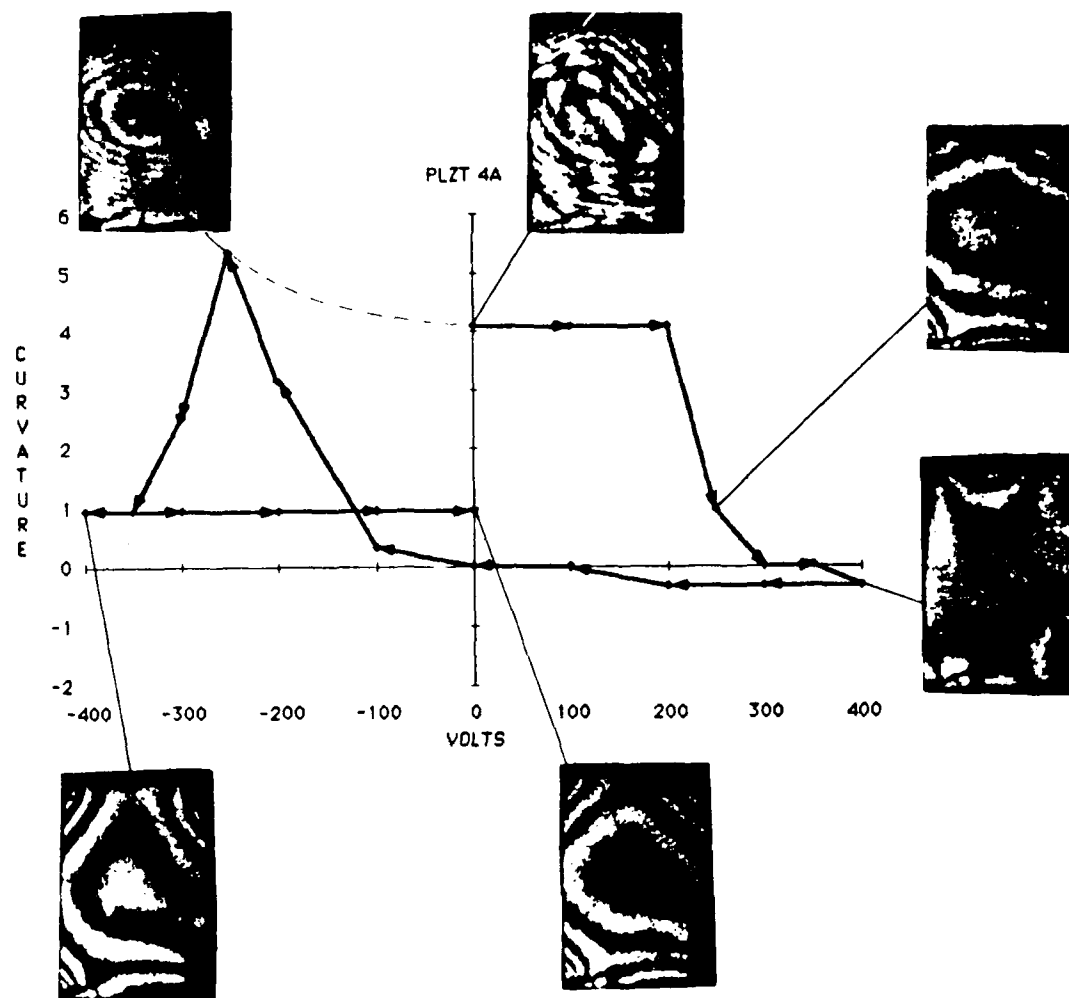


Figure 24. Implanted sample curvature hysteresis.



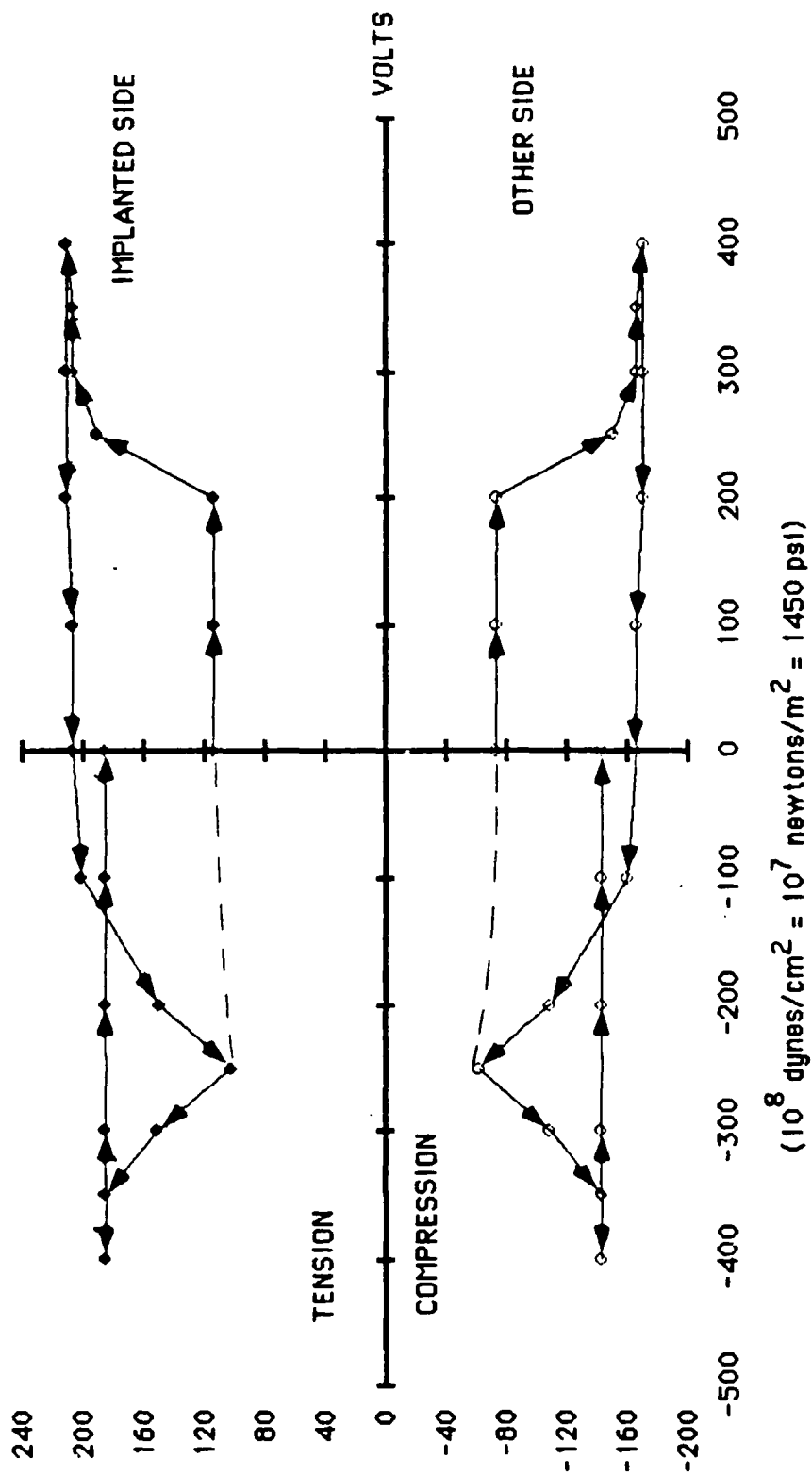


Figure 25. ITO stress ( $10^8 \text{ dynes/cm}^2$ ).

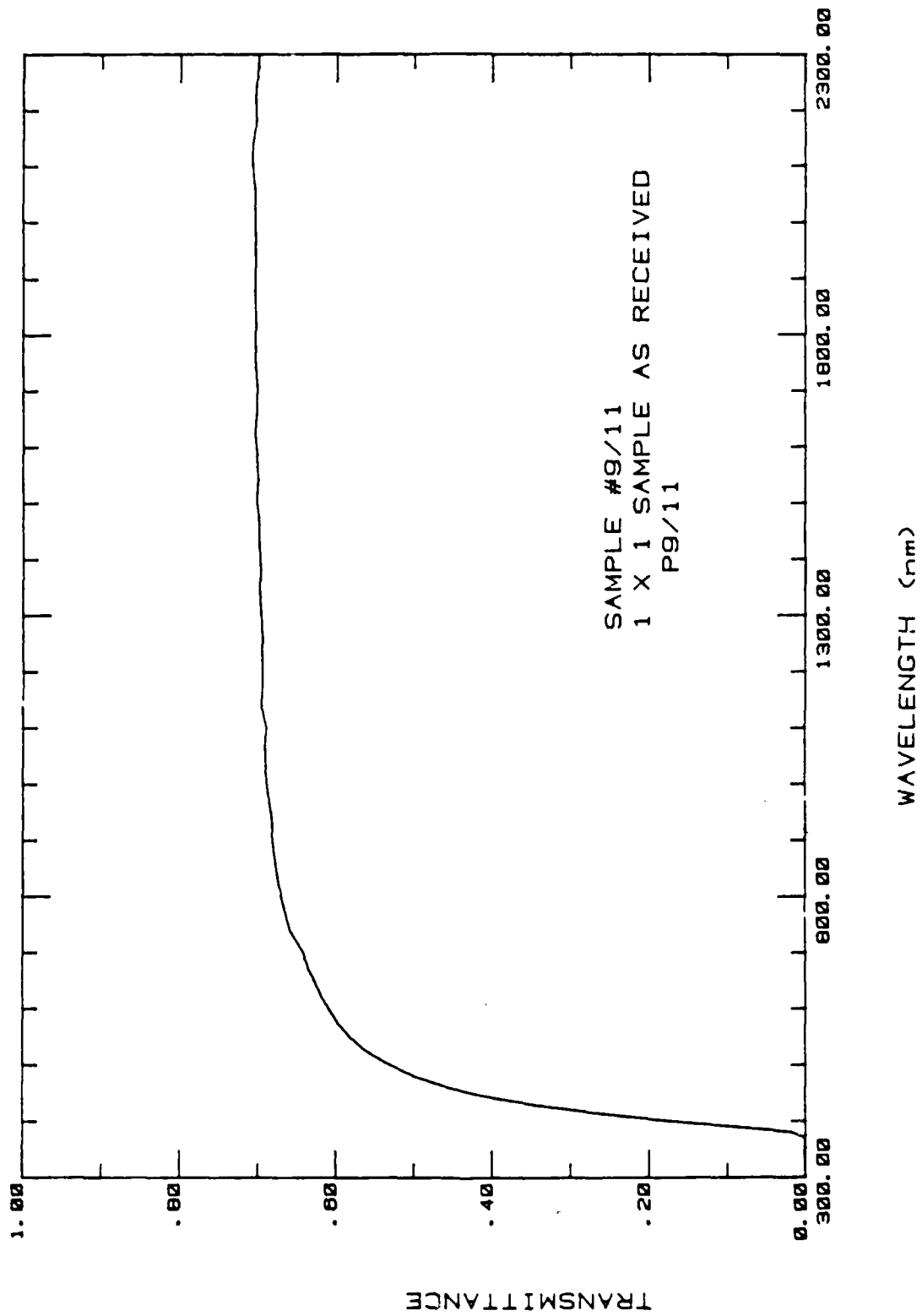


Figure 26. Transmission of as-received water.

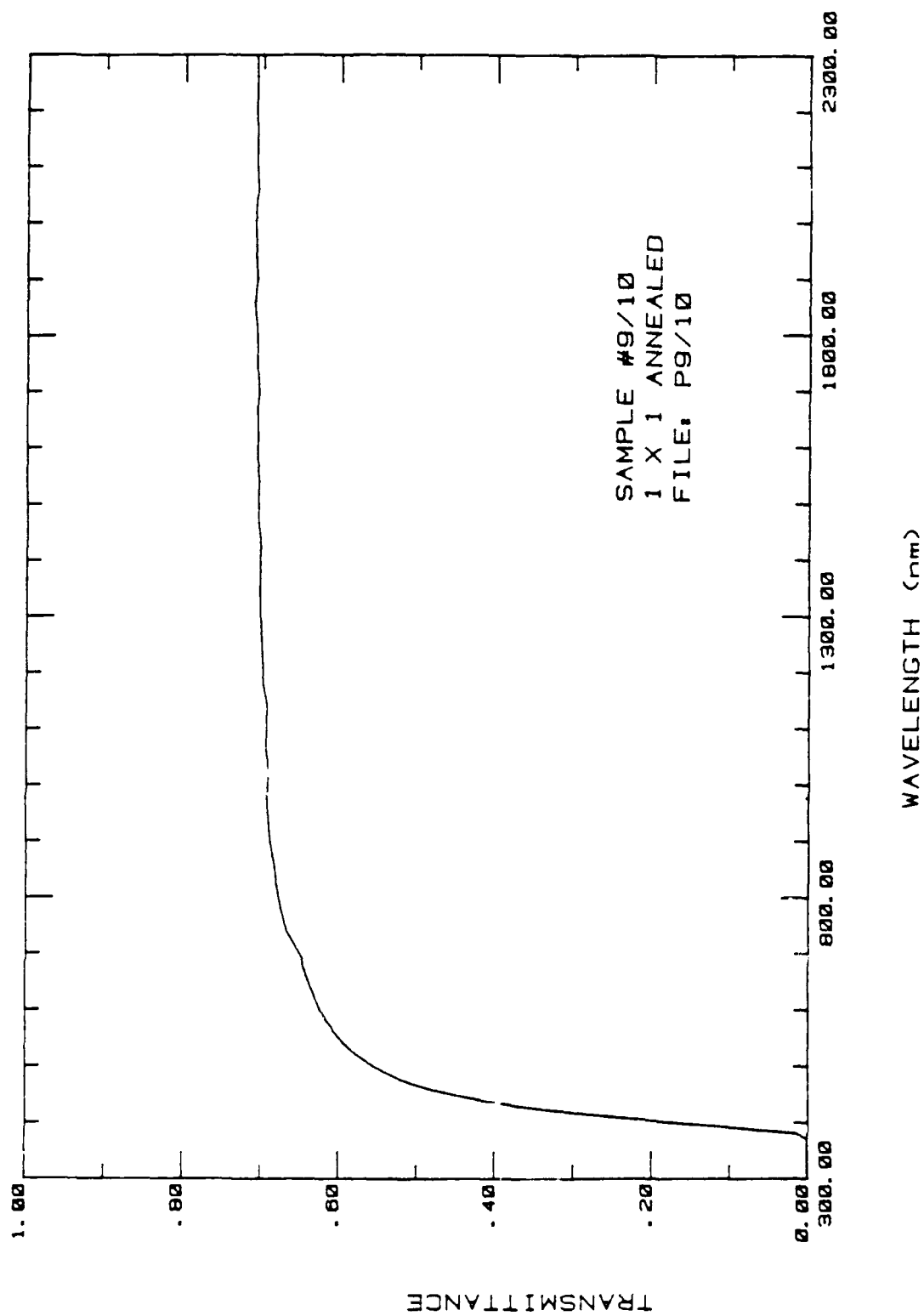


Figure 27. Transmission of annealed water.

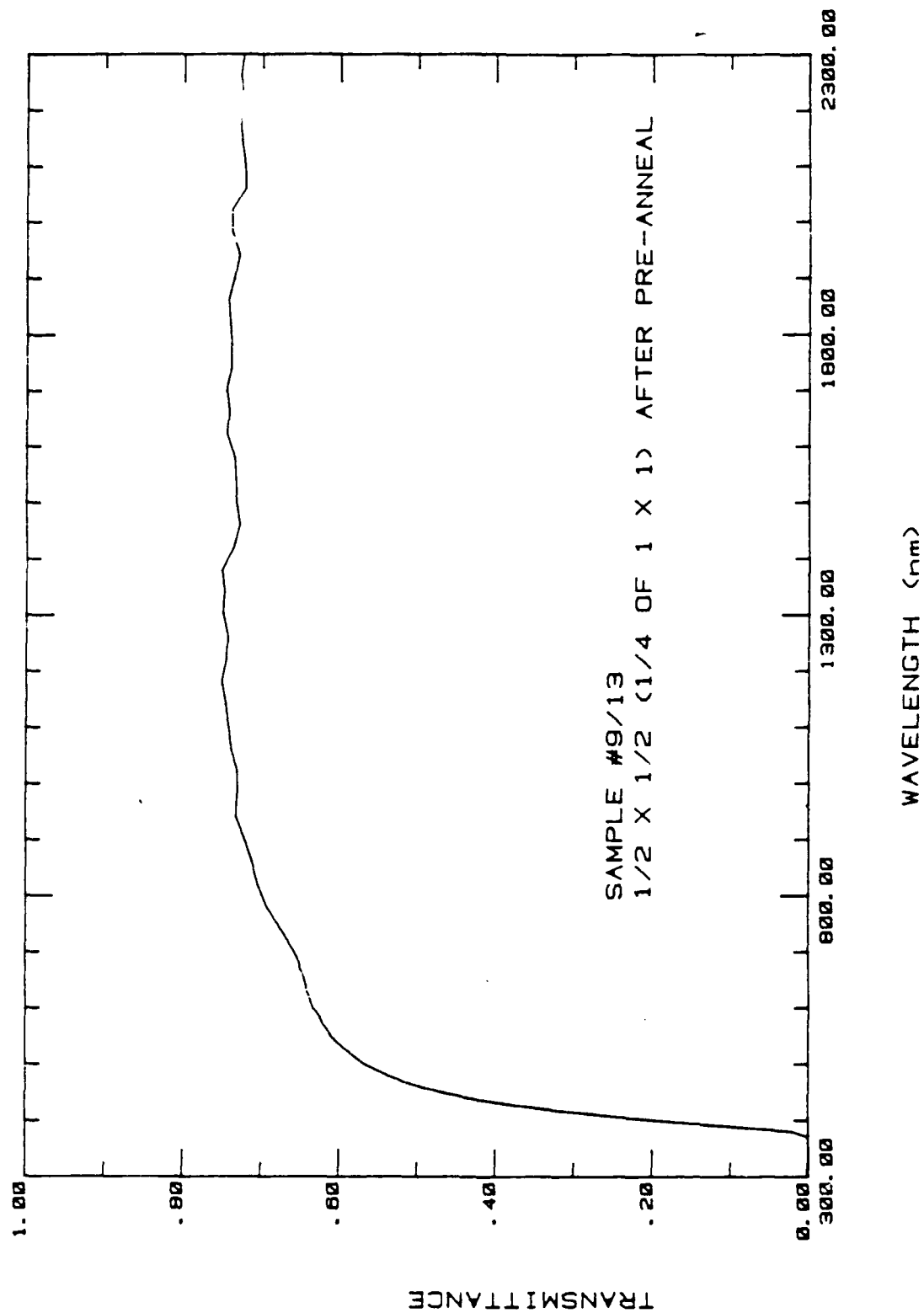


Figure 28. Transmission of cut and annealed wafer.

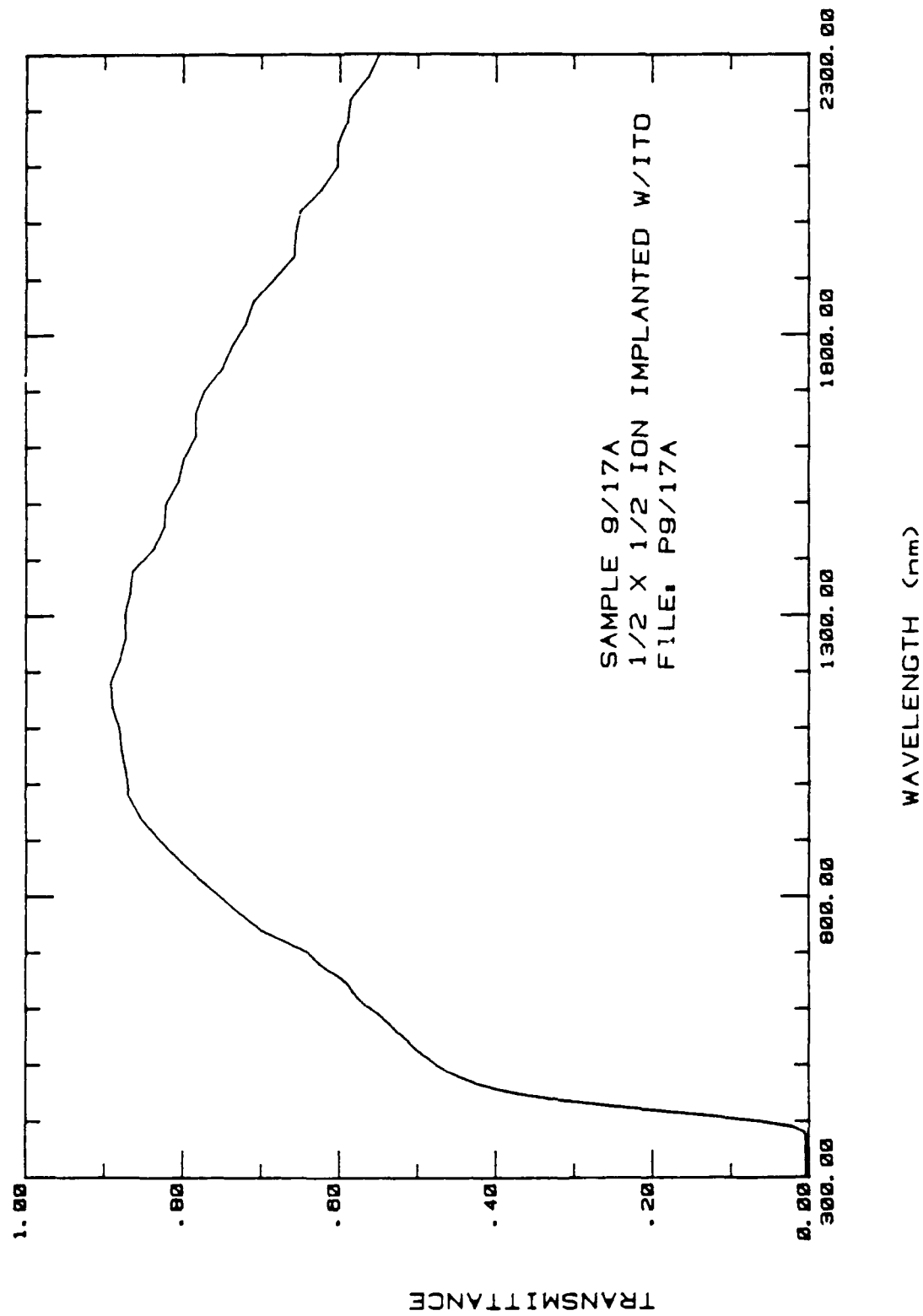


Figure 29. Transmission of implanted and ITO-coated wafer.

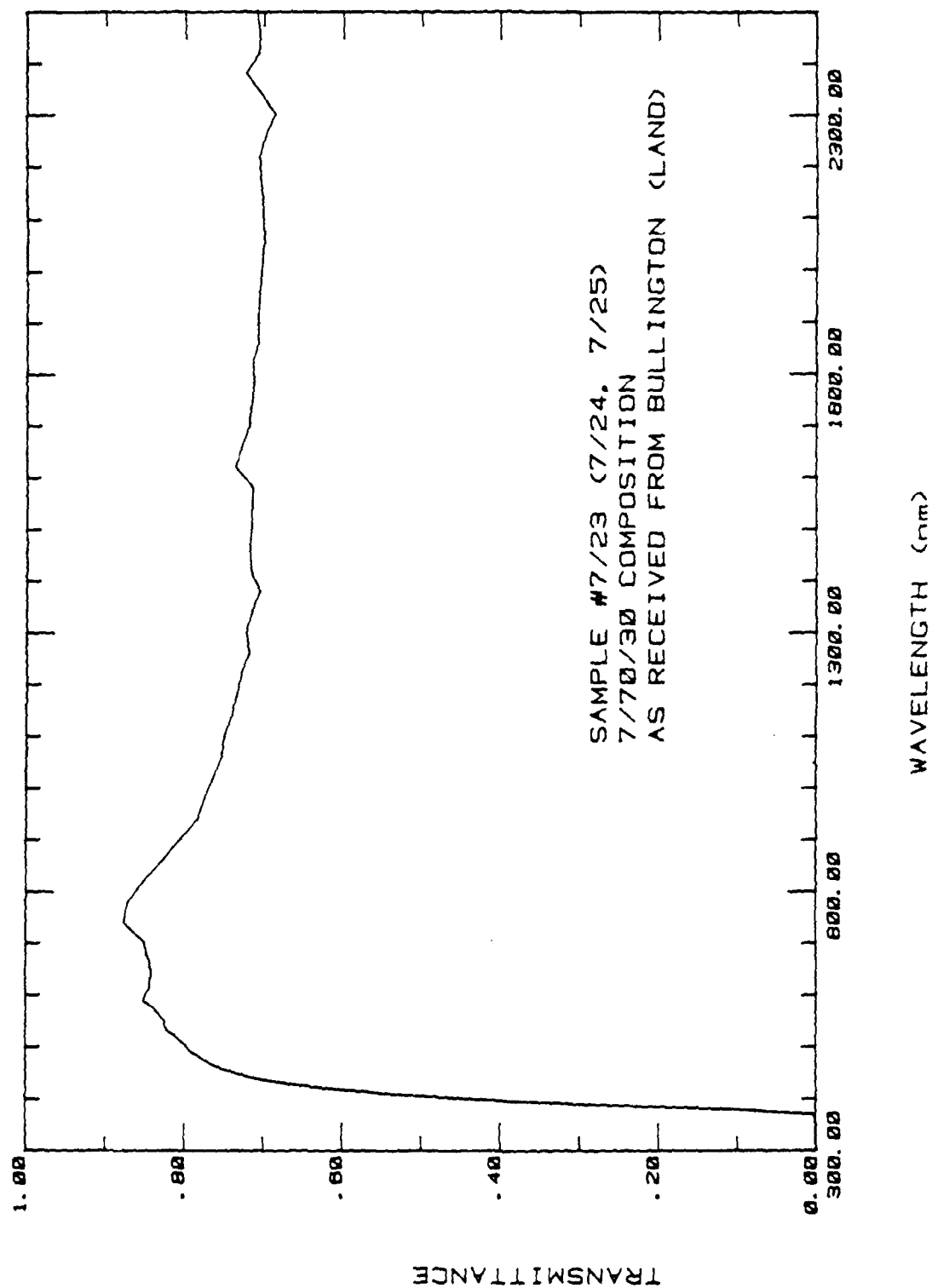


Figure 30. Transmission of as-received 7/70/30 water.

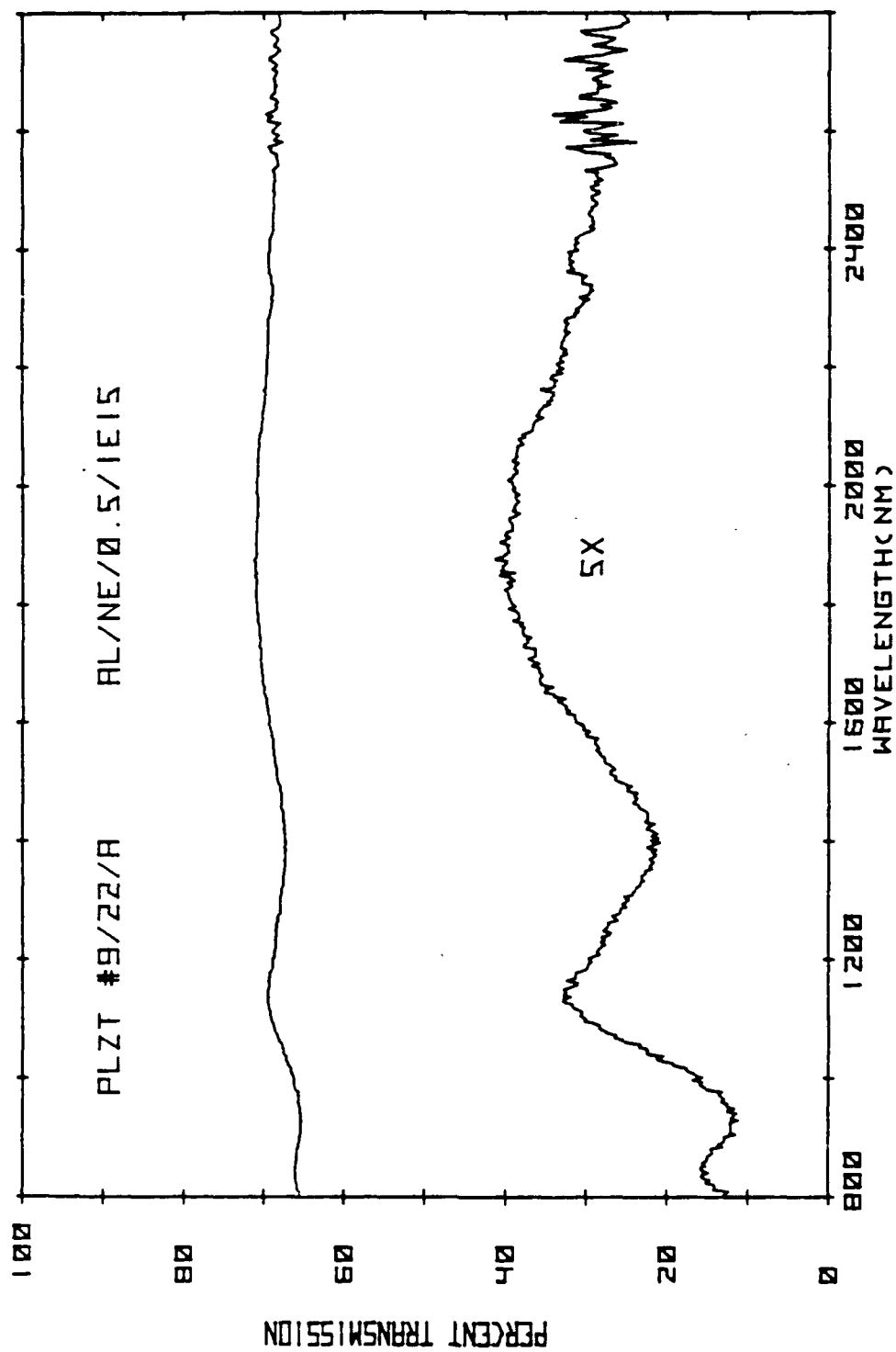


Figure 31. Oscillations in IR-transmission of implanted PLZT.

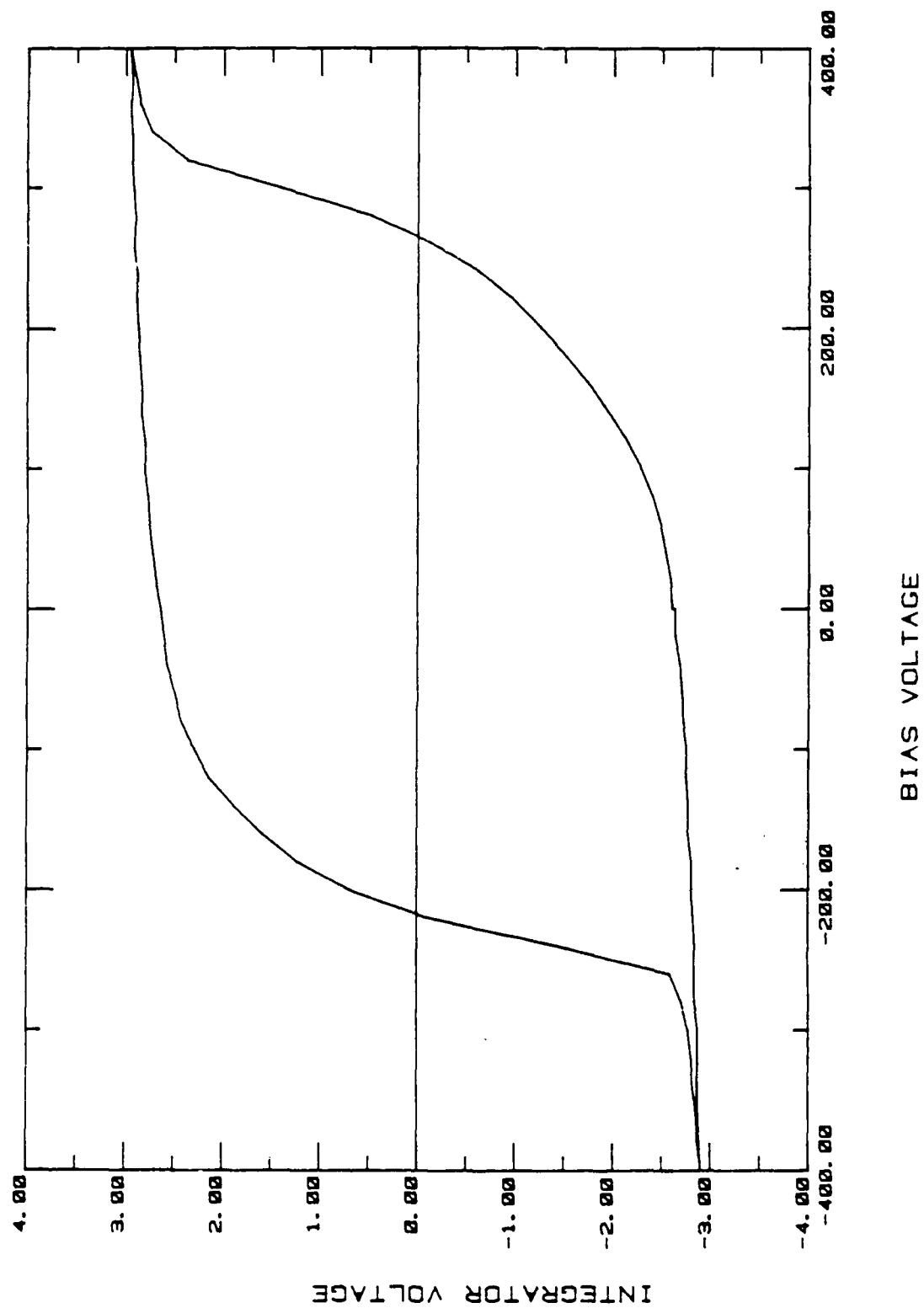
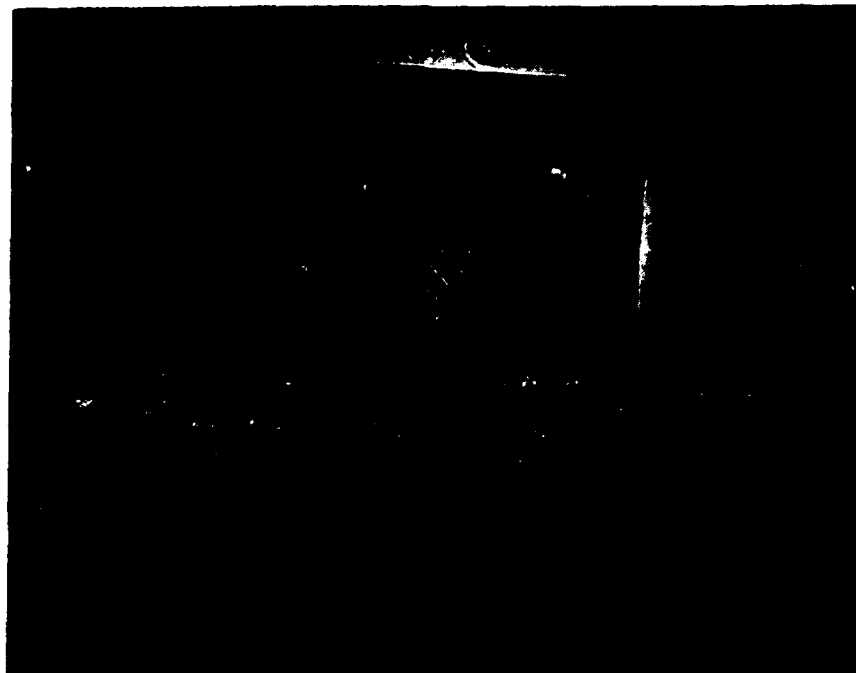
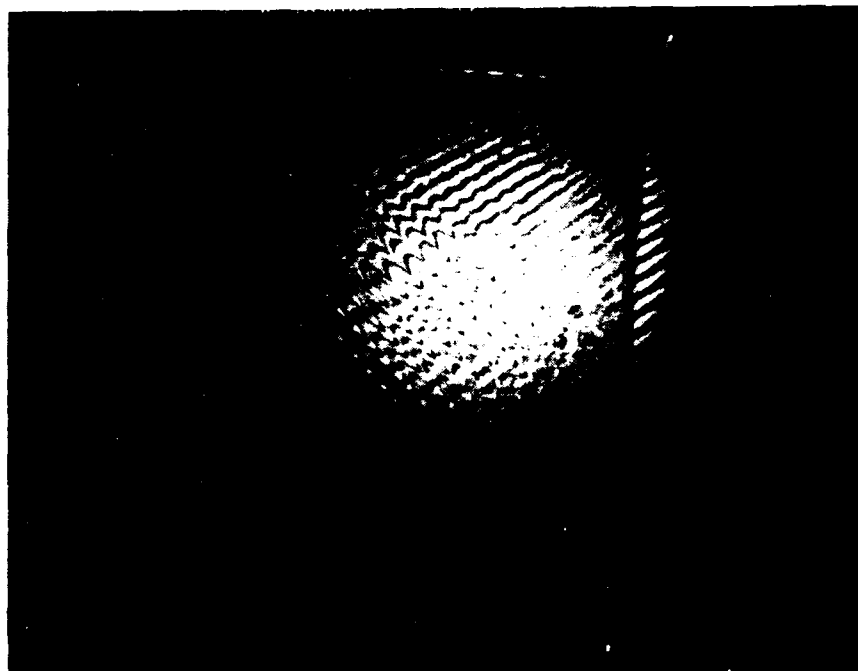


Figure 32.  $O^{2+}$  implanted sample B-8, first characteristic curve.





(a) Fifty-line-per-inch Ronchi ruling printed on sample B-8.



(b) Interferogram of sample shown in (a).

Figure 33. Photosensitivity test of 7/65/35 PLZT implanted with  $O^+$  ions.



Figure 34. Diffraction of 3 mW HeNe beam by 300-line-per-inch Ronchi ruling printed on sample 9/18B.

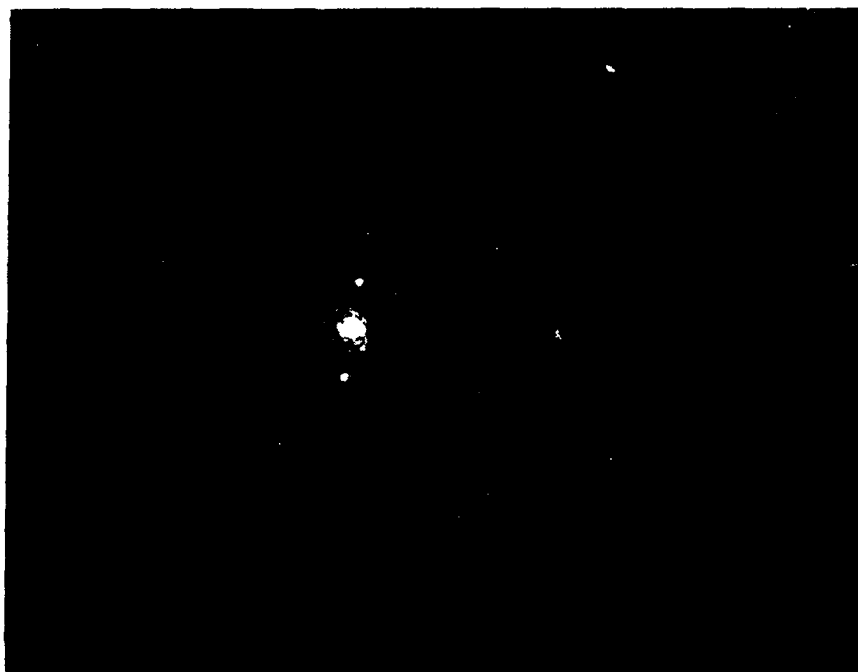


Figure 35. Diffraction of 25 mW HeNe beam by 300-line-per-inch Ronchi ruling printed on sample 9/18B.

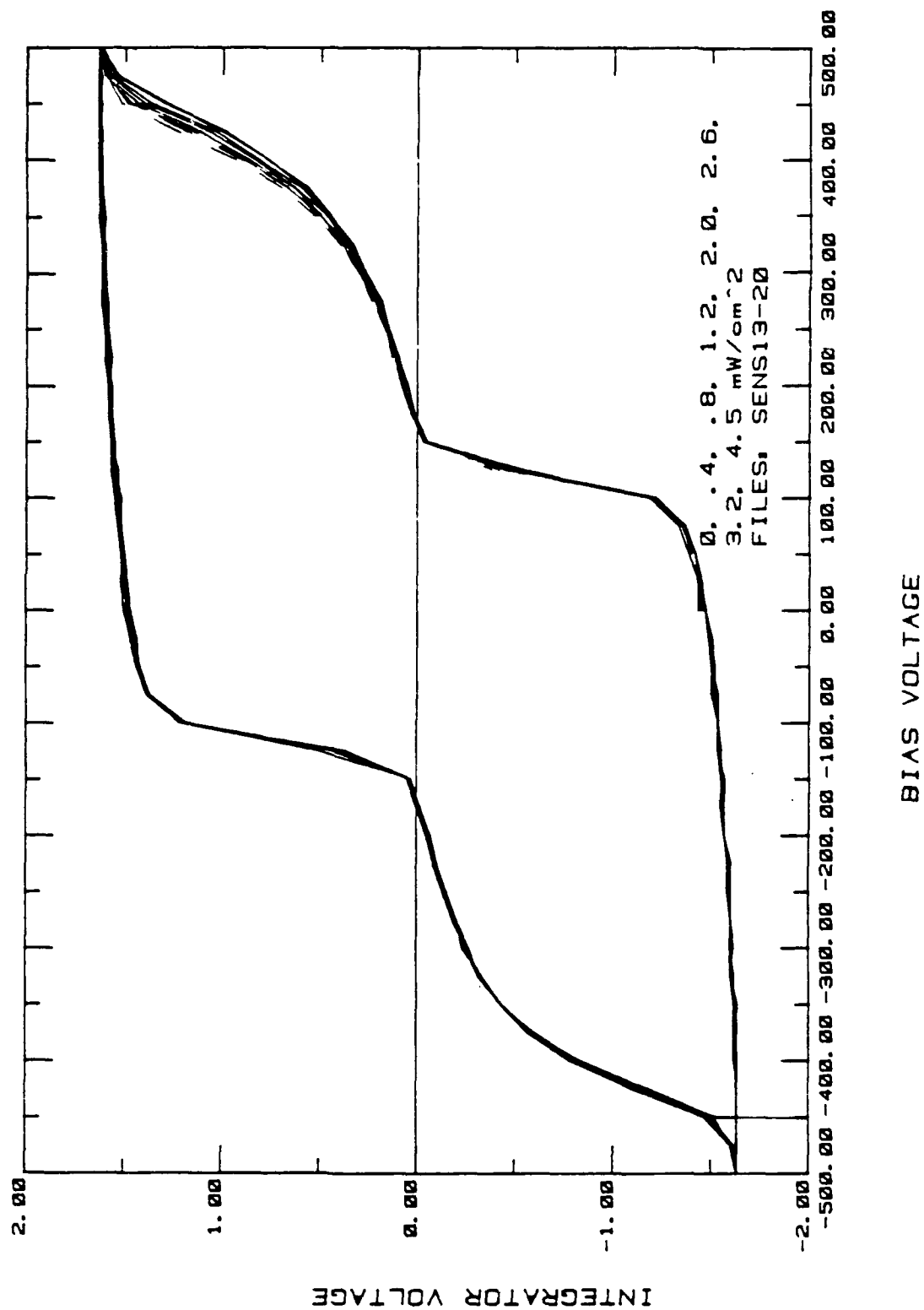


Figure 36. Sample 9/17C,  $O^+$  +  $Ni^+$ ; sensitivity run. No light to 4.5 MW at 4/6.2 nm.

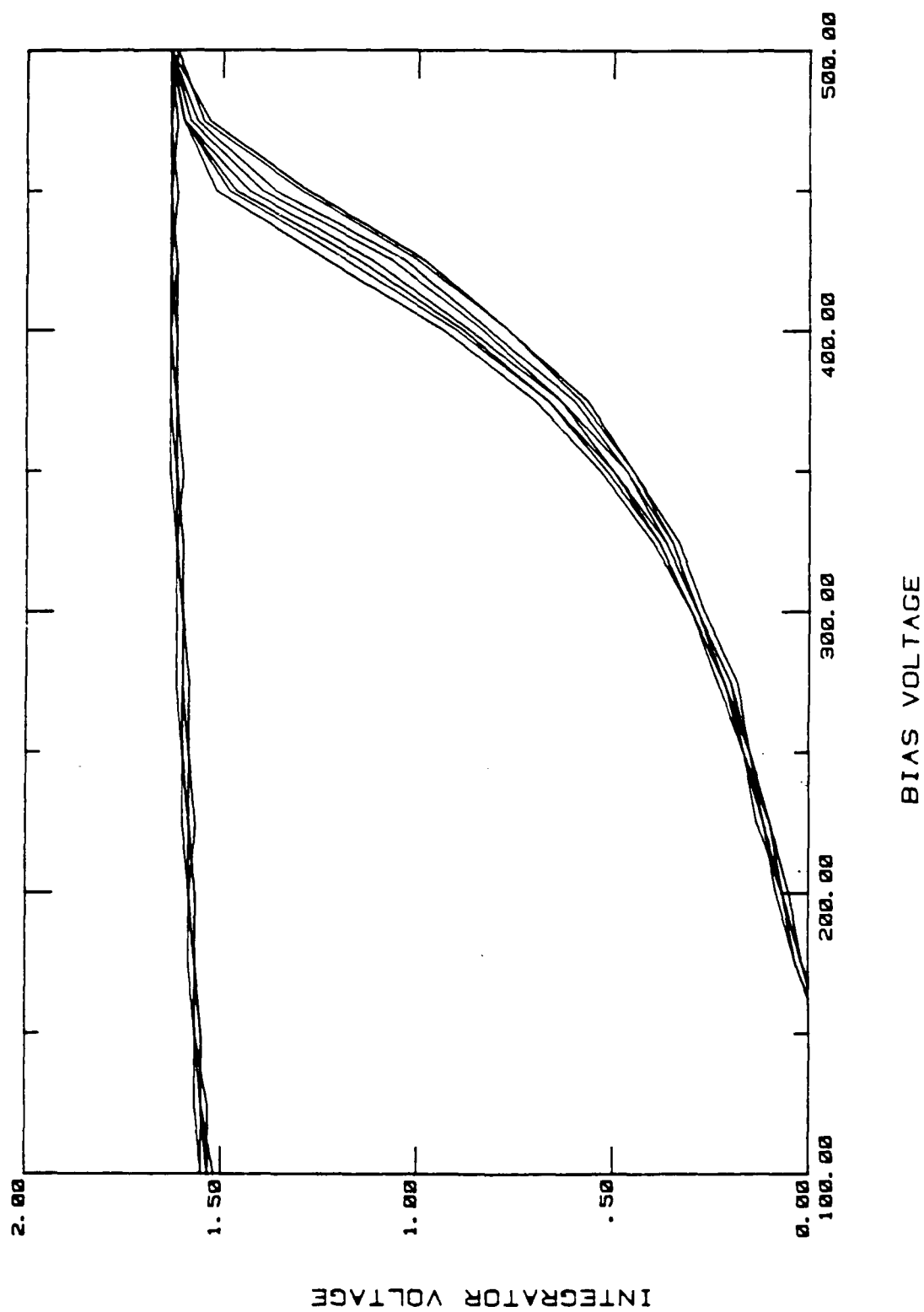


Figure 37. Sample 9/17C;  $O^+$  +  $Ni^+$ ; sensitivity run, expanded. No light to 4.5 MW at 476.2 nm.

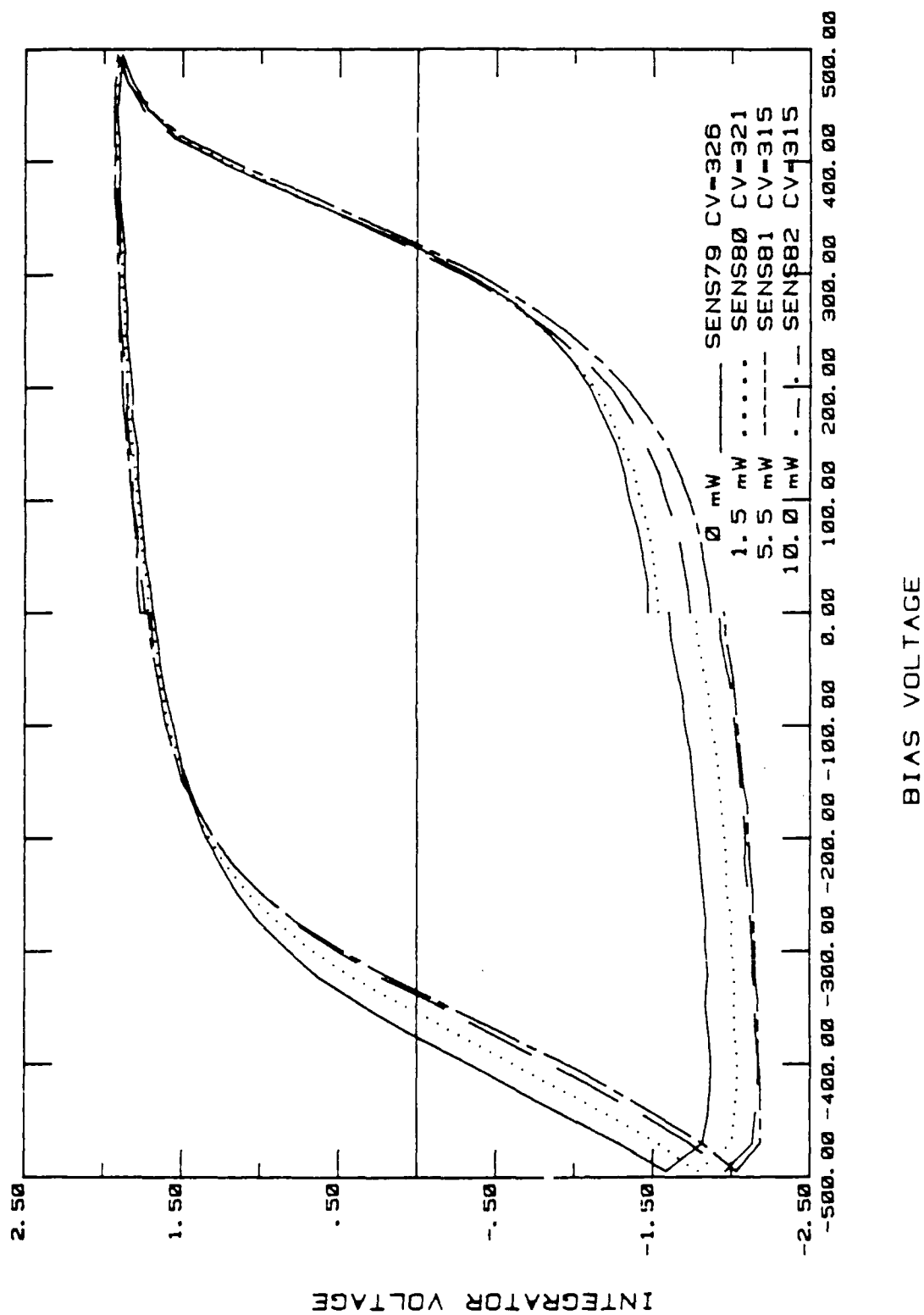


Figure 38. Sensitivity run, sample 9/13C; 1.5, 5.5, and 10 MW at 476.2 nm.

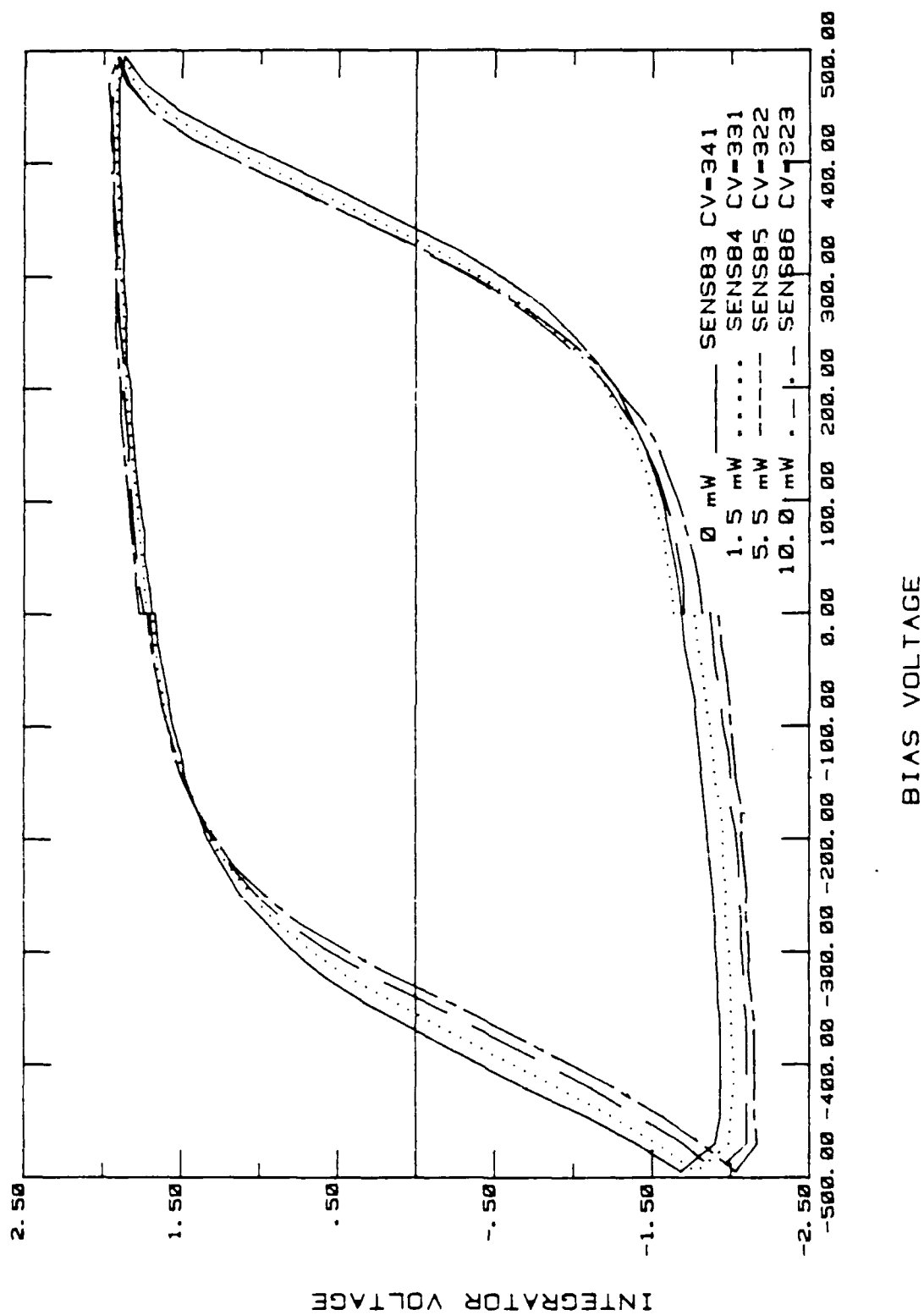


Figure 39. Sensitivity run, sample 9/13C; 1.5, 5.5, and 10 mW at 482.5 nm.

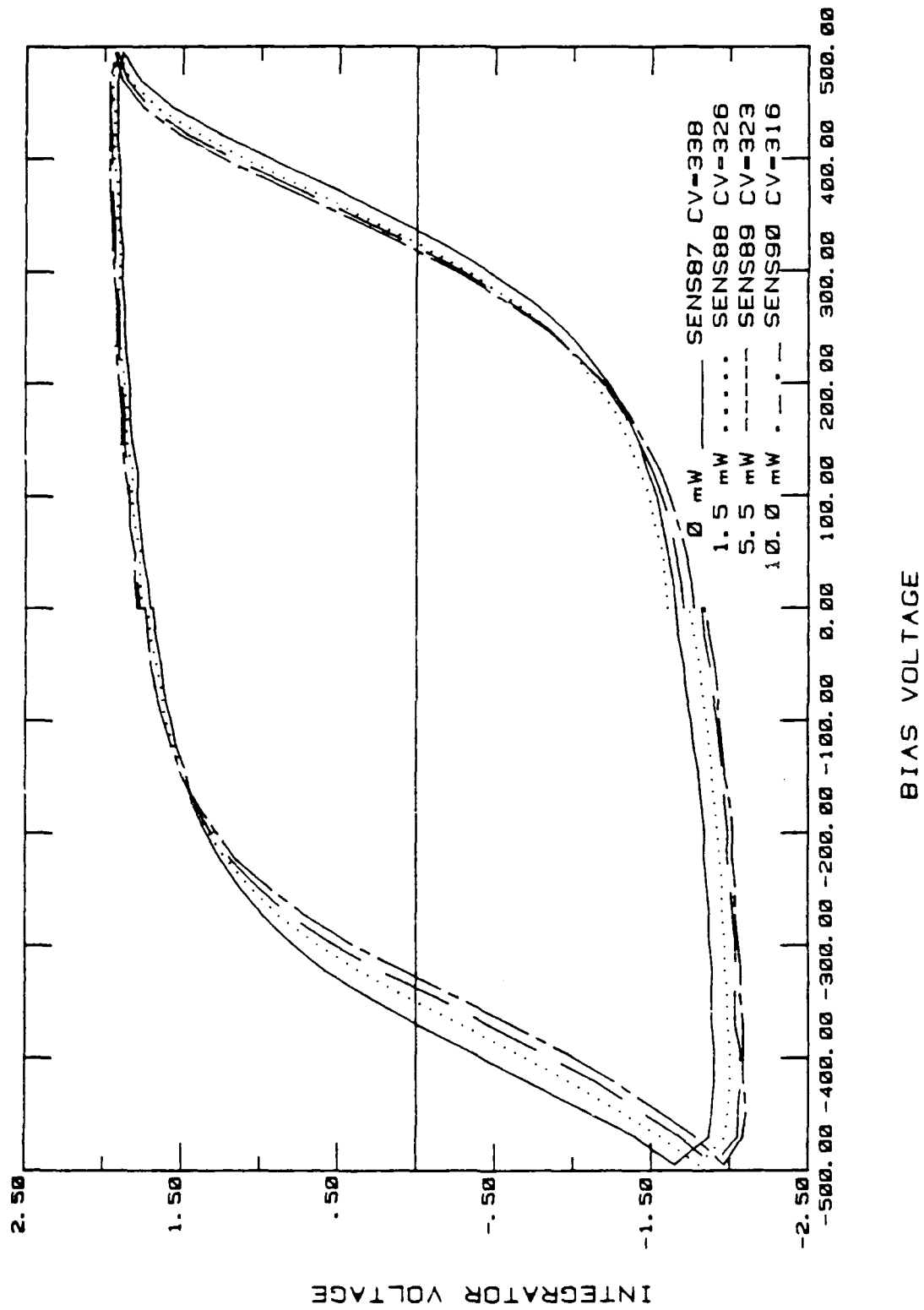


Figure 40. Sensitivity run, sample 9/13C; 1.5, 5.5, and 10 mW at 520.8 nm.

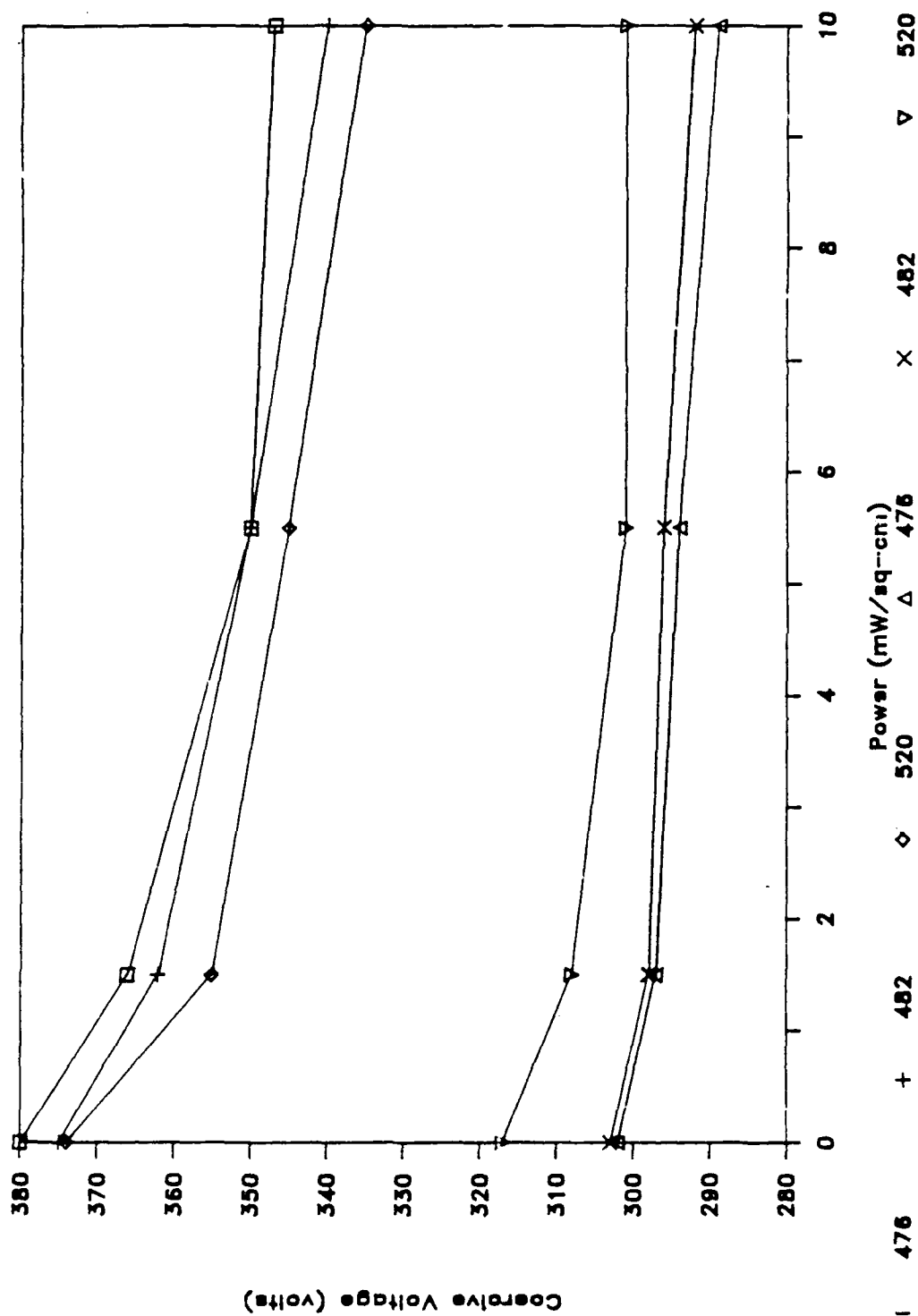


Figure 41. USAF PLZT adaptive optics - sensitivity: 9/13C(a) and 9/22B.



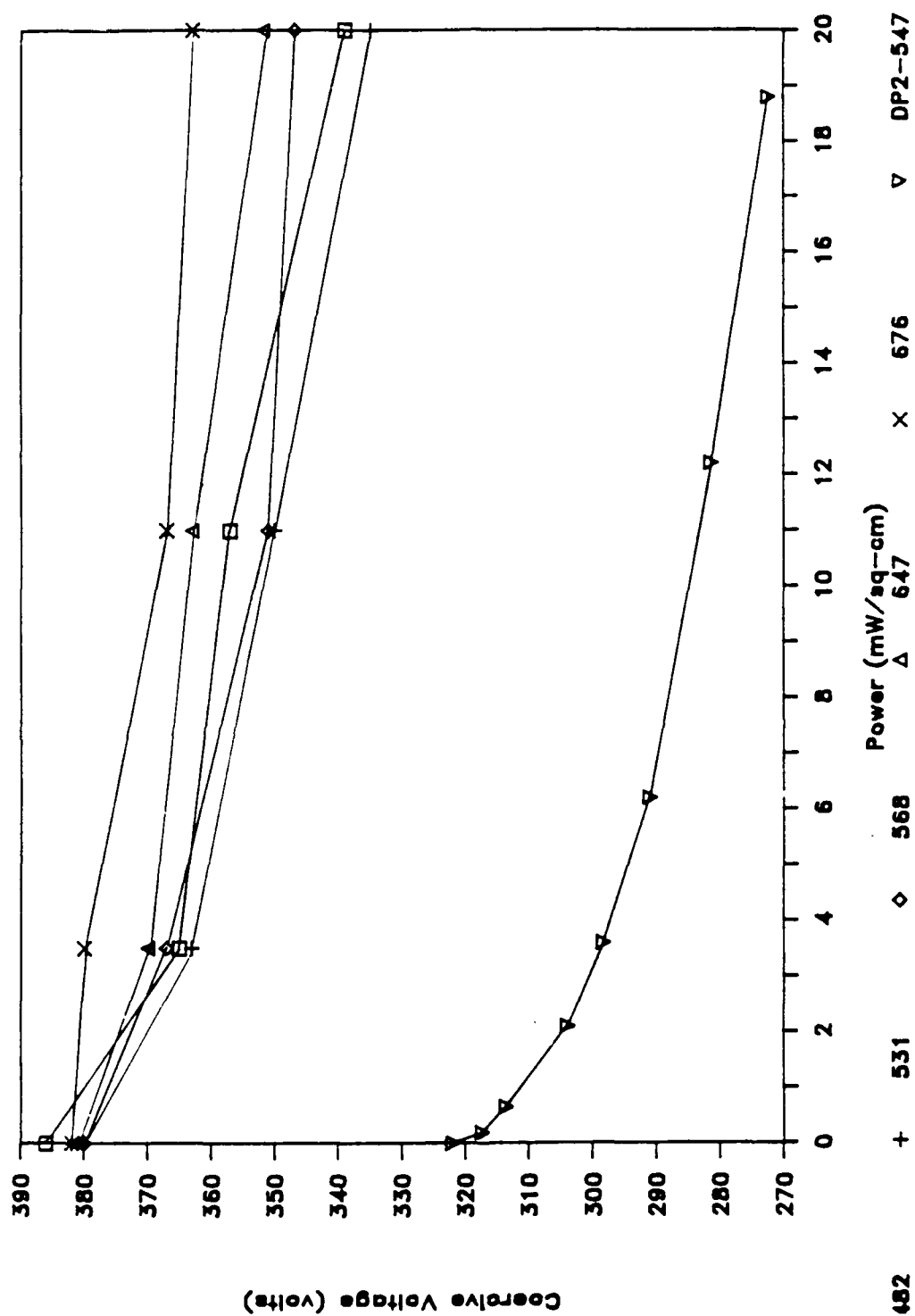


Figure 42. USAF PLZT adaptive optics - sensitivity: 9/13C(e) and DP2-547.

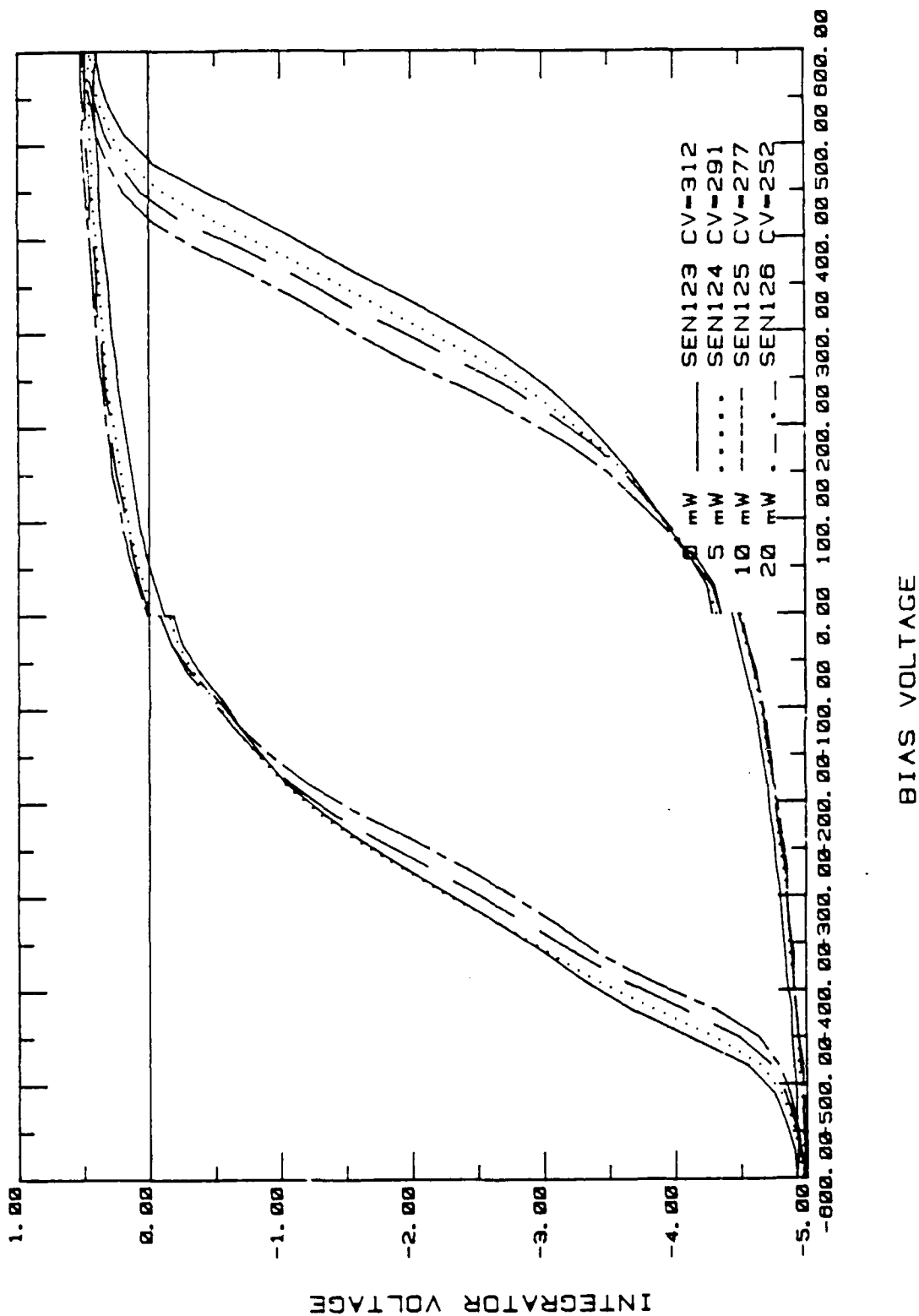


Figure 43. Sensitivity run, sample 7/24A (1.3 MeV Al plus 1.3 MeV Ne);  
0, 5, 10, and 20 mW at 4/6.2 nm.

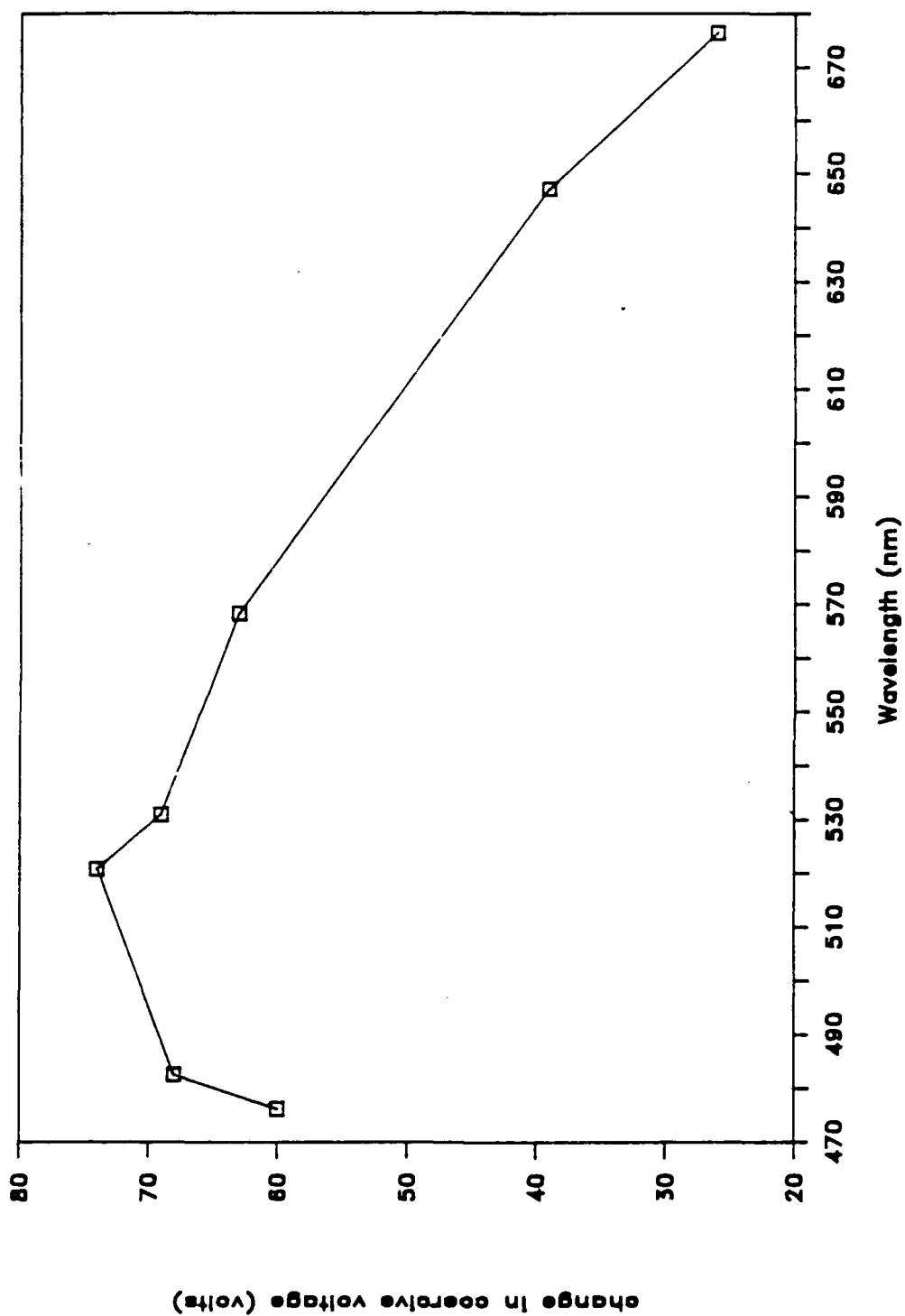


Figure 44. USAF PLZT adaptive optics - sensitivity: 7/24A.

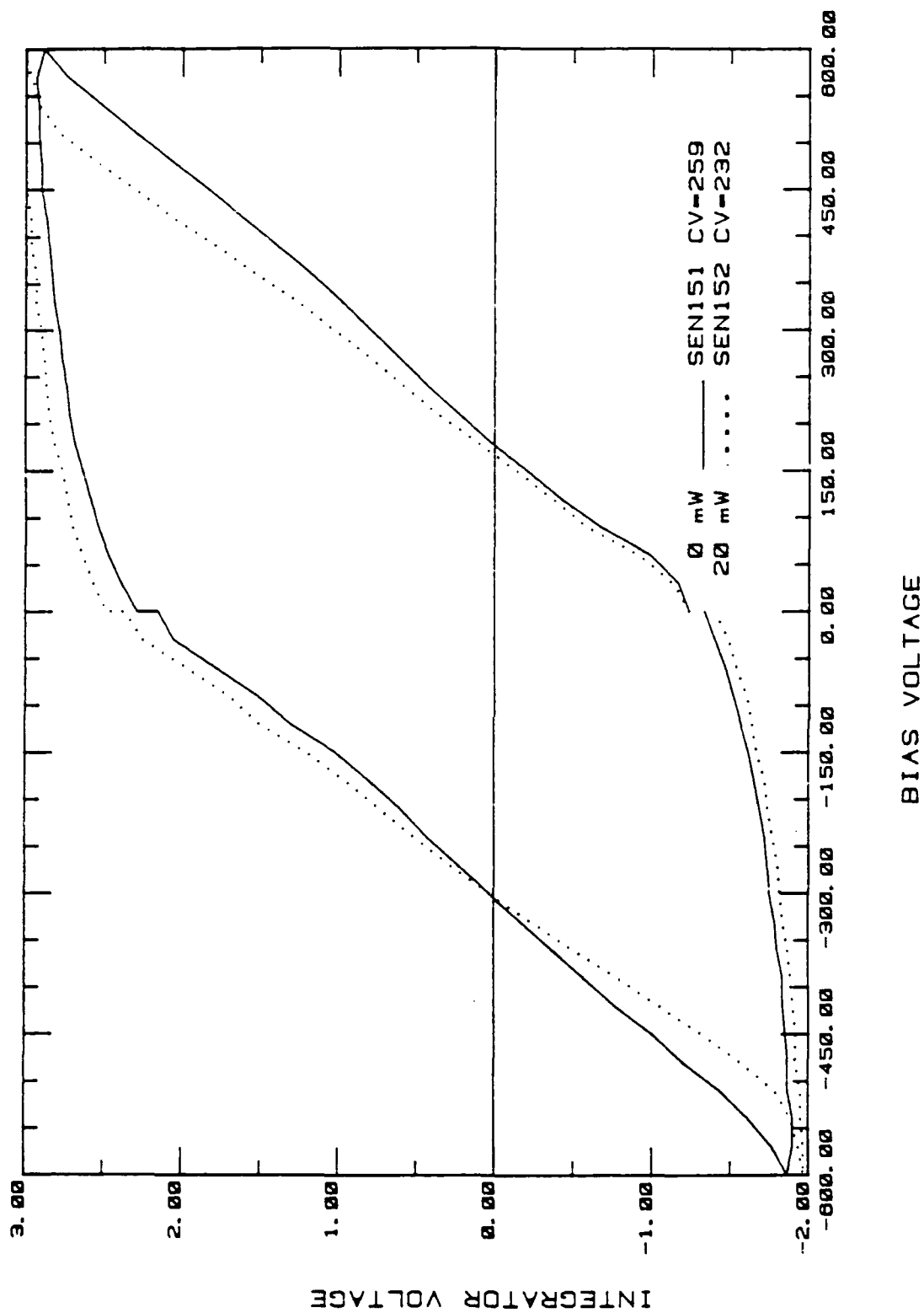


Figure 45. Sensitivity run, sample 7/24A (10- $\mu$ F capacitor) after reanneal; 0 and 20 MW at 476.2 nm.

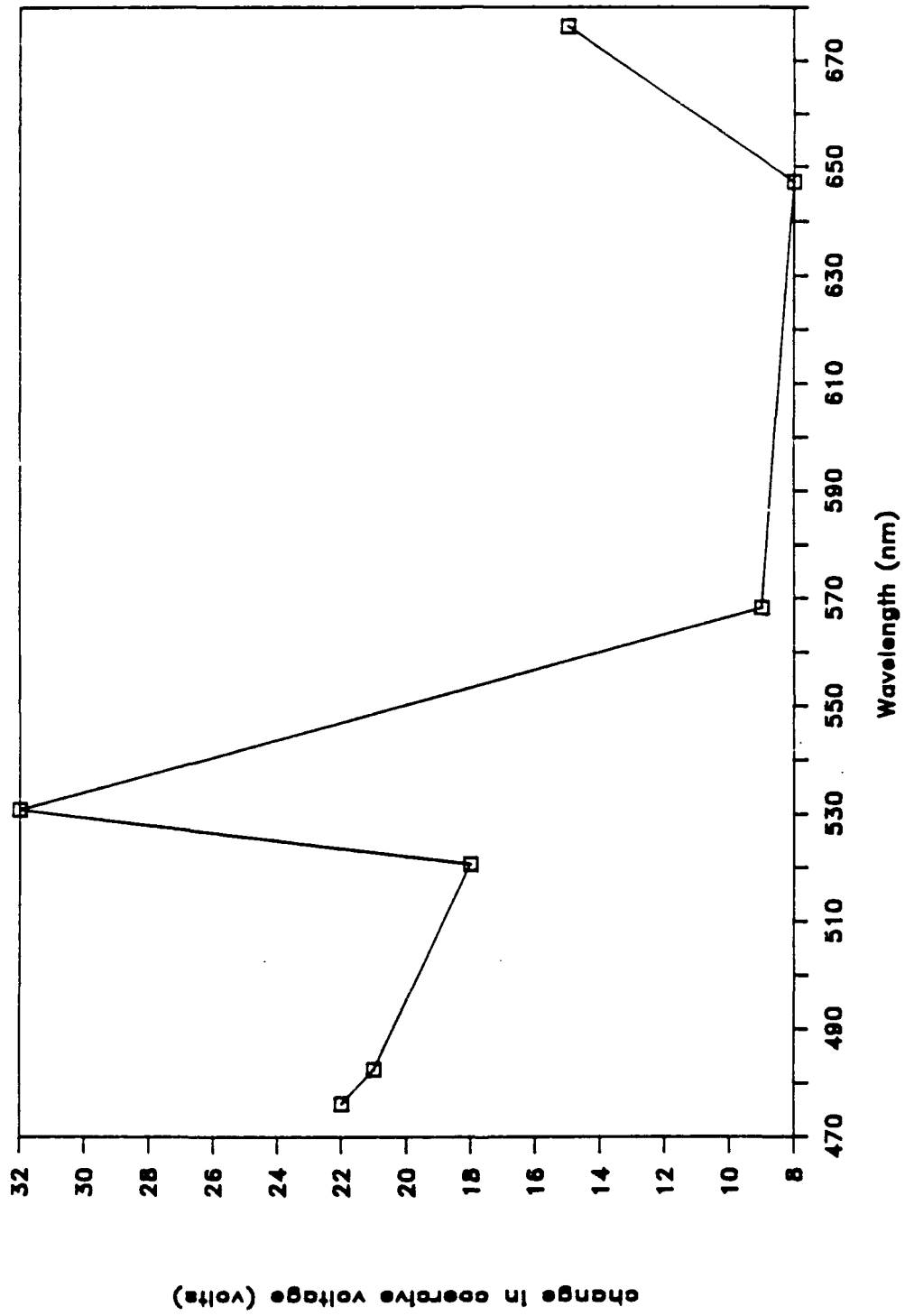


Figure 46. USAF PLZF adaptive optics - sensitivity after anneal: 7/24A.

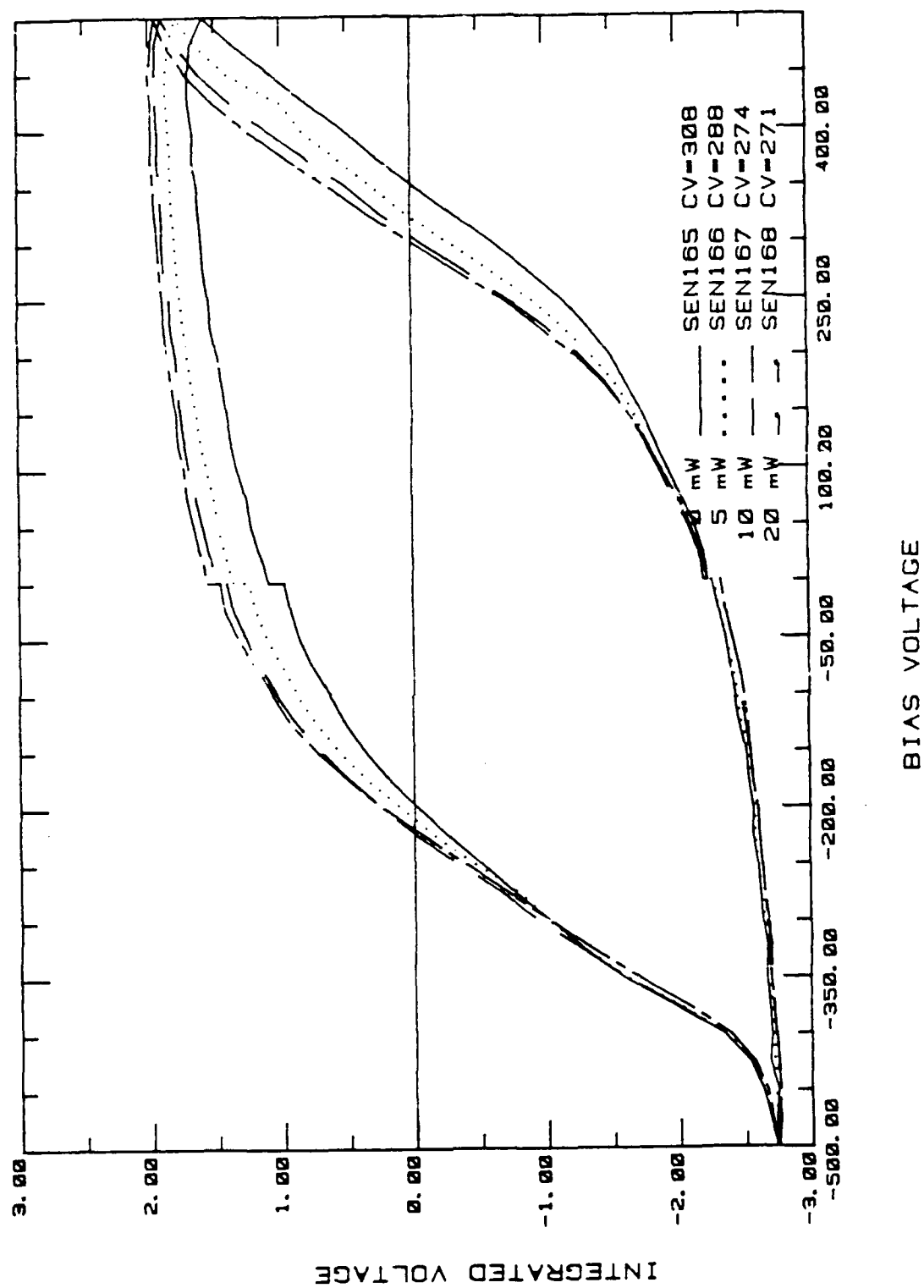


Figure 41. Sensitivity run, sample 1/23D, 7/70/30 (1.3 MeV Cr plus 1.3 MeV Ne); 0, 5, 10, and 20 MW at 476.2 nm.

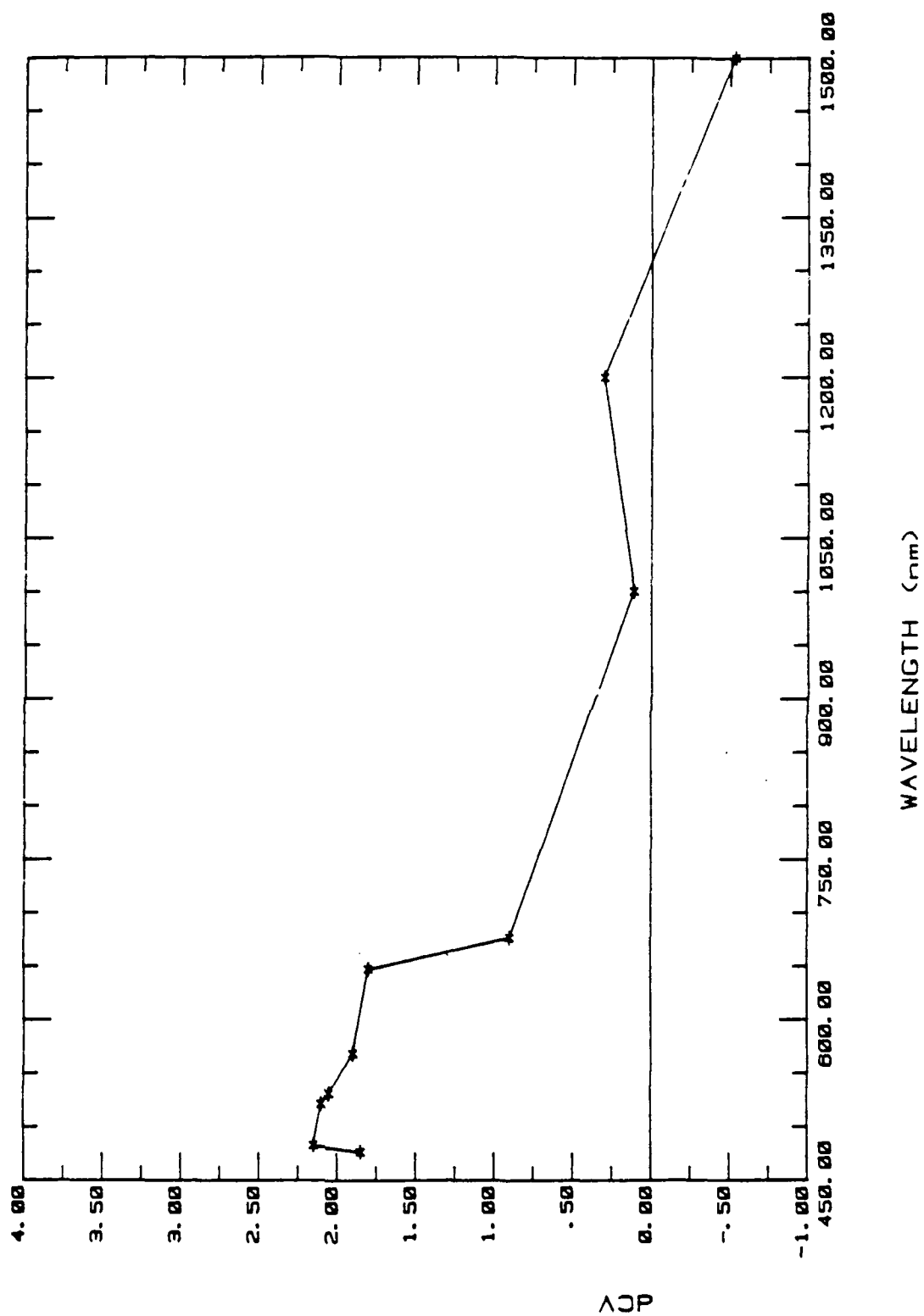


Figure 48. Change in CV per change in beam power, sample 1/23D, file DCVIR1, combination of  $Kr^+$  laser and Xe lamp results.

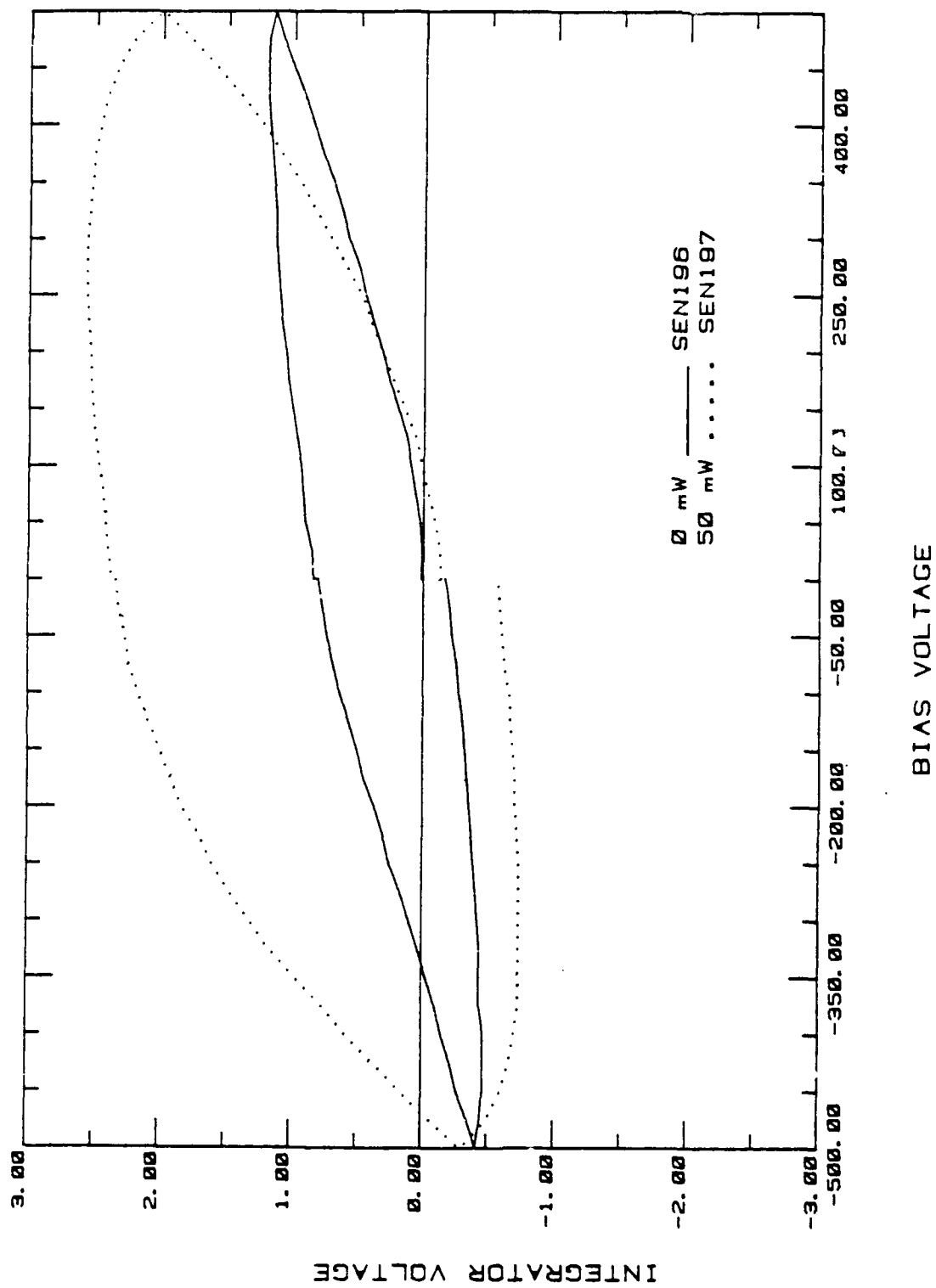


Figure 49. Sensitivity run, sample 9/20A; 0 and 50 MW at 476.2 nm.



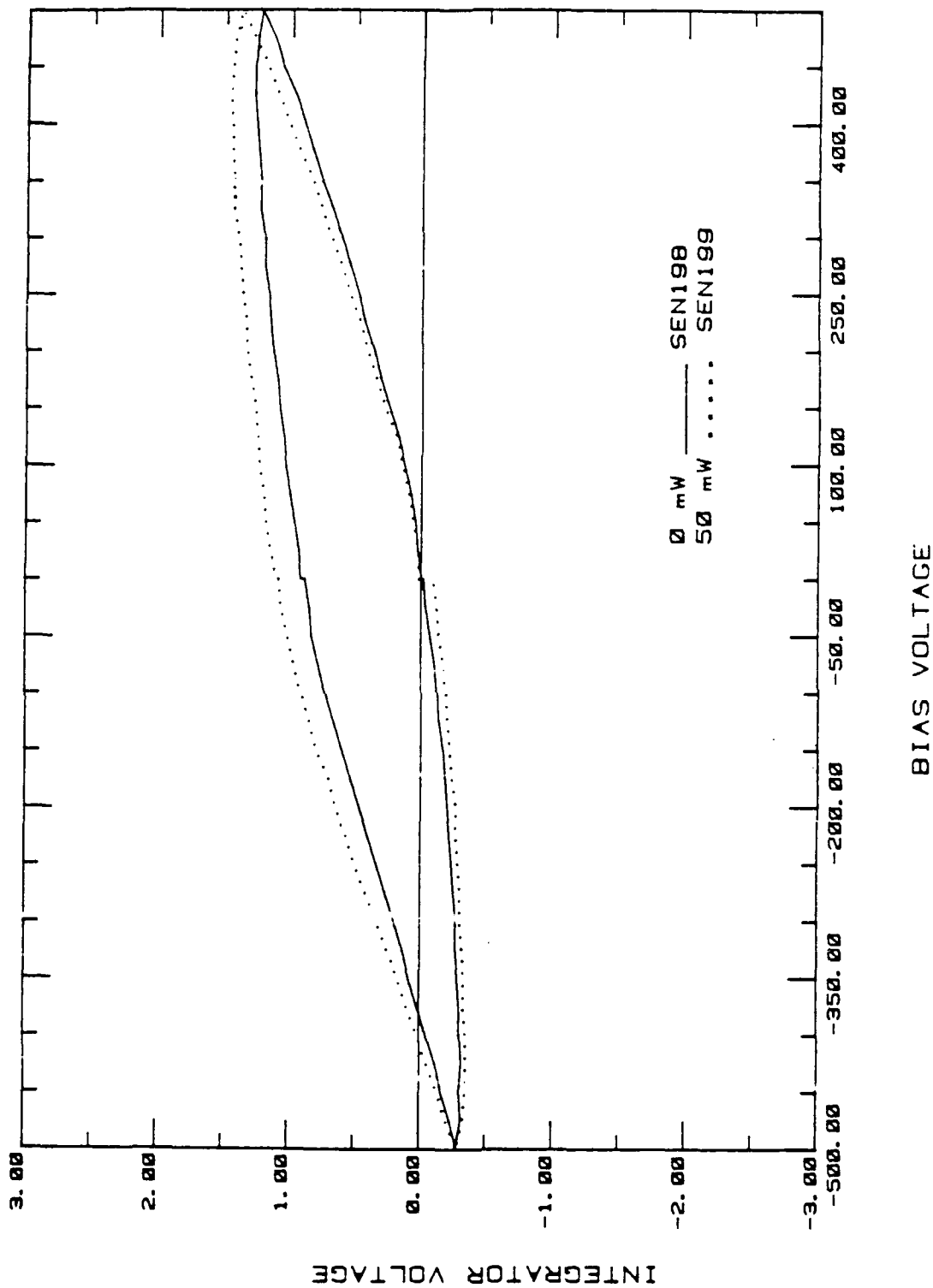


Figure 50. Sensitivity run, sample 9/20A; 0 and 50 mW at 676.4 nm.

CHANGE IN CV PER CHANGE IN BEAM POWER  
 476.2 nm TO 676.4 nm  
 SAMPLE 9/12C (C+,O+++)  
 FILE: DCV227

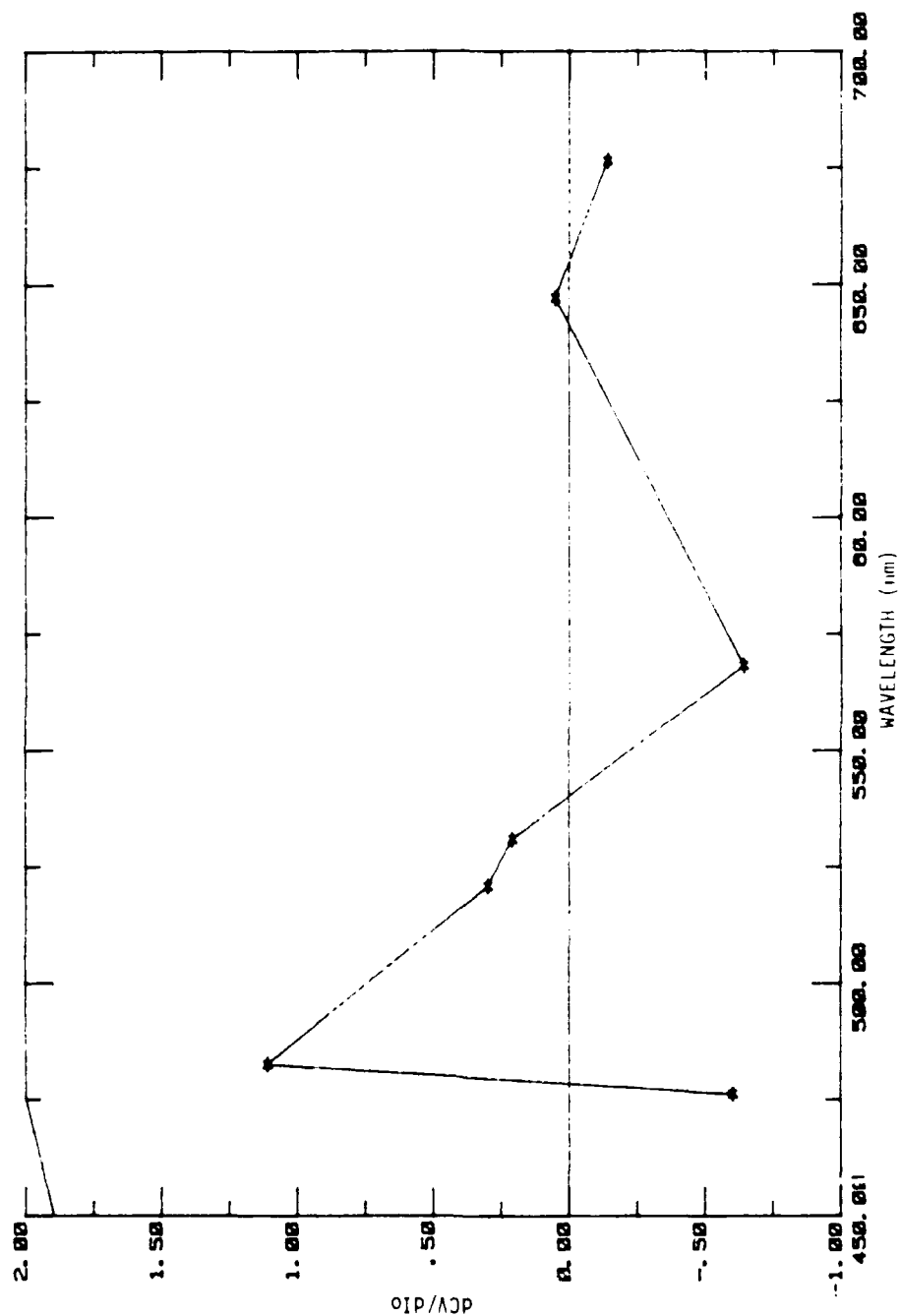


Figure 51. Spectral photosensitivity of C<sup>+</sup>-O<sup>+</sup> coimplanted PLZT, sample 9/12C.

CHANGE IN CV PER CHANGE IN BEAM POWER  
 476.2 nm TO 676.4 nm  
 SAMPLE 9/11B (C+ 0+) FILE: DCV212

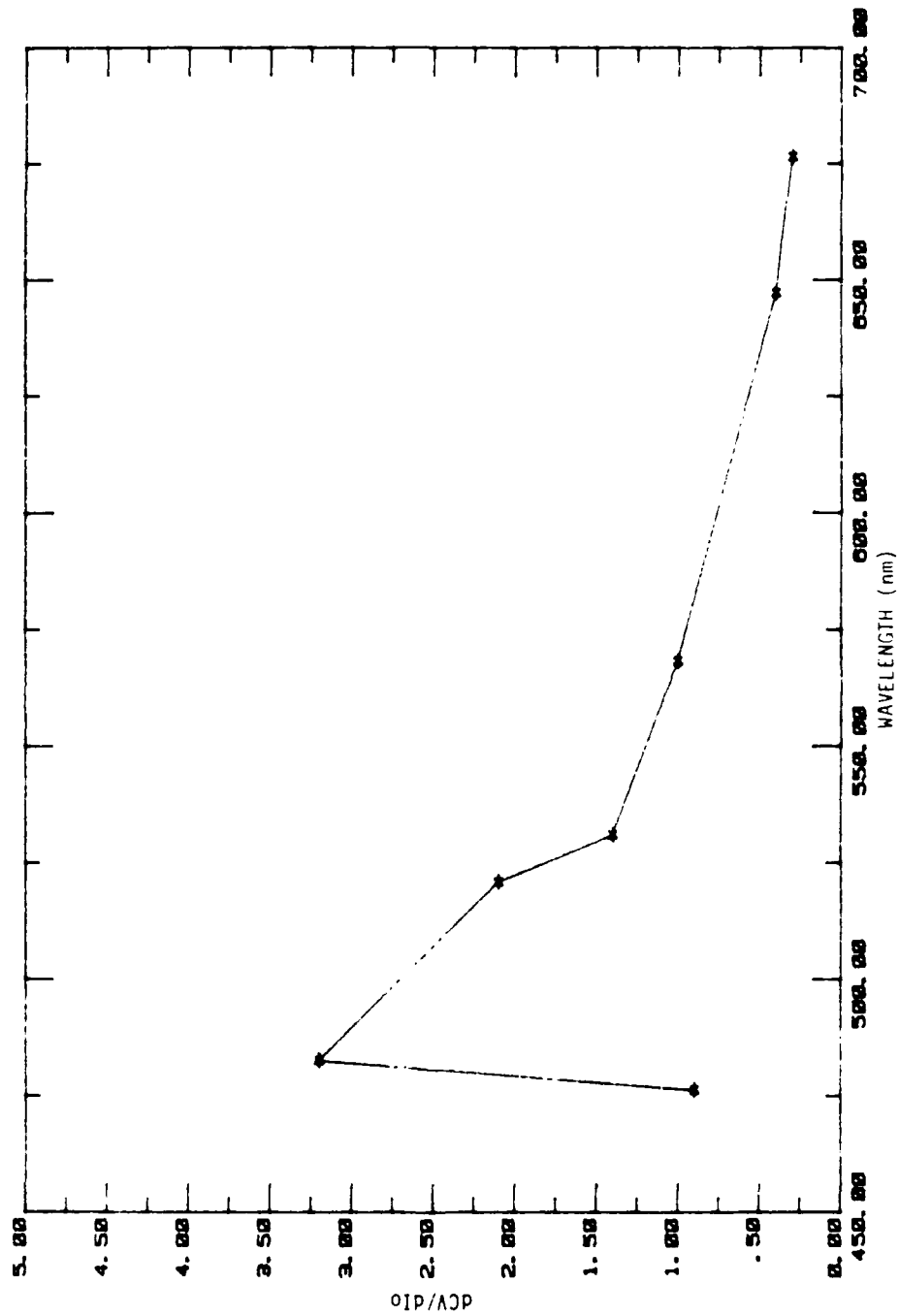
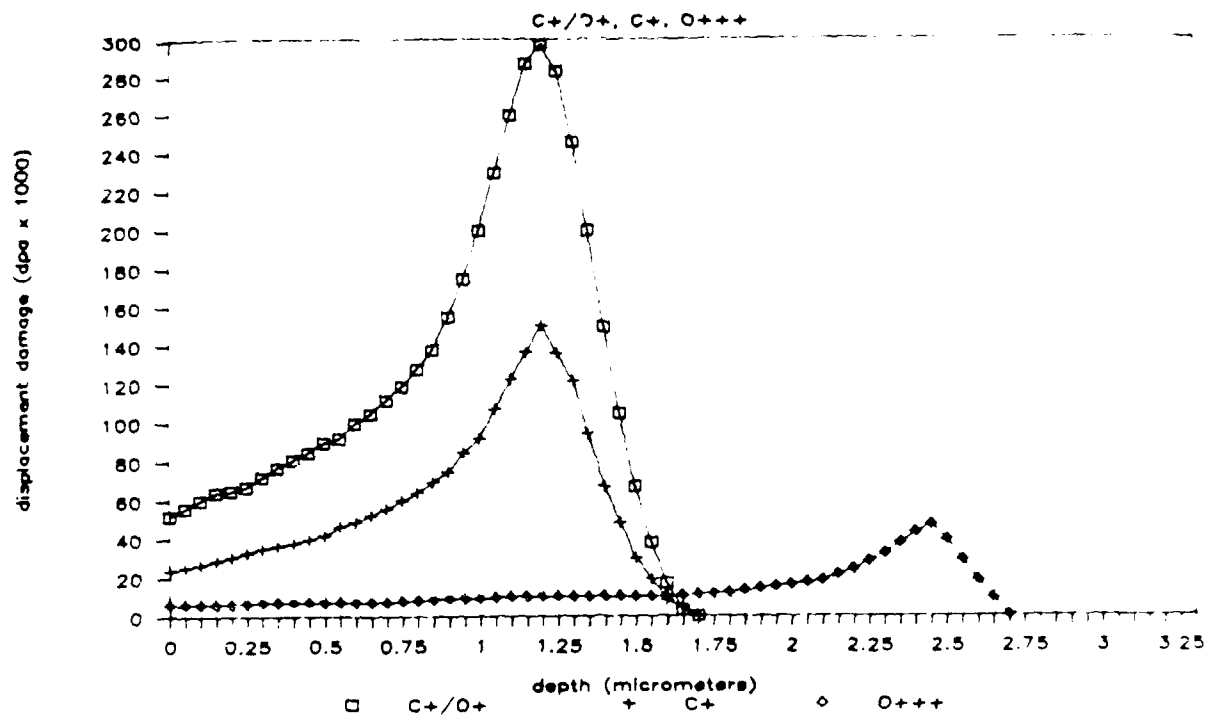
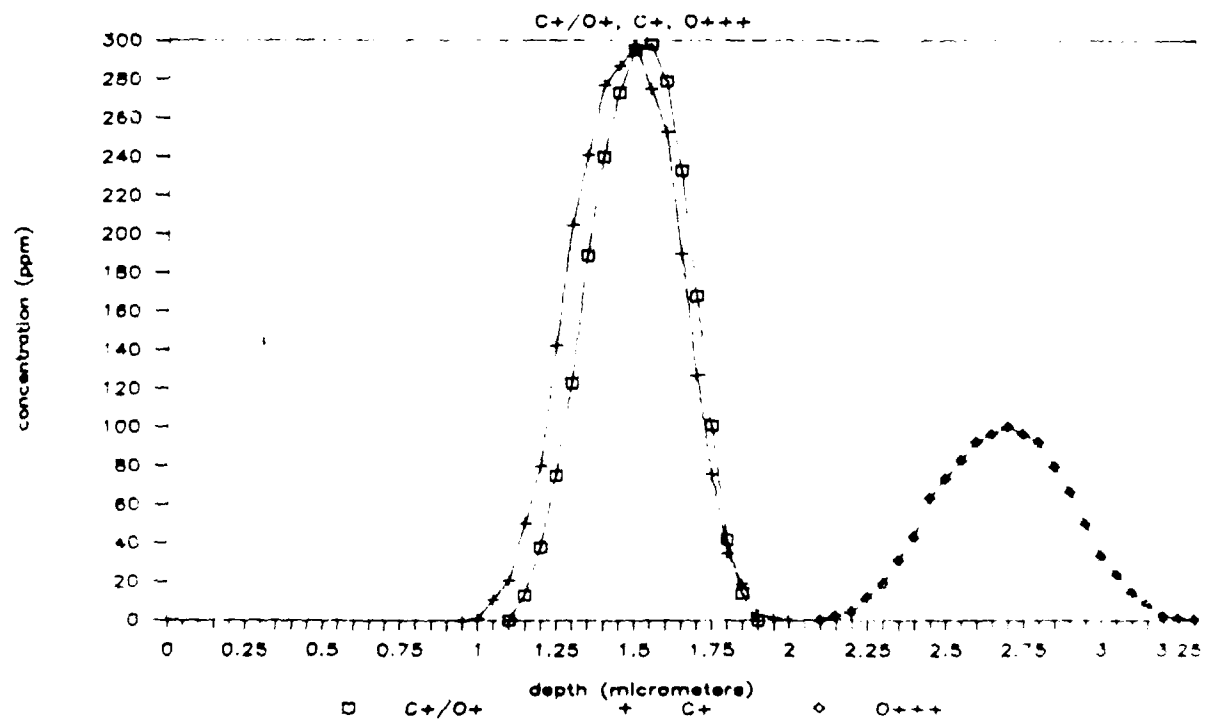


Figure 52. Spectral photosensitivity of C<sup>+</sup>-O<sup>+</sup> coimplanted PLZF, sample 9/11B.



(a) Implantation damage profile.



(b) Implanted ion depth profile.

Figure 53. Implantation profiles.

SAMPLE 9/12C (C<sup>+</sup>, O<sup>3+</sup>) FILE: PC0001  
 PHOTOCONDUCTIVE MODE, 50V BIAS  
 WAVELENGTH SELECTION VIA BANDPASS FILTERS

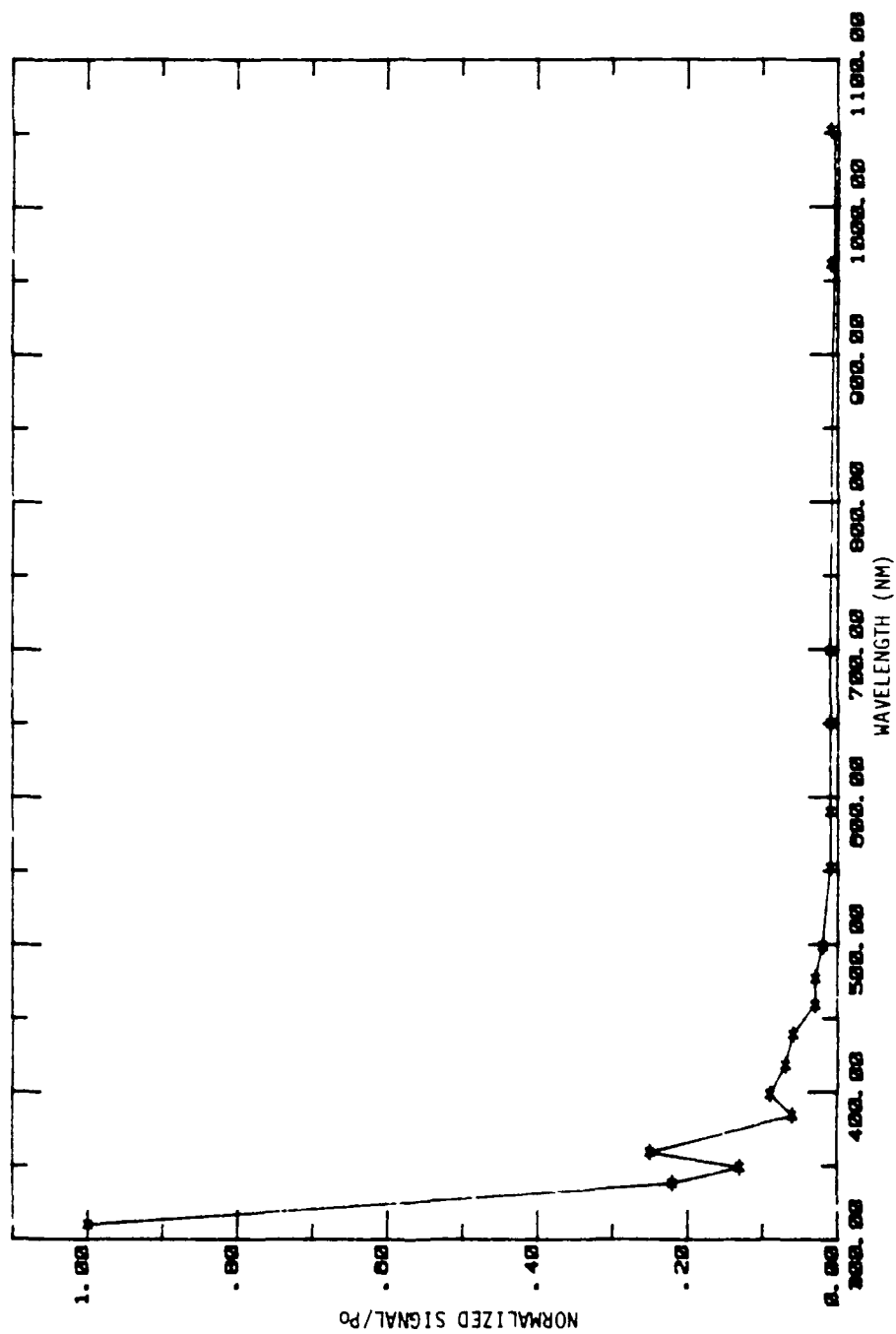


Figure 54. Preliminary test of spectral photoconductivity method for C<sup>+</sup>, O<sup>3+</sup> implanted PLZT.

SAMPLE 9/10A (C+,0+) FILE: PC00002  
 PHOTOCONDUCTIVE MODE, 50V BIAS  
 WAVELENGTH SELECTION VIA BANDPASS FILTERS

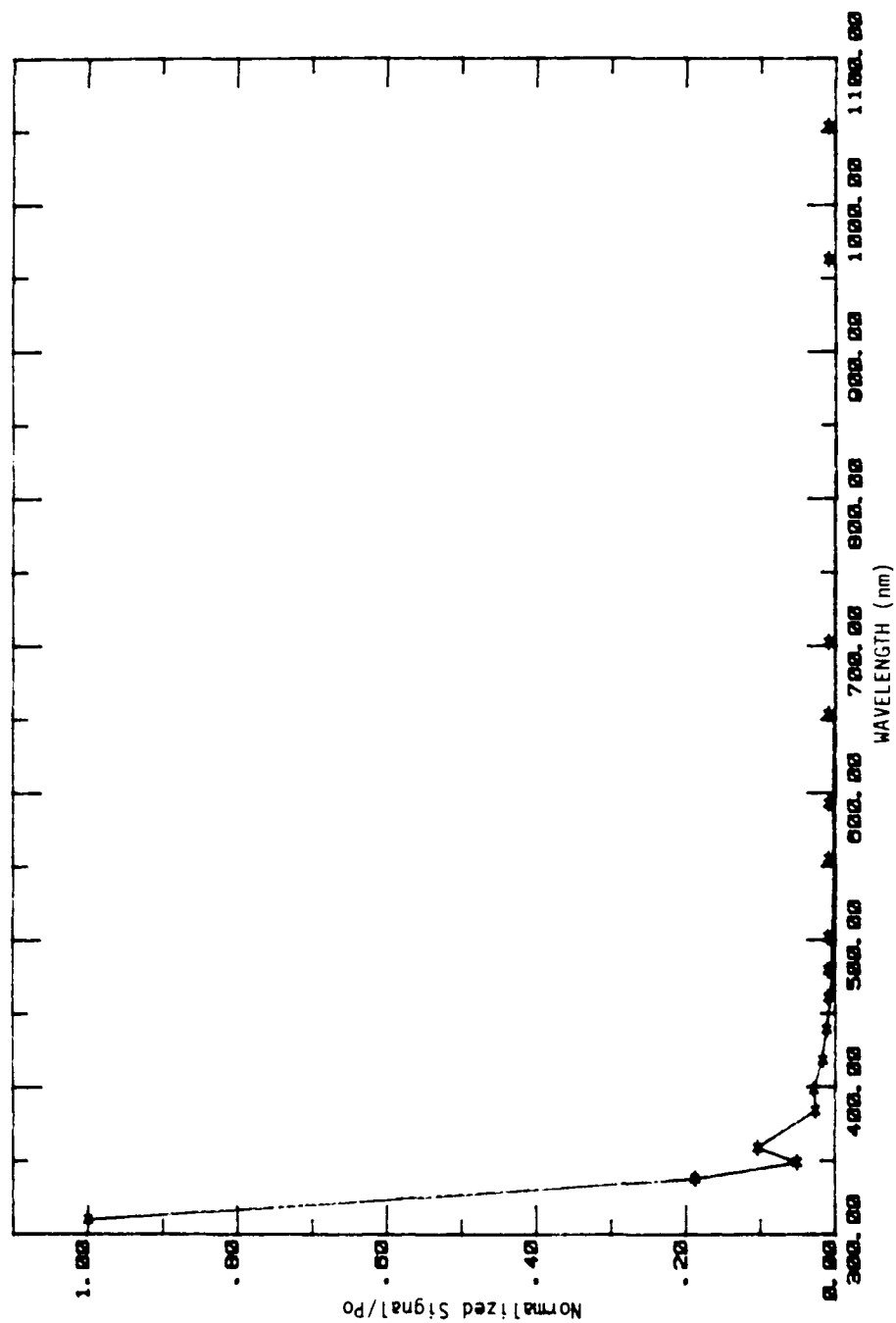


Figure 55. Preliminary test of spectral photoconductivity method for C<sup>+</sup>, O<sup>+</sup> implanted PLZT.

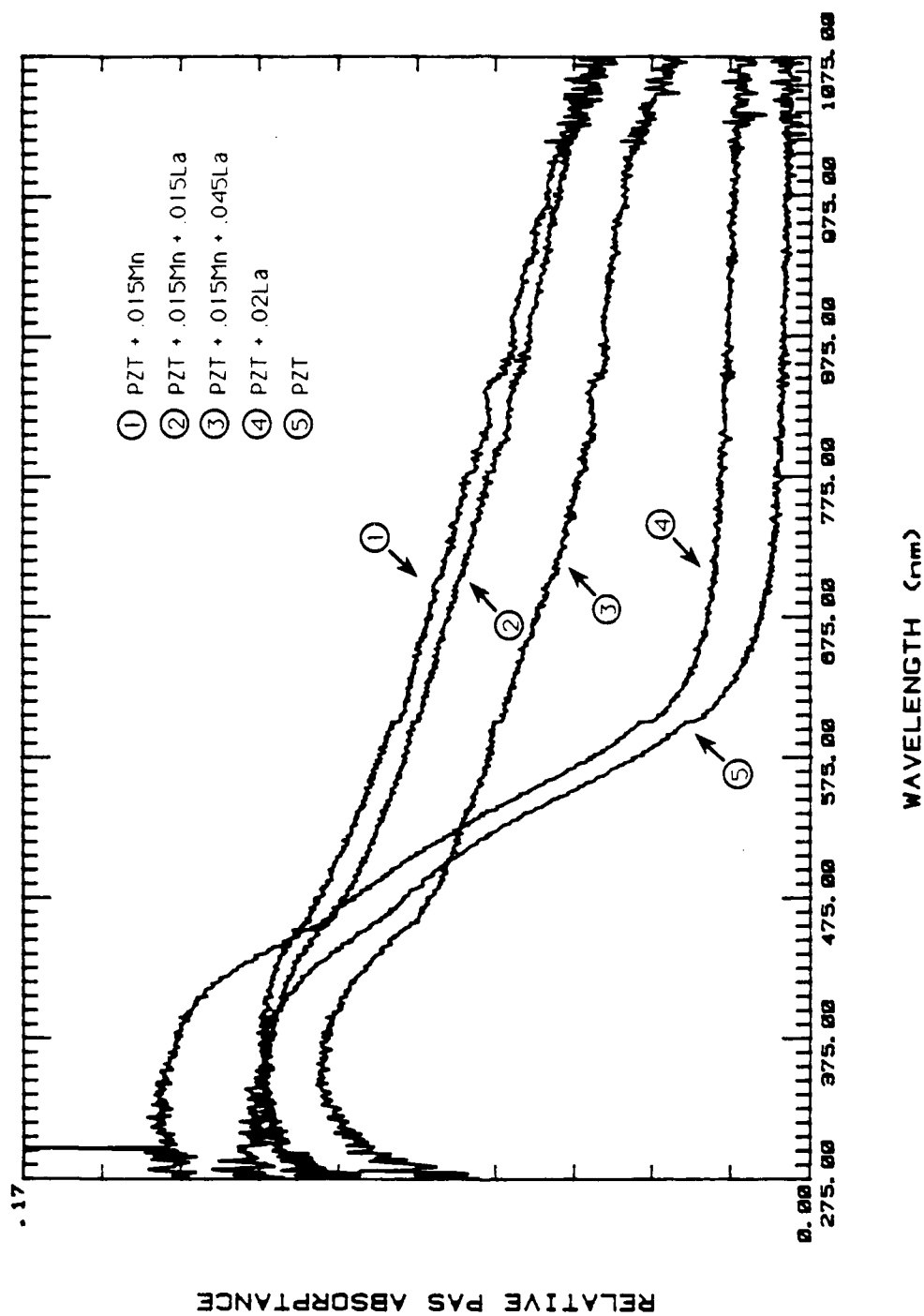


Figure 56. Photoacoustic spectra of PZT and doped PZT.

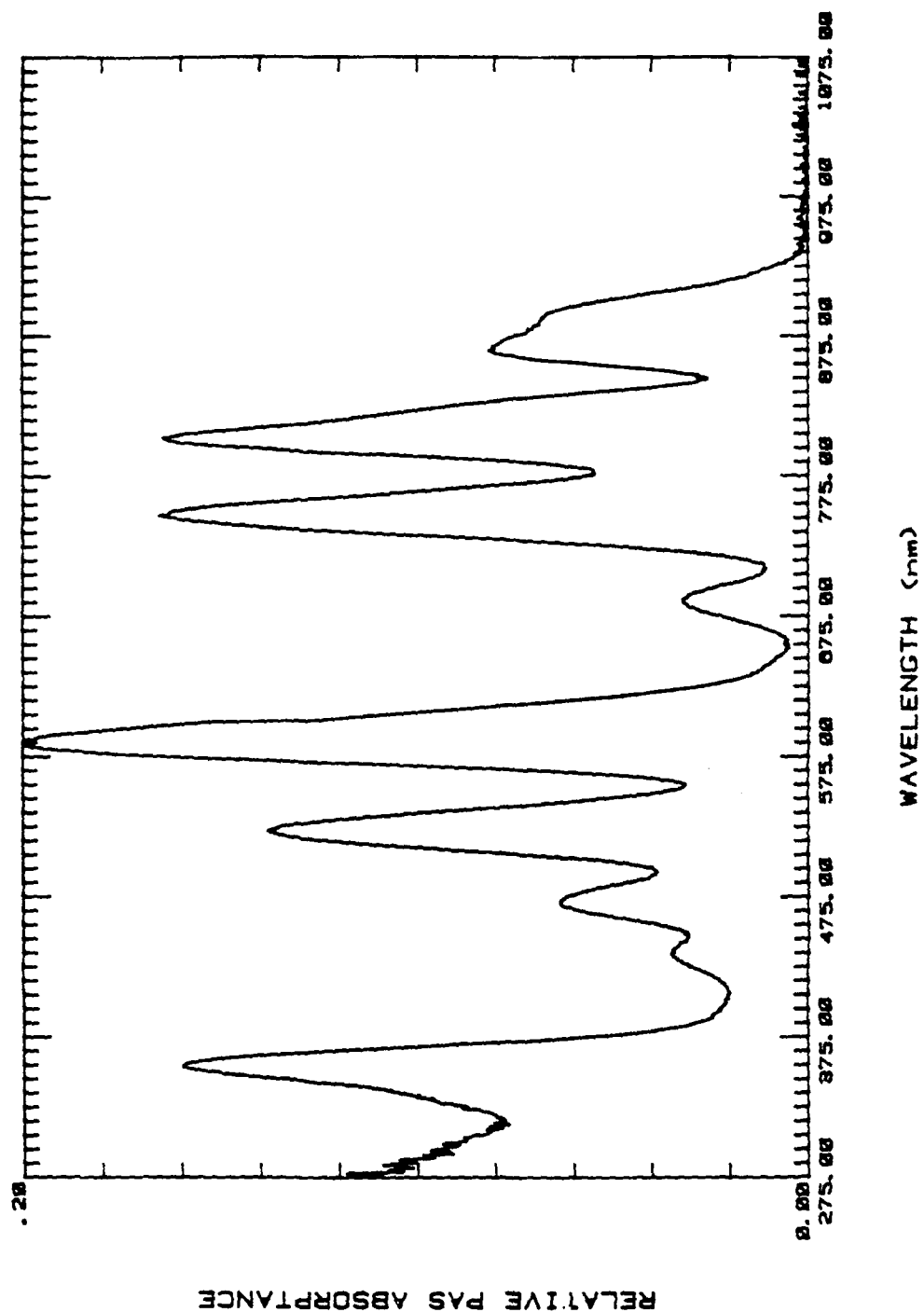


Figure 57. Photacoustic spectrum of neodymium-oxide.



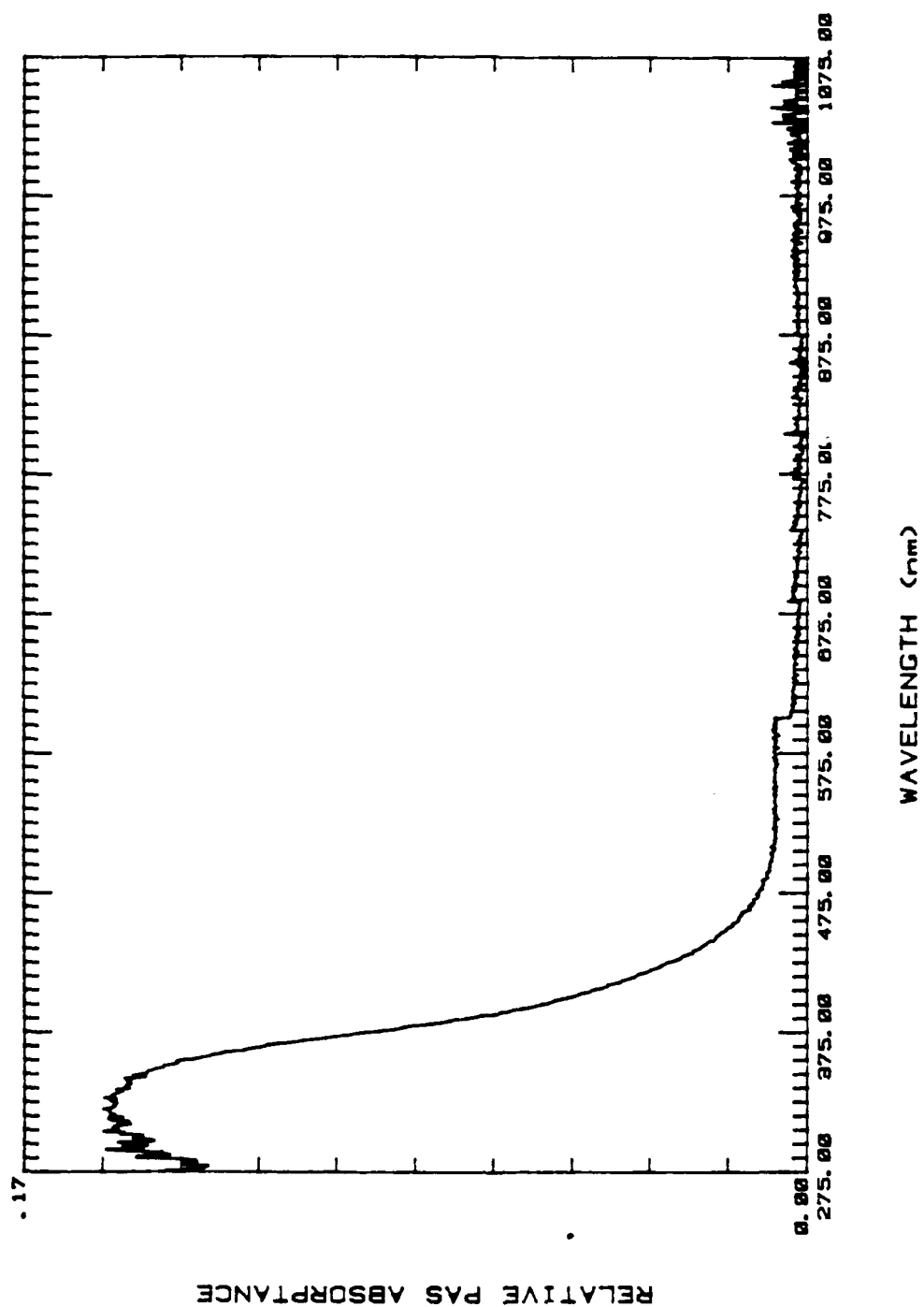


Figure 58. Photoacoustic spectrum of crushed 70/65 unimplanted PLZT.

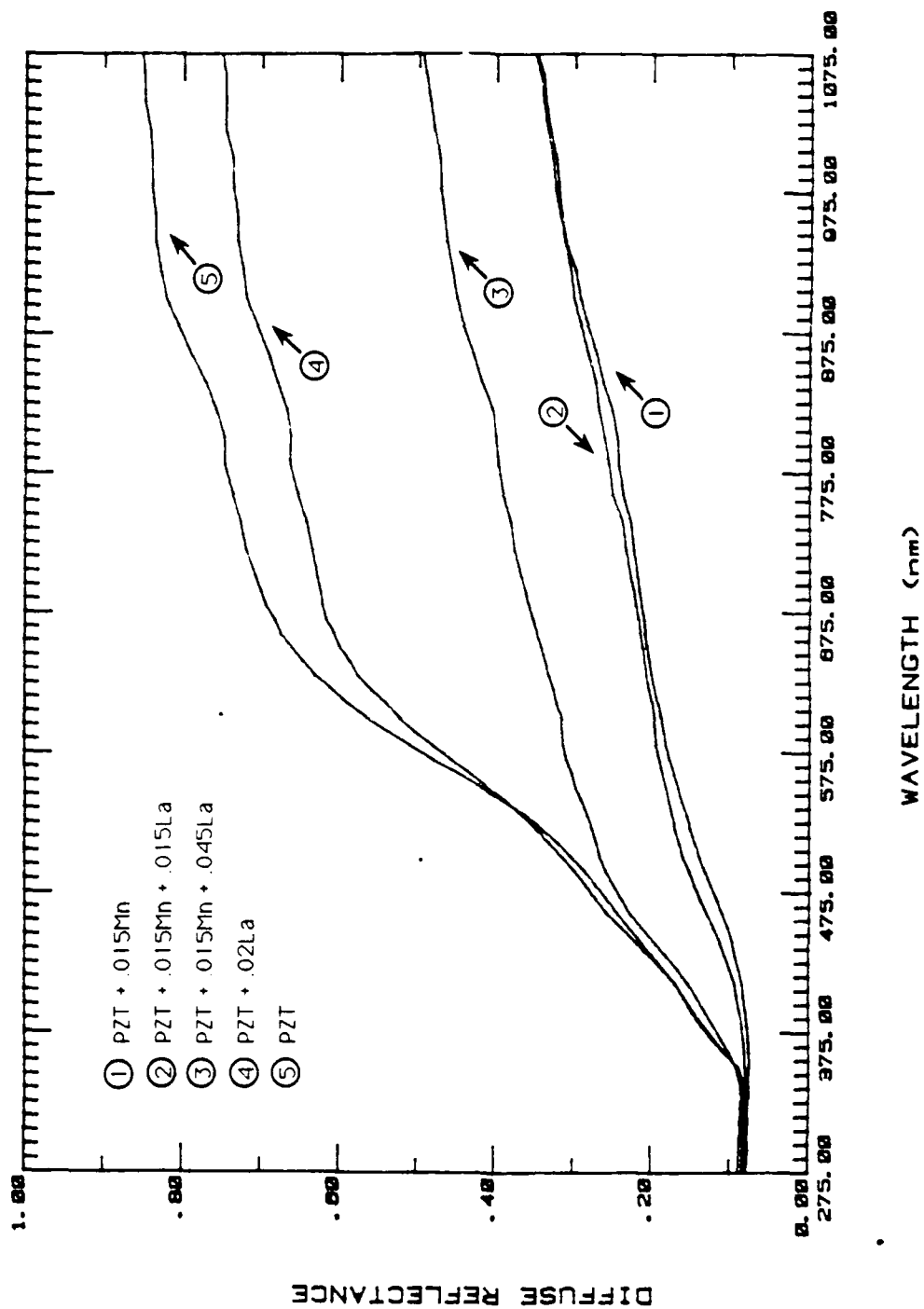


Figure 59. Diffuse reflectance spectra of undoped and doped PZT.

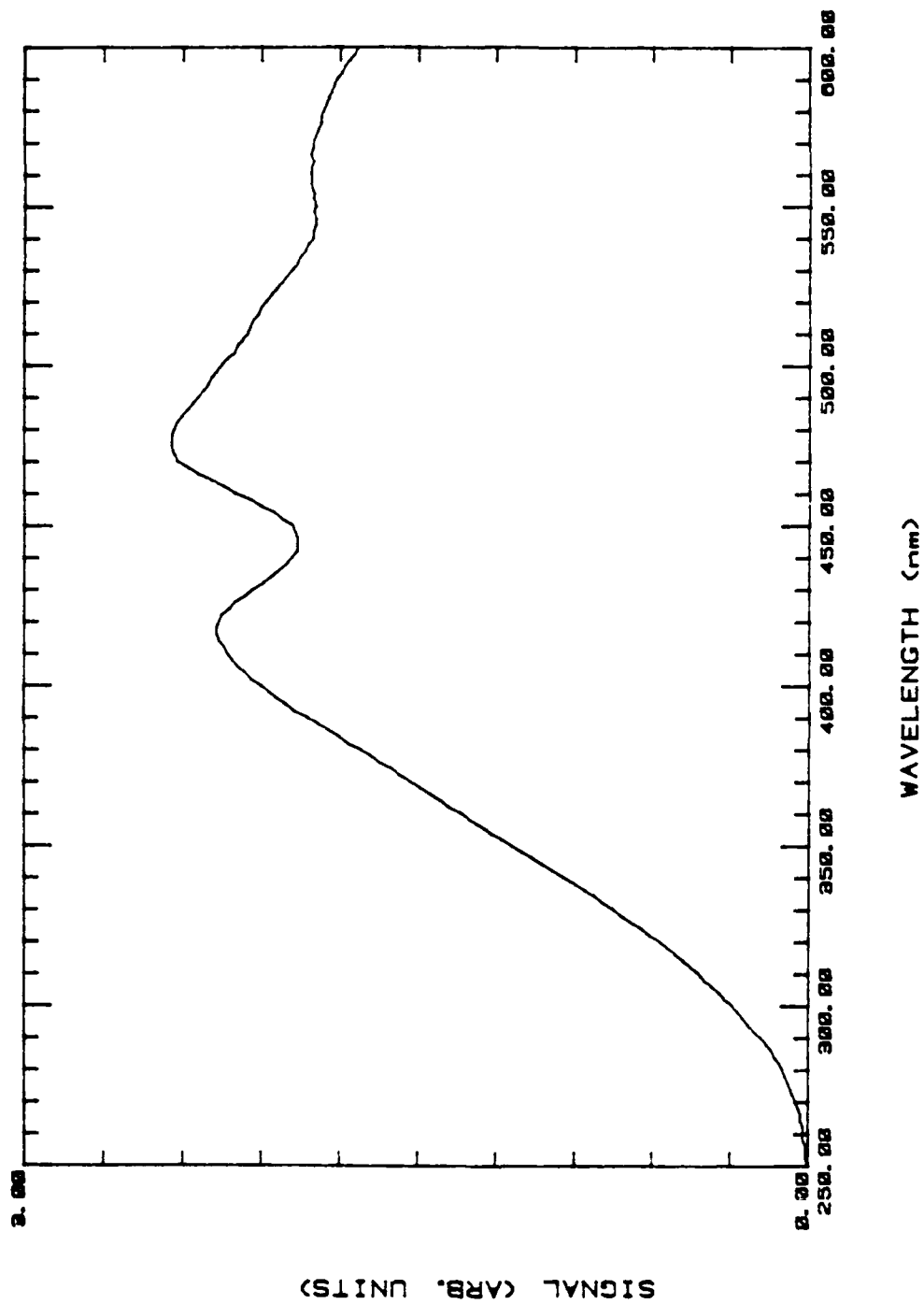


Figure 60. Spectral content of Xenon-arc lamp/monochrometer combination.

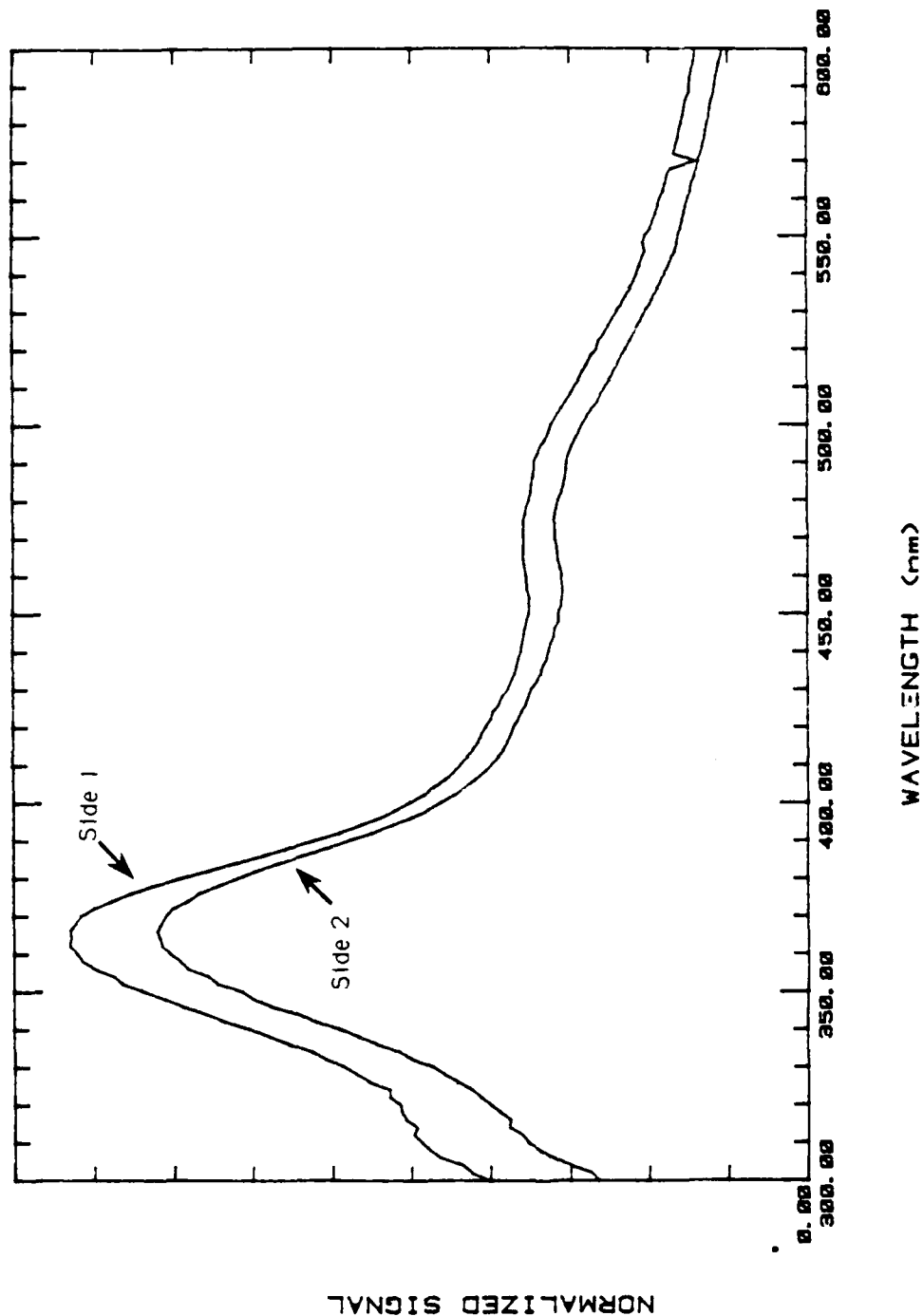


Figure 61. Pyroelectric response for virgin PLZT sample 7/51. Upper curve, side1; lower curve, side 2. The difference in amplitudes for the two sides ascribed to geometry change.

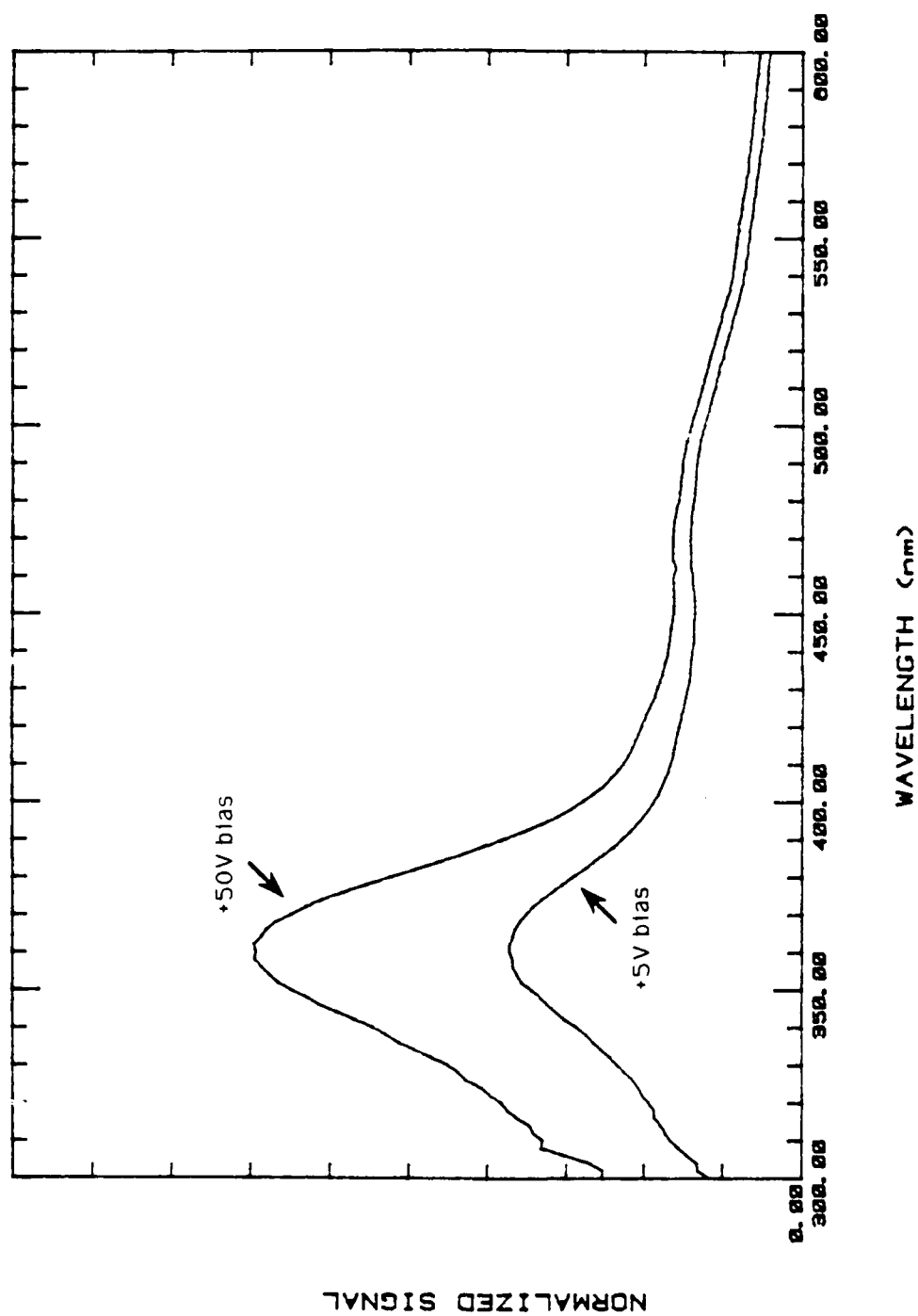


Figure 62. Photoconductivity response for sample 7/51. Upper curve bias is +50 V; lower curve bias is +5 V.

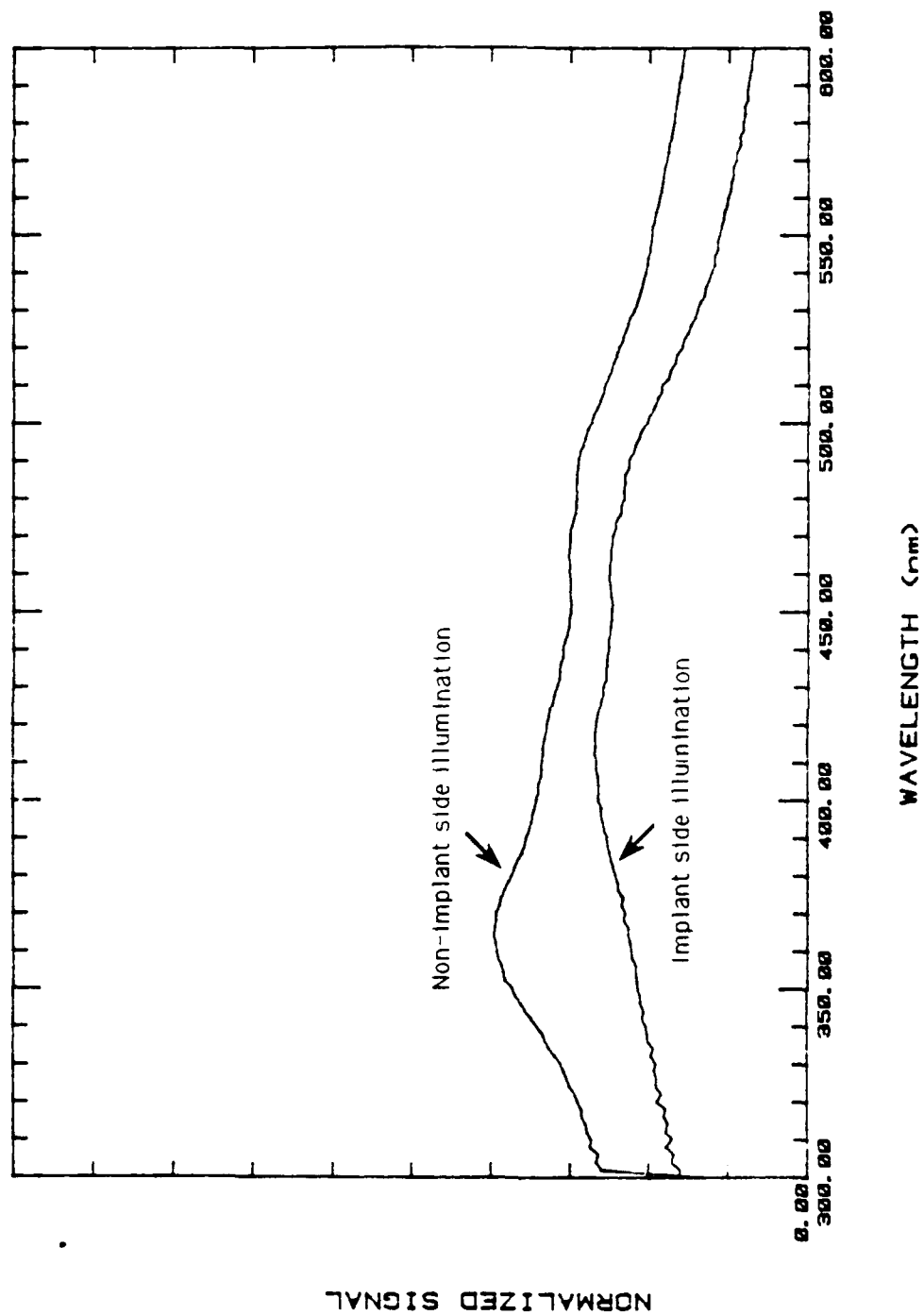


Figure 63. Pyroelectric response for sample 9/10B, 0.3+, C+ dual implant. Upper curve is for illumination on nonimplanted side; lower curve is for illumination on implanted side.

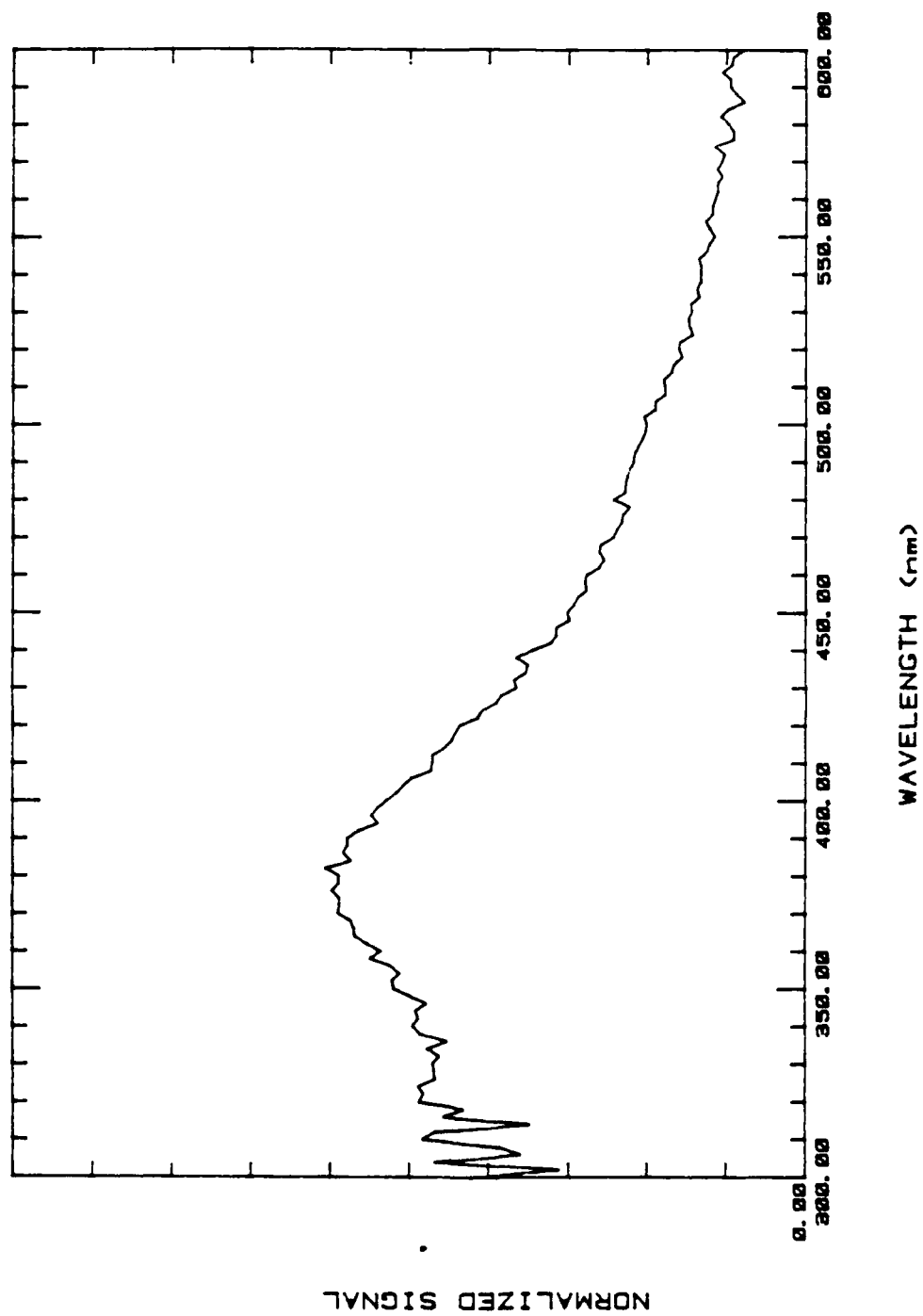


Figure 64. Pyroelectric response for sample 9/21B, a triple-Ni<sup>+</sup> implant, nonimplanted side.

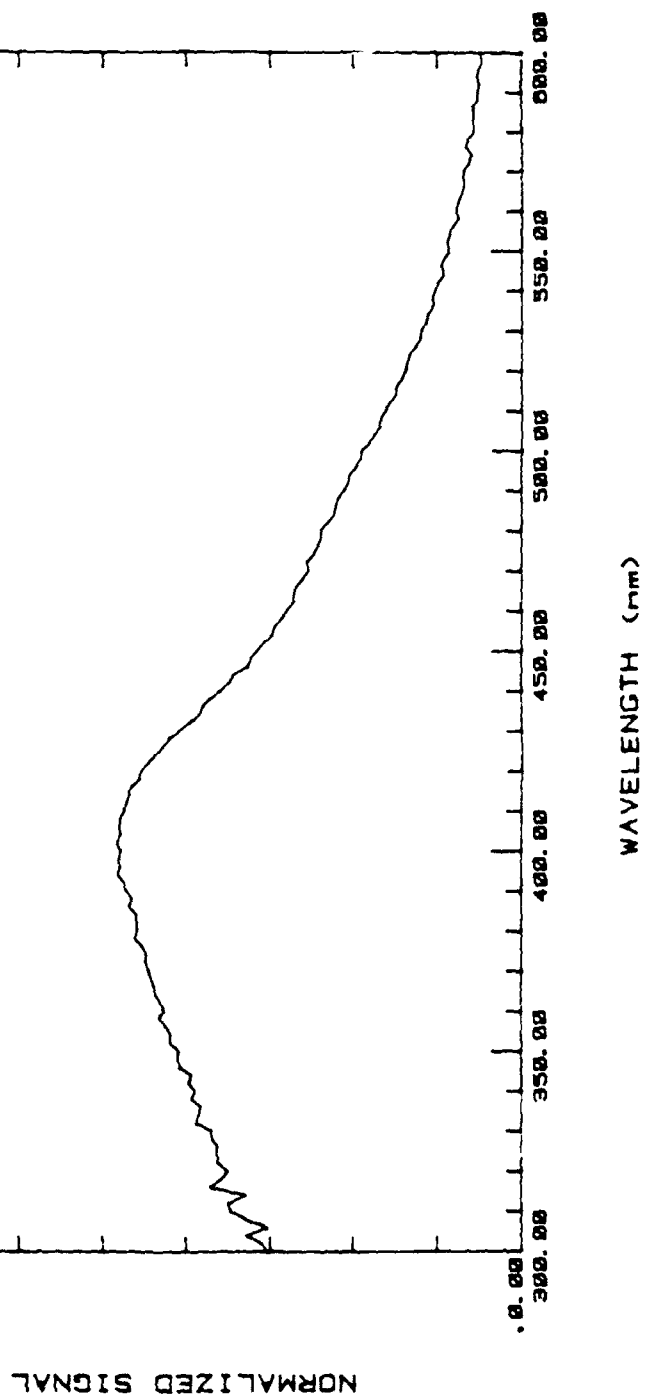


Figure 65. Pyroelectric response for sample //21B, a triple-Ni<sup>+</sup> implant, implanted side.



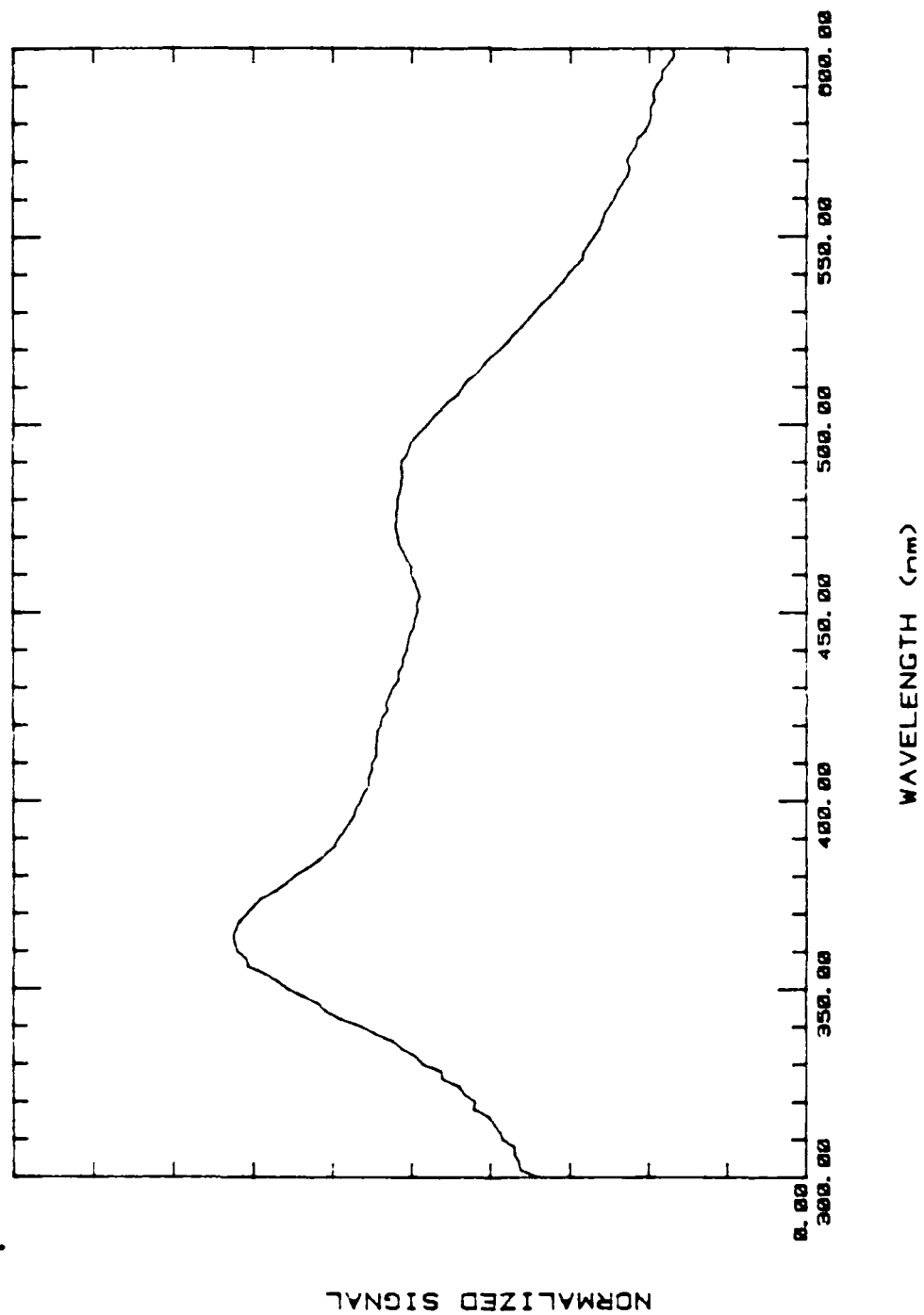


Figure 66. Pyroelectric response for sample 9/18B, an  $\text{Ne}^+$ ,  $\text{Ni}^+$  dual-implant, nonimplanted side illuminated.

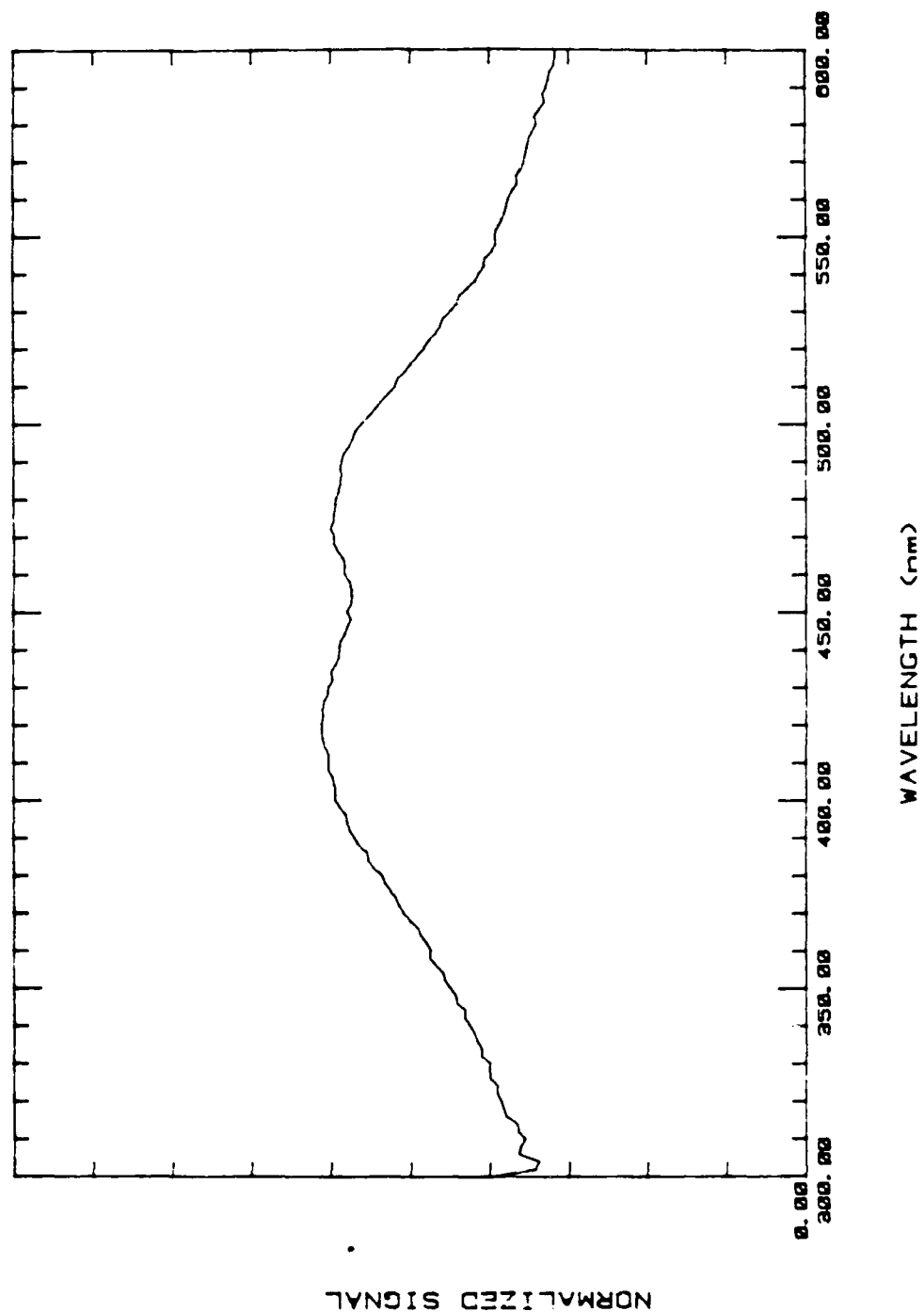


Figure 67. Pyroelectric response for sample 9/18B, an  $\text{Ne}^+$ ,  $\text{Ni}^+$  dual-implant, implanted side illuminated.

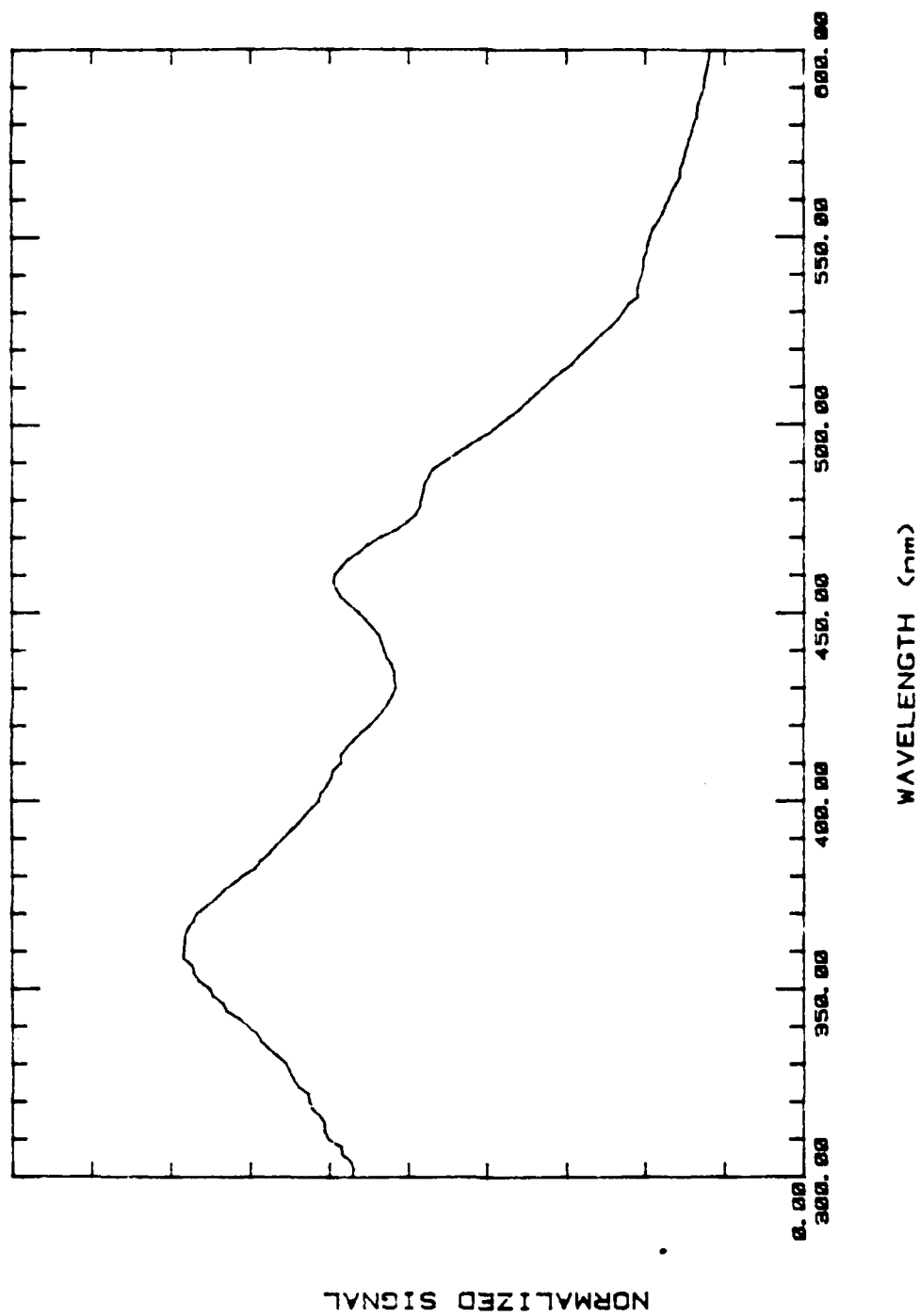


Figure 68. Pyroelectric response for sample 9/10A, an  $O^+$ ,  $C^+$  dual-implant, nonimplanted side illuminated.

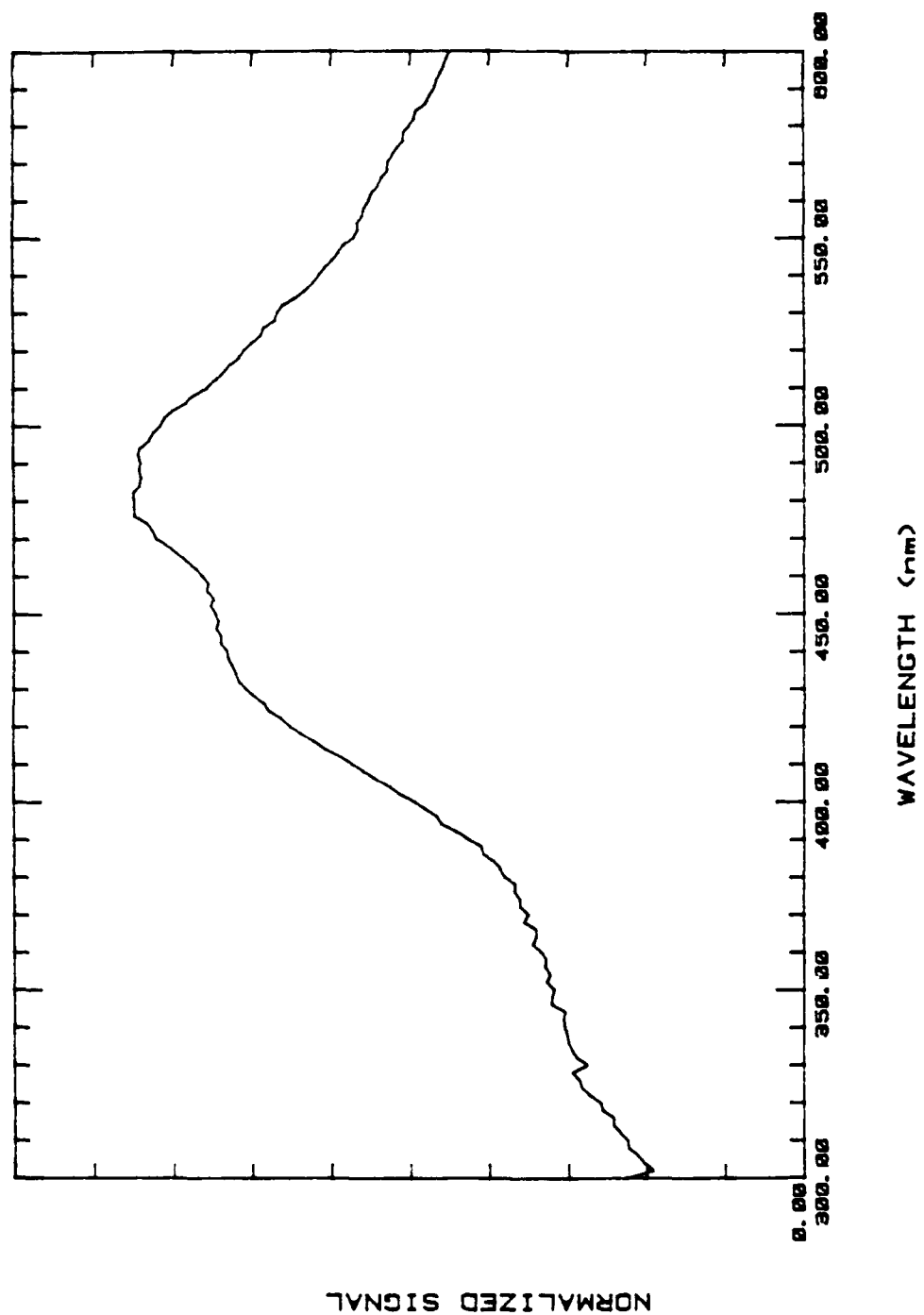


Figure 69. Pyroelectric response for sample 9/10A, an  $O^+$ ,  $C^+$  dual implant, implanted side illuminated.

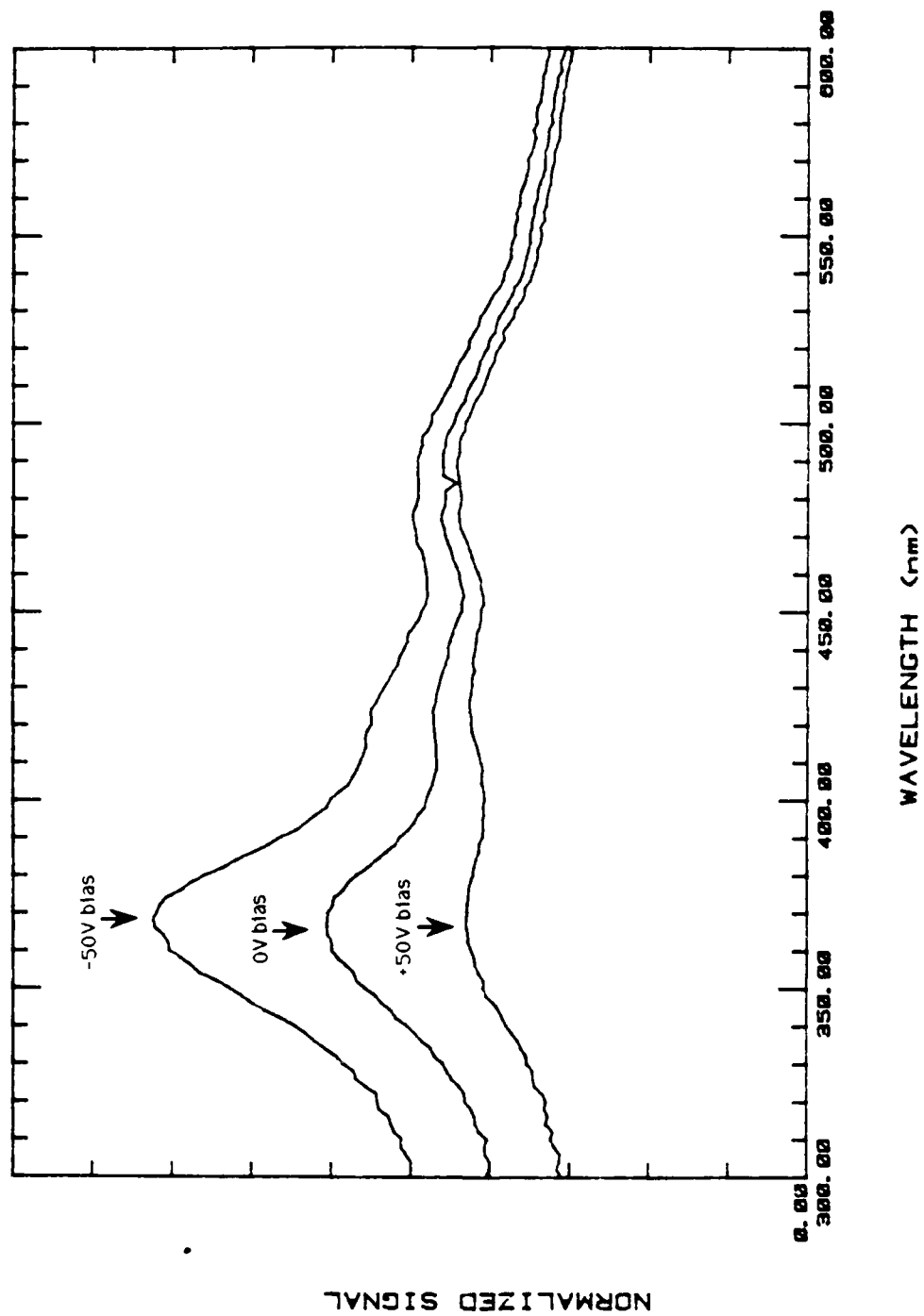


Figure 70. Photoconductivity-mode spectrum of sample 9/10B, an  $O^{3+}$ ,  $C^{+}$  dual-implant, nonimplanted side illuminated.

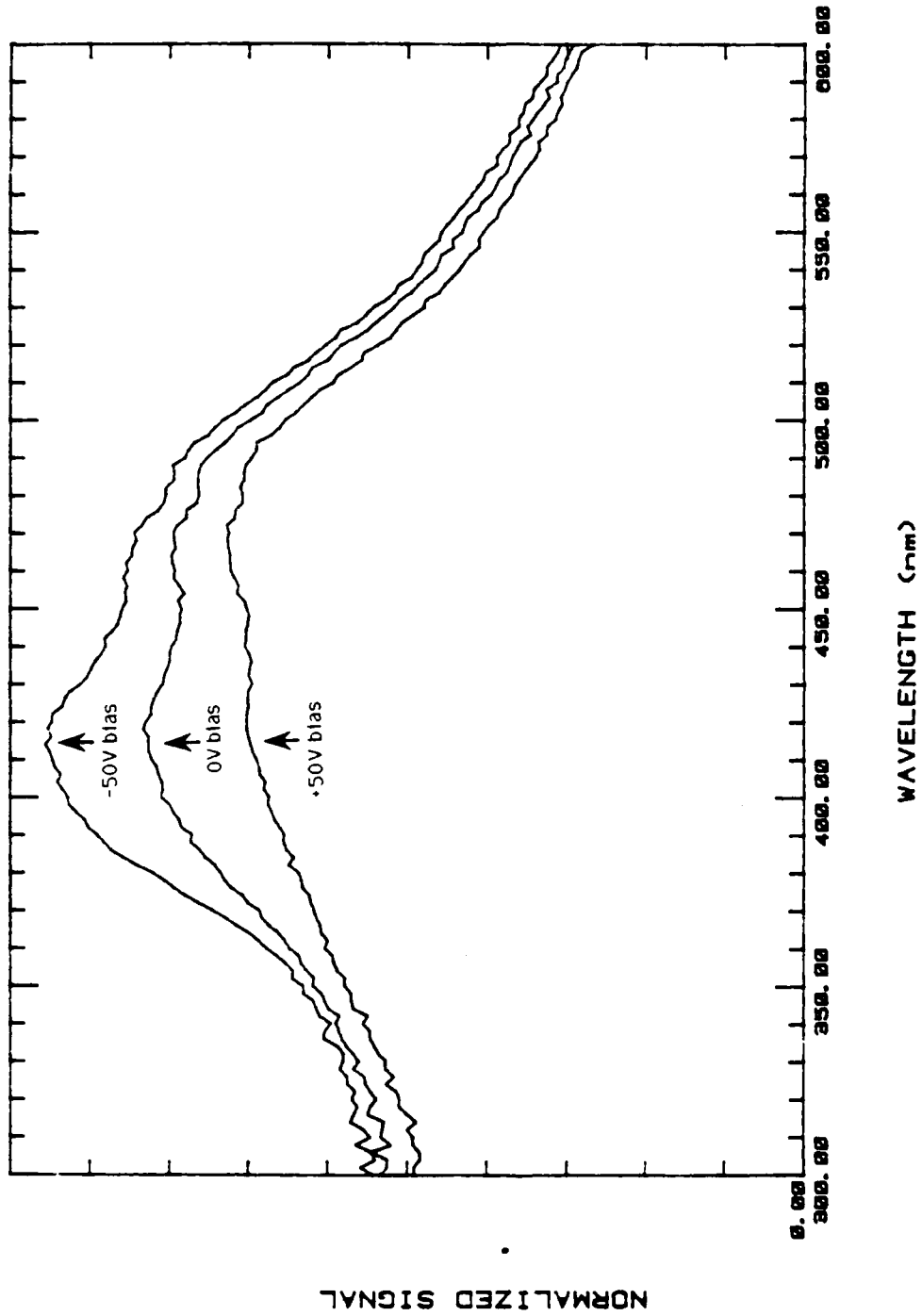


Figure 71. Photoconductivity-mode spectrum of sample 9/10B, an  $O^{3+}$ ,  $C^{+}$  dual-implant, implanted side illuminated.

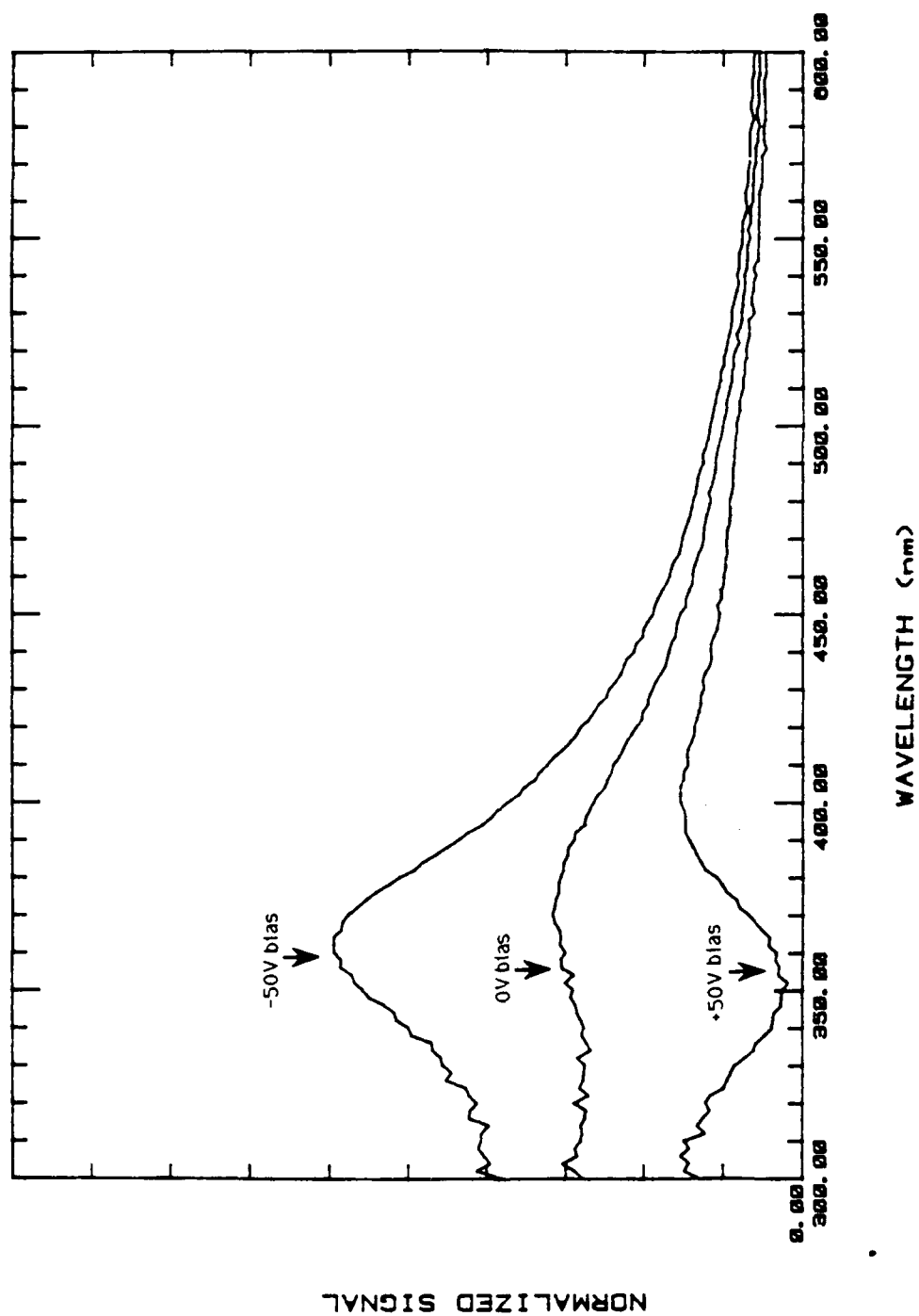


Figure 72. Photoconductivity-mode spectrum of sample 9/21B, a triple-Ni<sup>+</sup> implant, nonimplanted side illuminated.

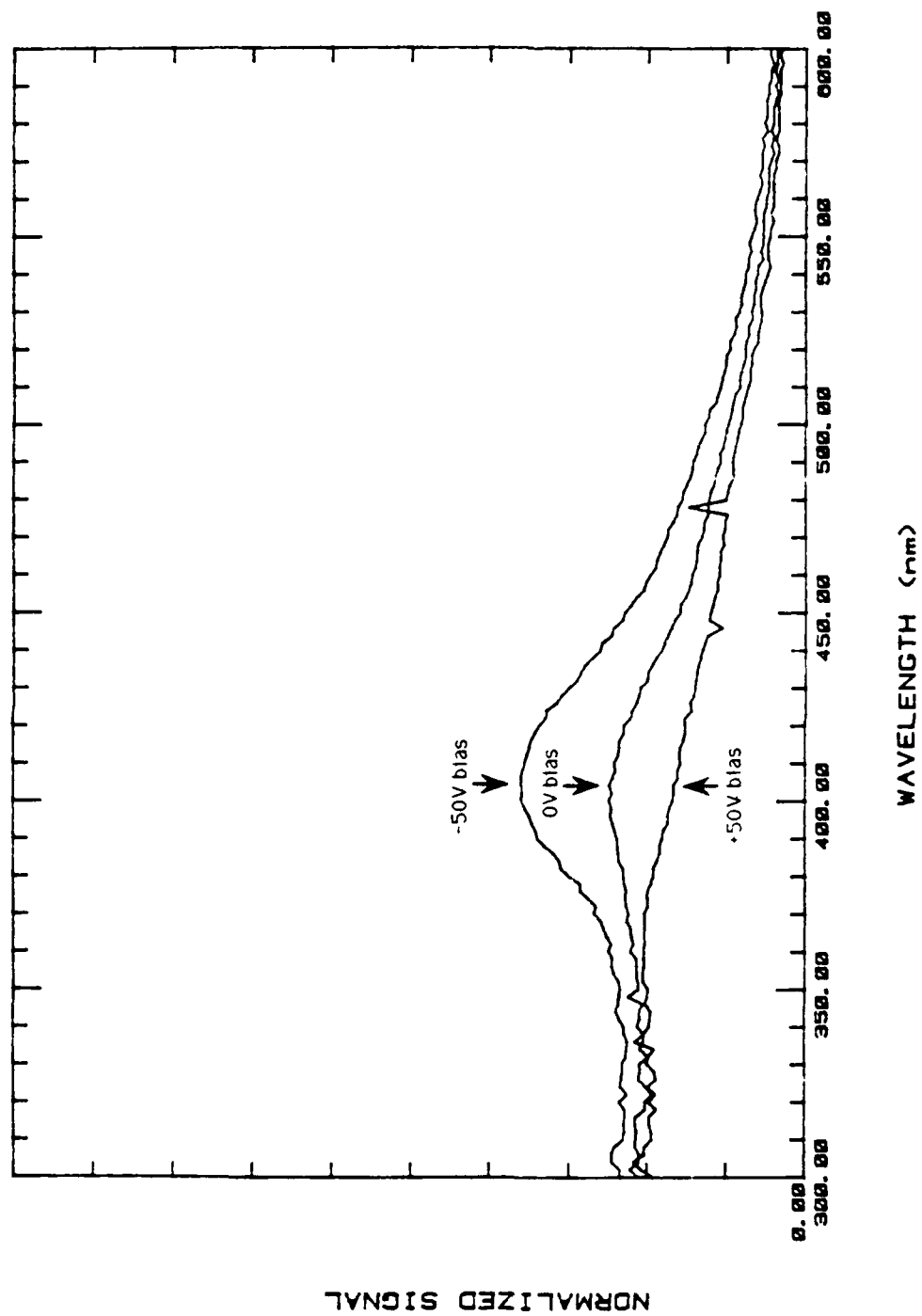


Figure 73. Photoconductivity-mode spectrum of sample 9/21B, a triple-Ni<sup>+</sup> implant, implanted side illuminated.



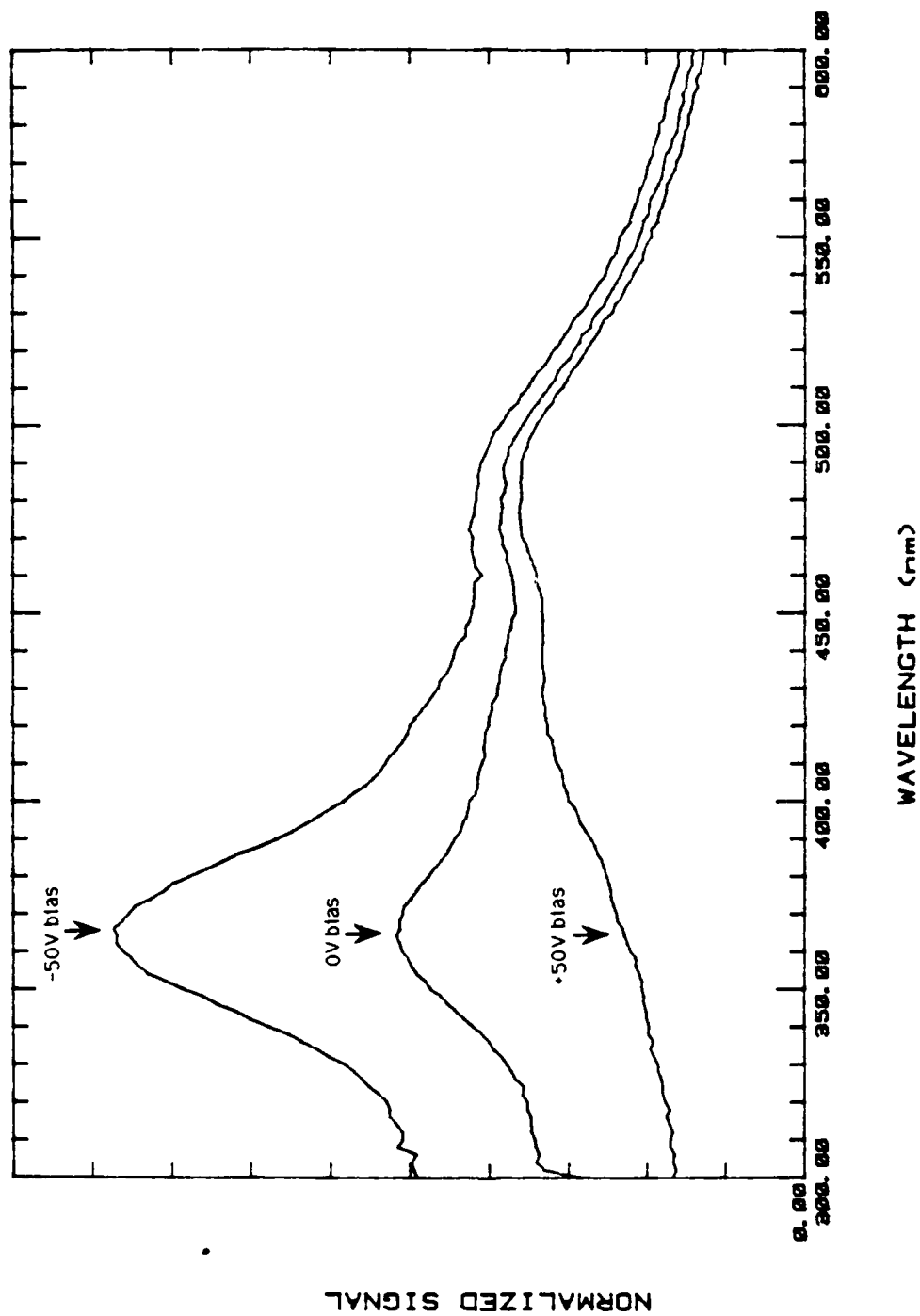


Figure 74. Photoconductivity-mode spectrum of sample 9/18B, an  $\text{Ne}^+$ ,  $\text{Ni}^+$  dual-implant, nonimplanted side illuminated.

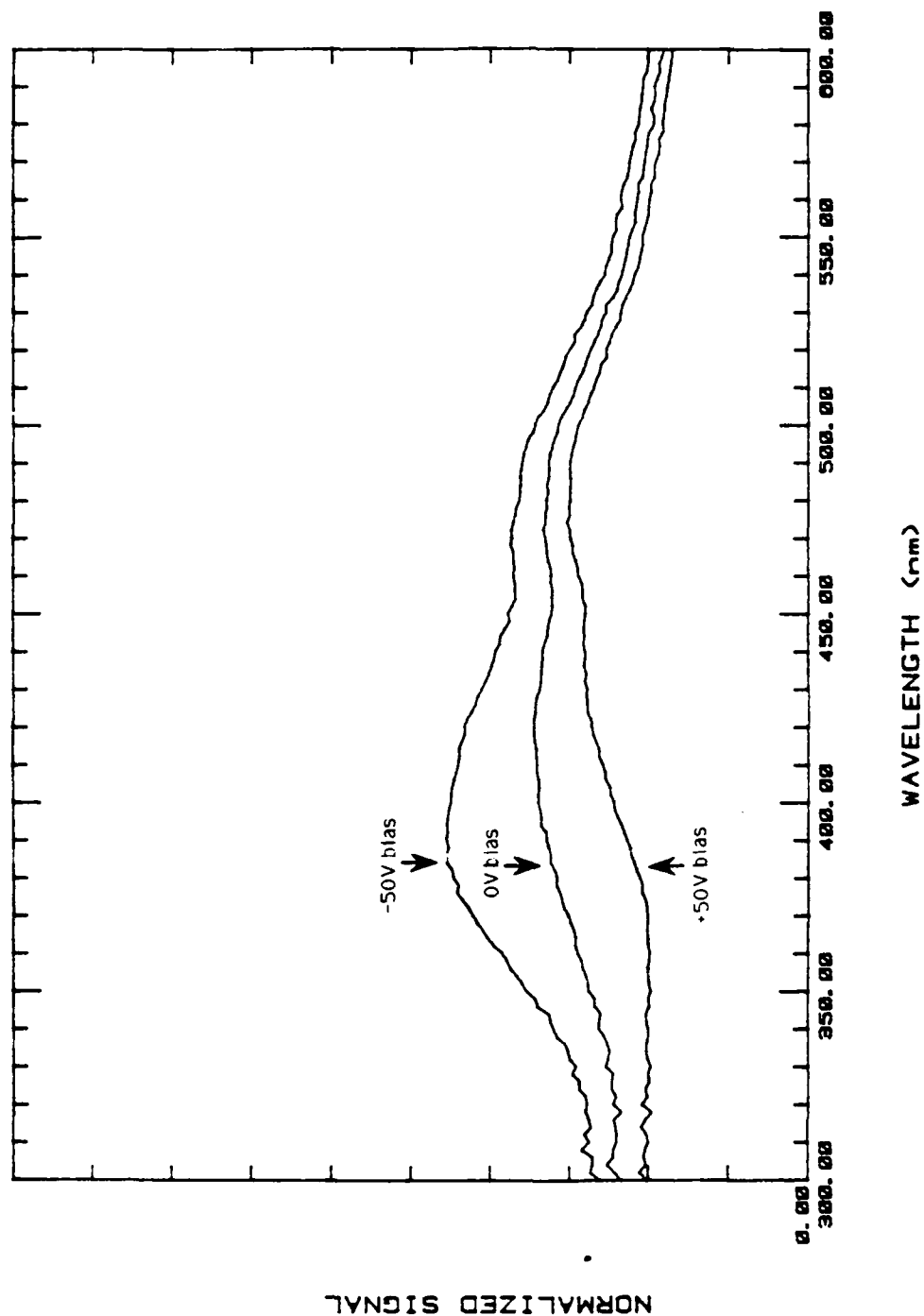


Figure 75. Photoconductivity-mode spectrum of sample 9/18B, an  $\text{Ne}^+$ ,  $\text{Ni}^+$  dual-implant, implanted side illuminated.

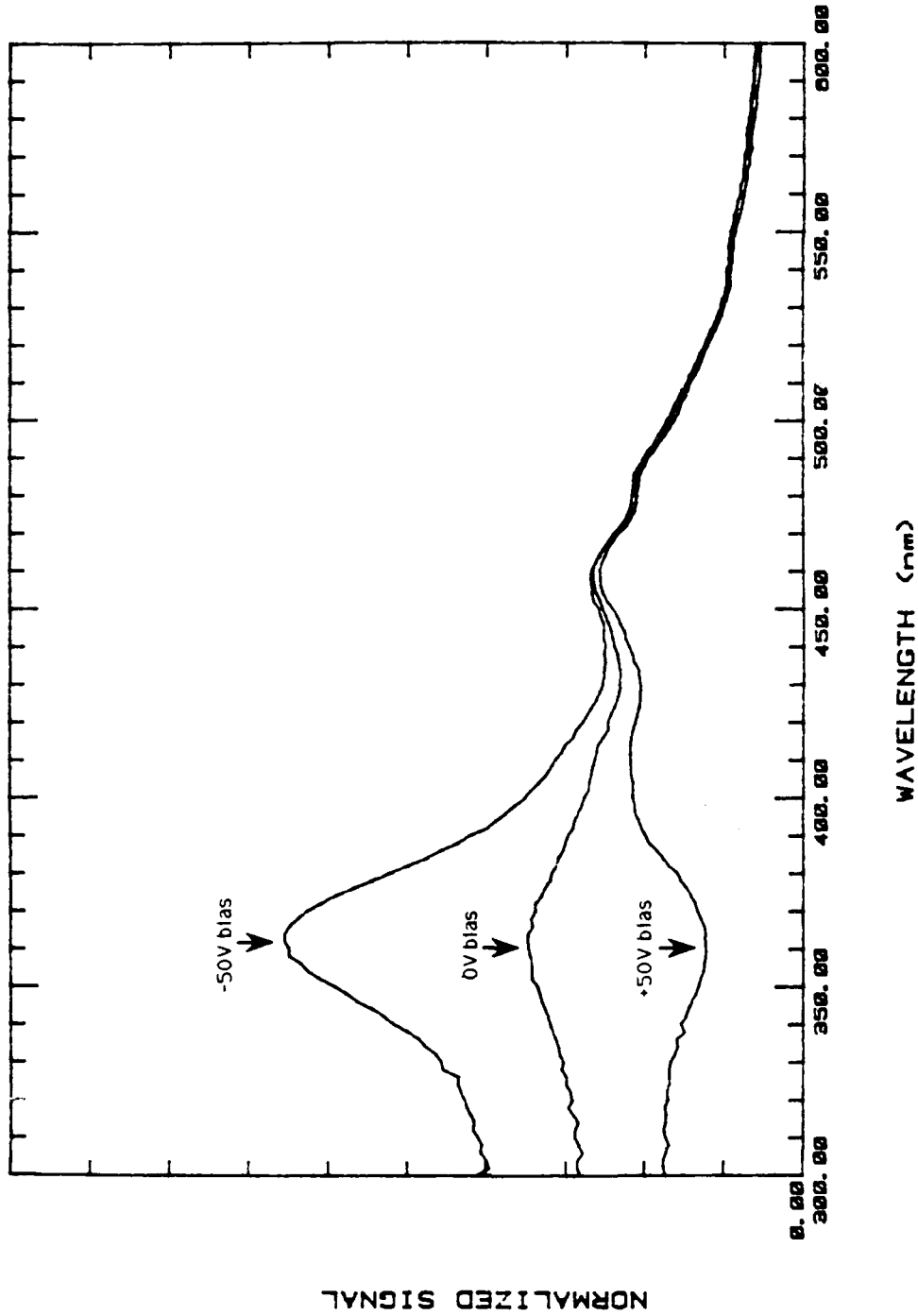


Figure 76. Photoconductivity-mode spectrum of sample 9/10A, an  $O^+$ ,  $C^+$  dual-implant, nonimplanted side illuminated.

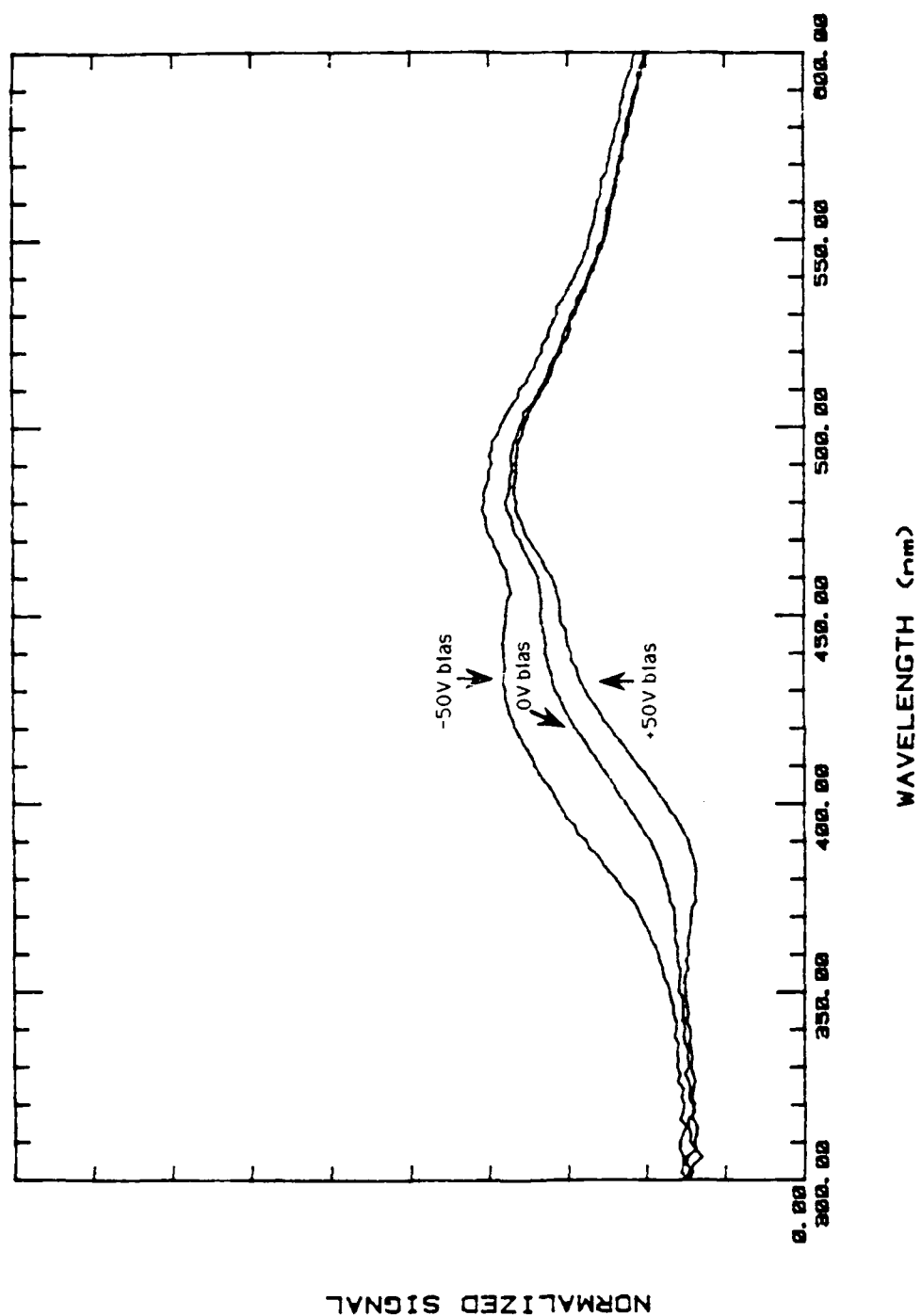


Figure 77. Photoconductivity-mode spectrum of sample 9/10A, an  $O^+$ ,  $C^+$  dual-implant, implanted side illuminated.

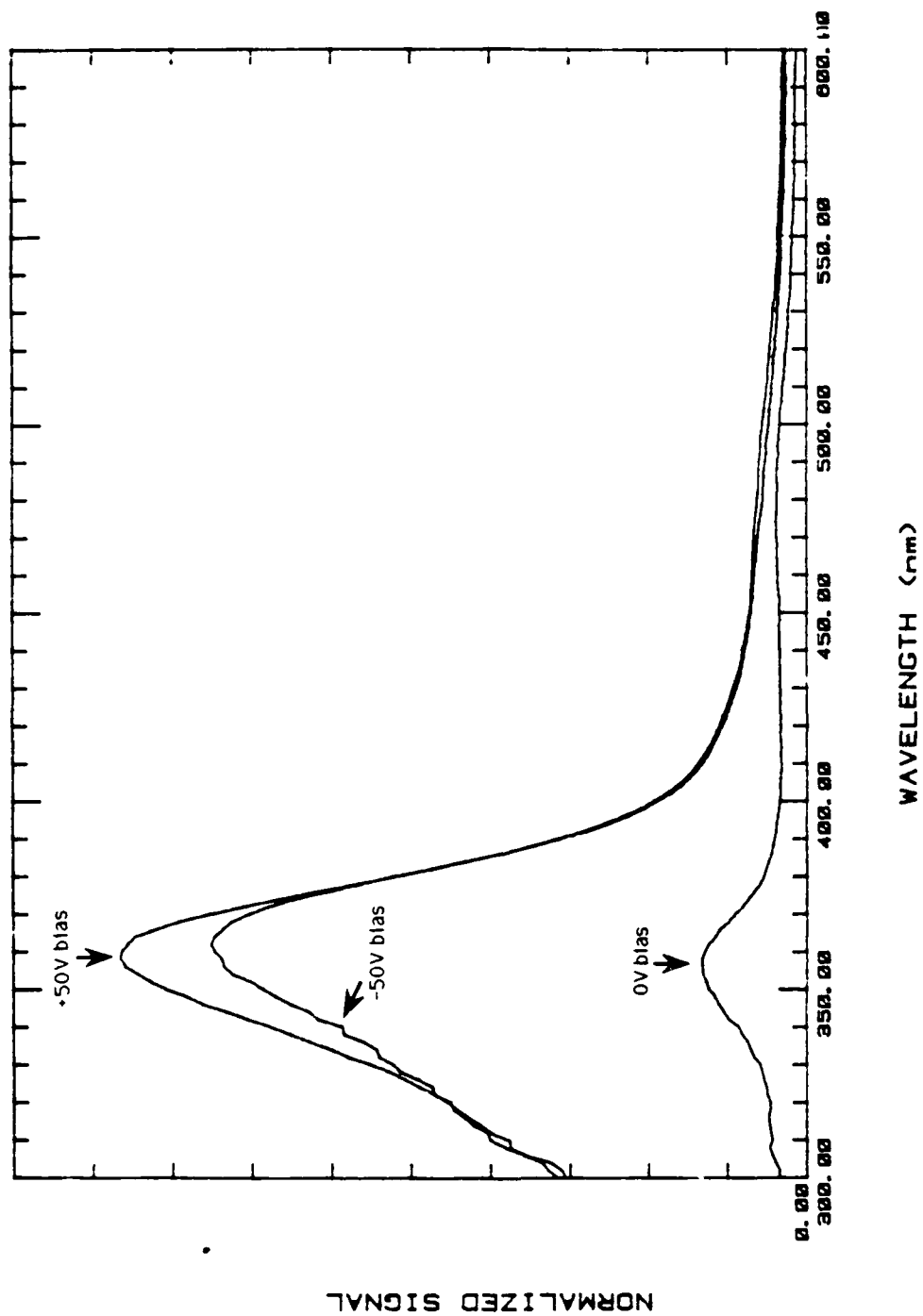


Figure 78. Photoconductivity-mode spectrum of virgin PLZT sample 7/51, lock-in amplifier set for autophase.

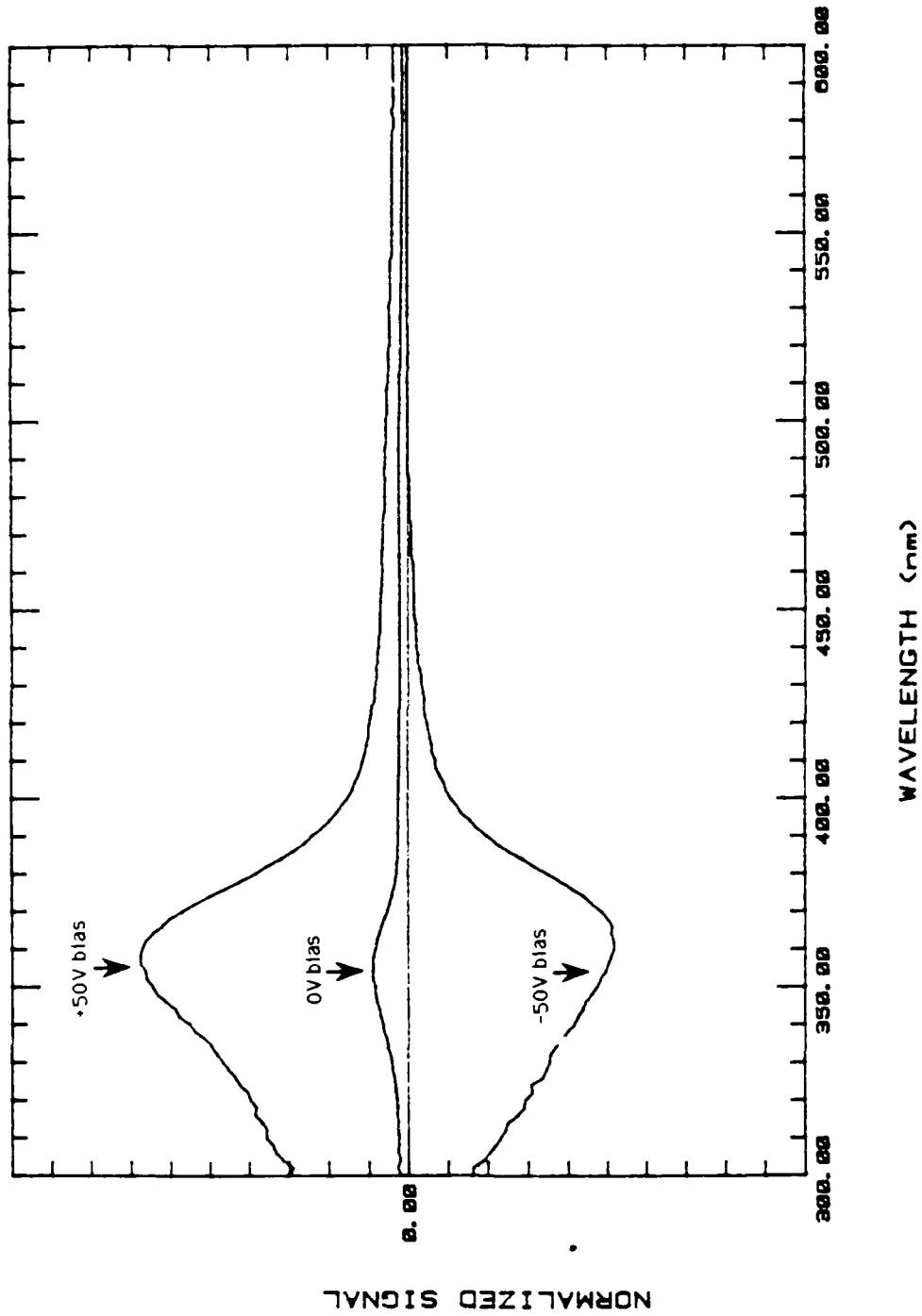


Figure 79. Photoconductivity-mode spectrum of virgin PLZT sample 7/51, not set for autophase.

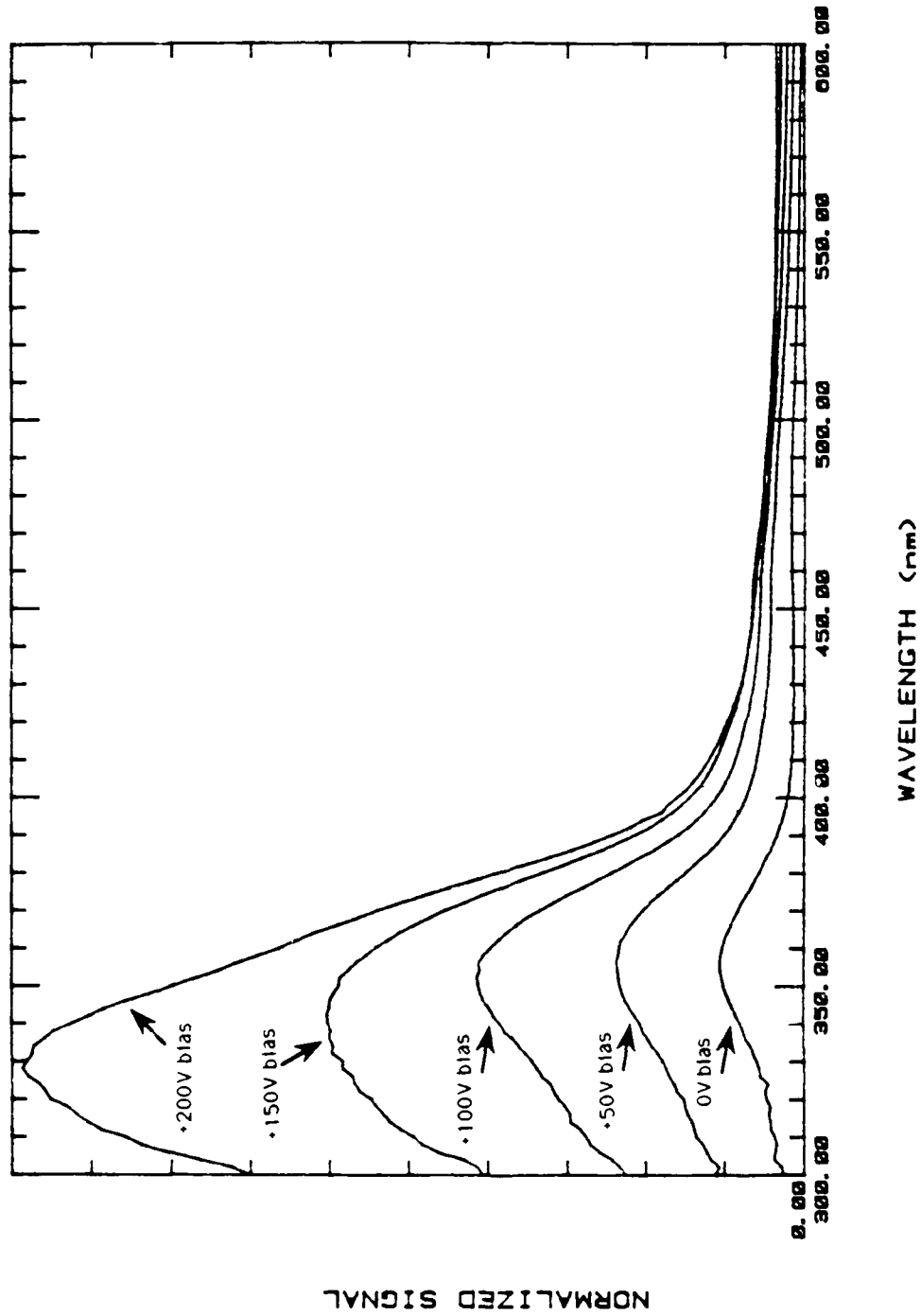


Figure 80. Photoconductivity-mode spectrum of virgin PLZT sample 1/51 as a function of bias voltage.

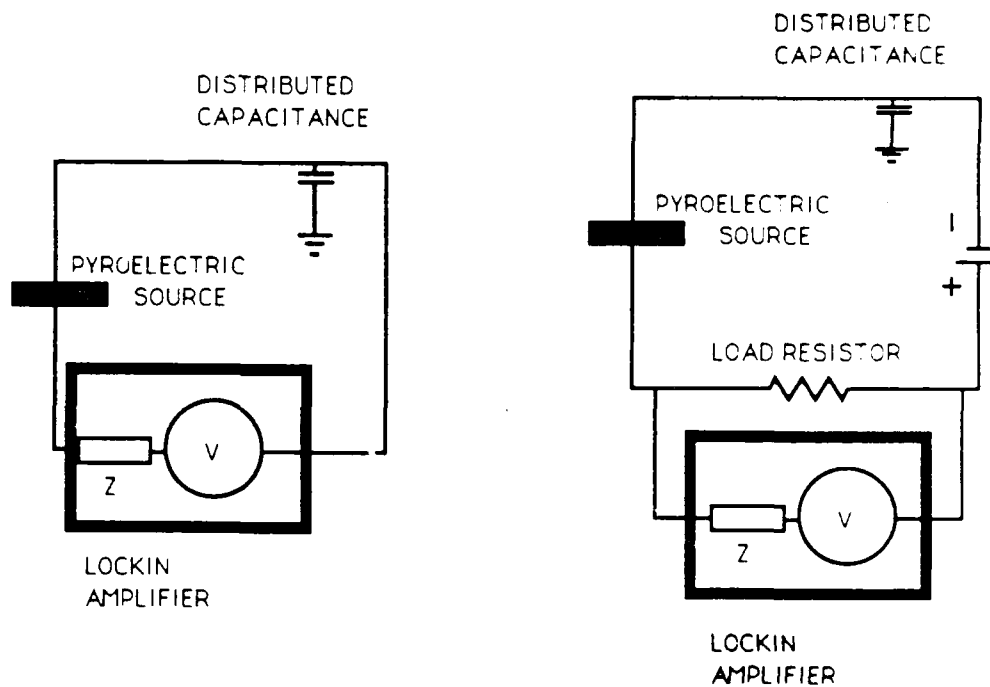


Figure 81. Electrical setup for pyroelectric and photoconductivity-mode measurements.



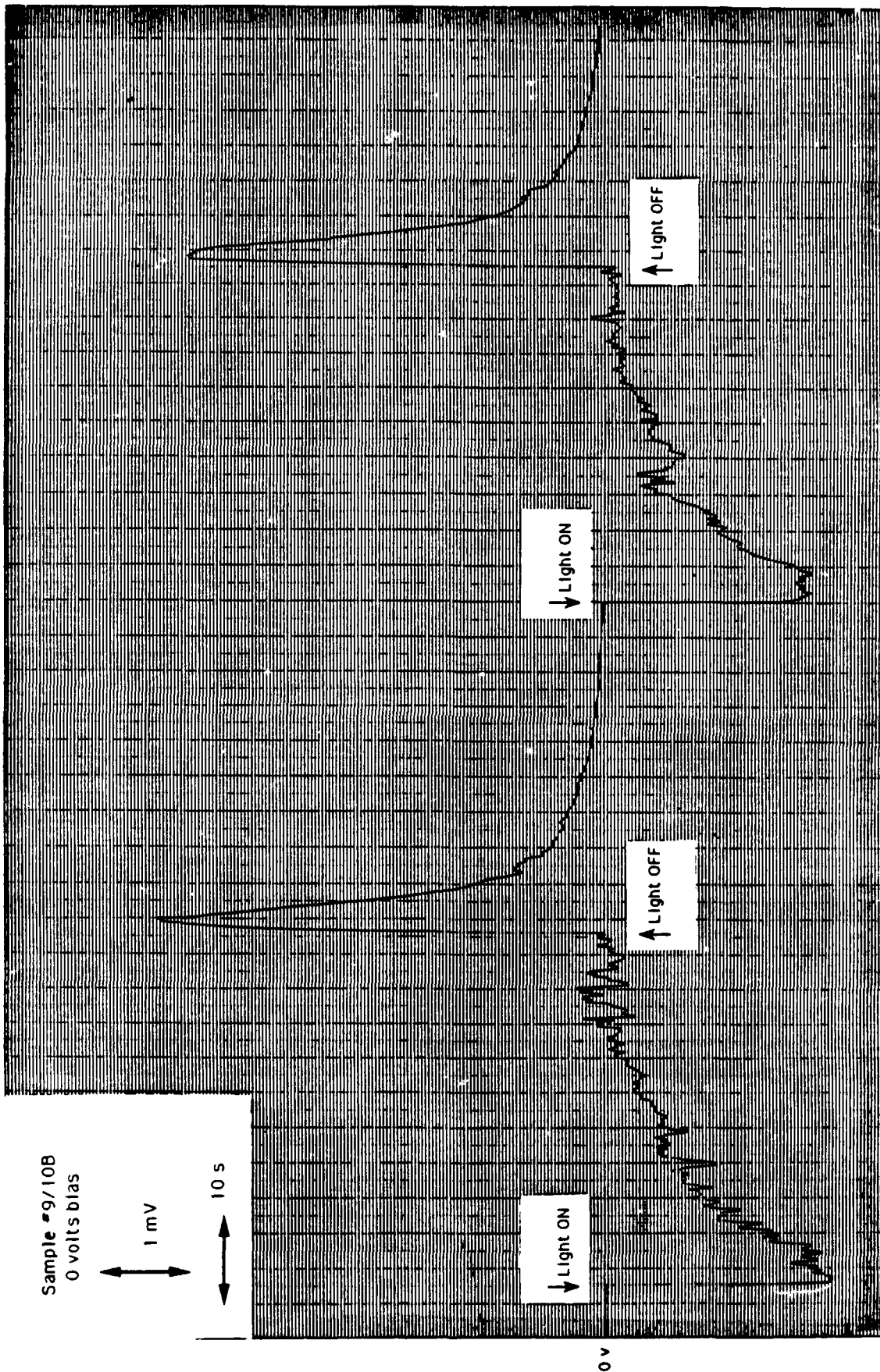
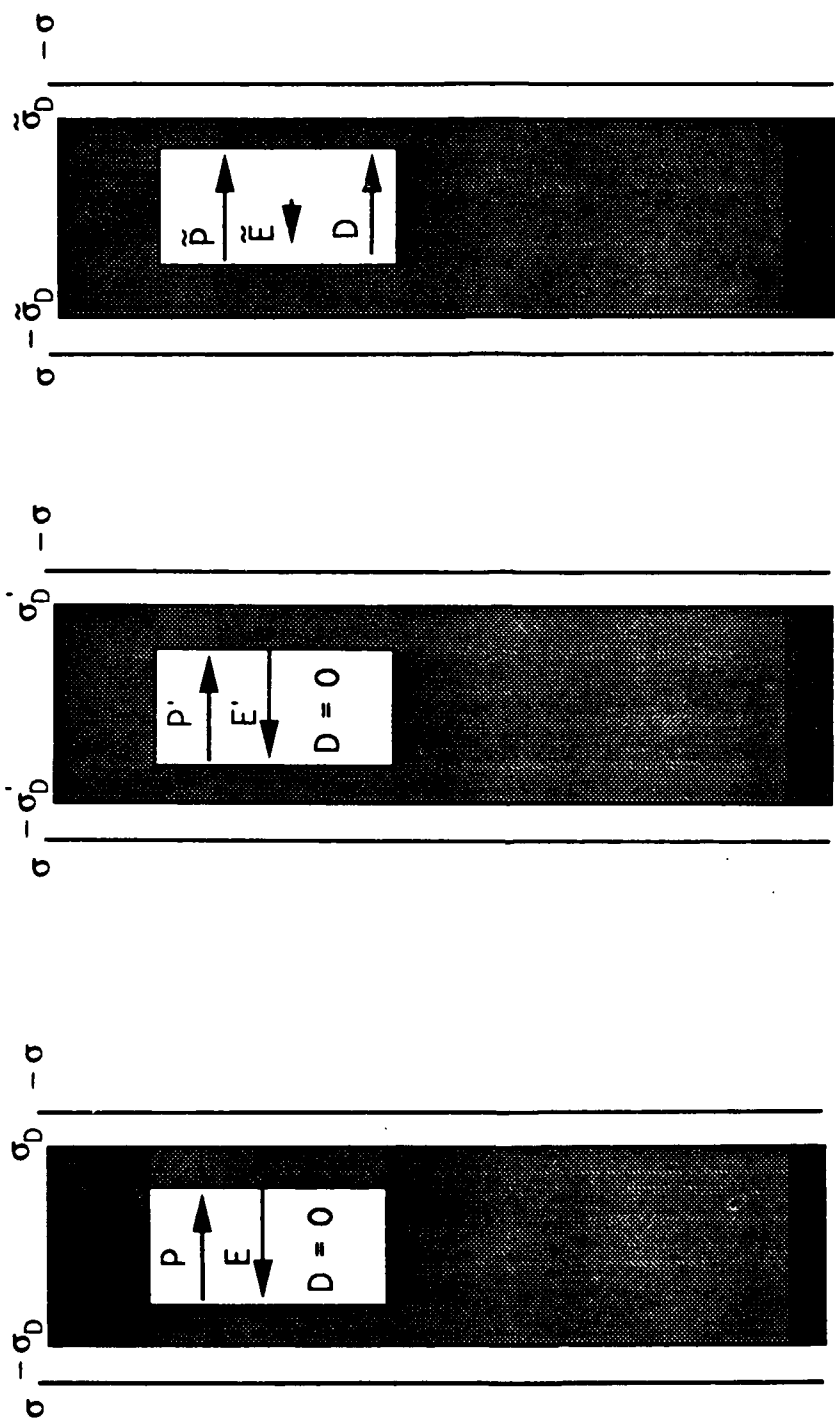


Figure 82. DC-photoconductivity signal for sample 9/10B at 488 nm.



(a) Sample in equilibrium. (b) Sample absorbing light. (c) Biased sample.

Figure 83. Source of pyroelectric response.

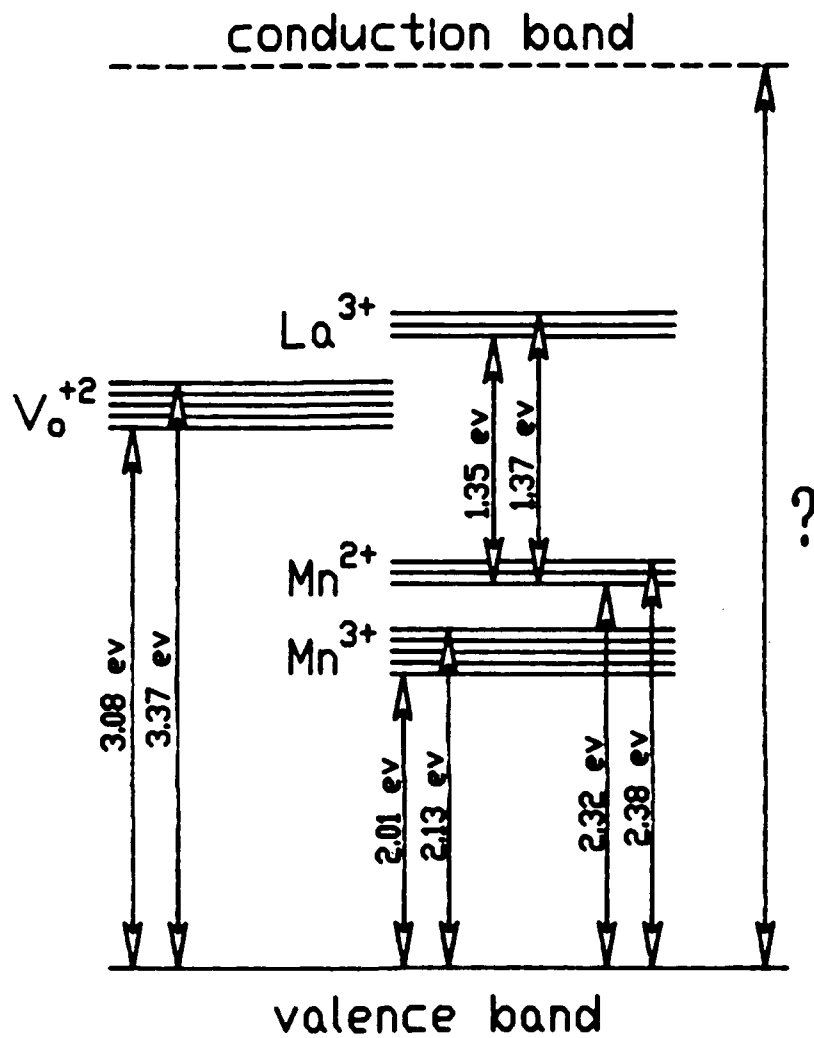


Figure 84. Result of doping PZT with La and Mn (Ref. 7).

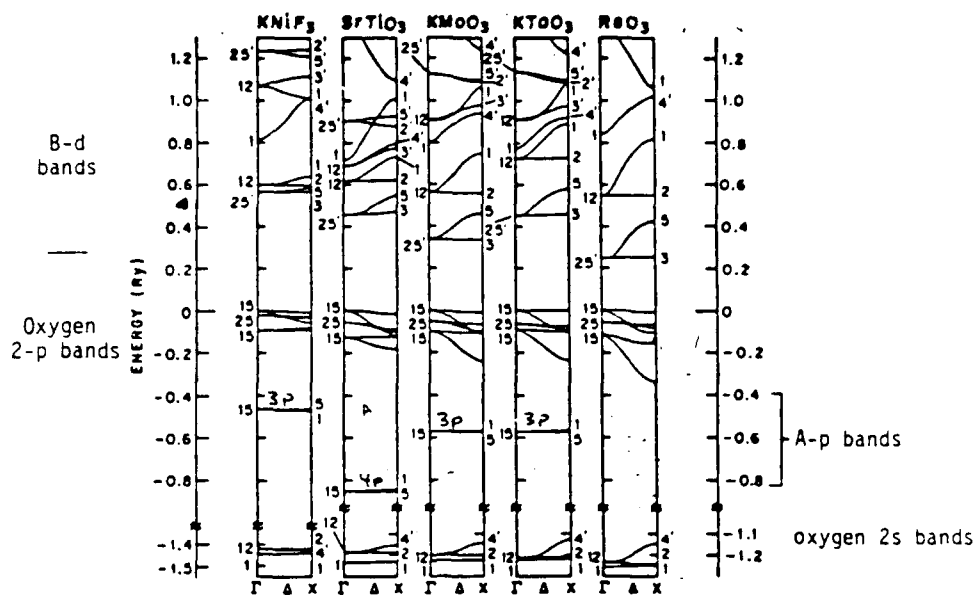


Figure 85. APW results along the line for several perovskite-type compounds and  $\text{ReO}_2$ . The energy scale to the lower left-hand side is for  $\text{KNiF}_3$ , the one to the lower right-hand side is for the oxide compounds.

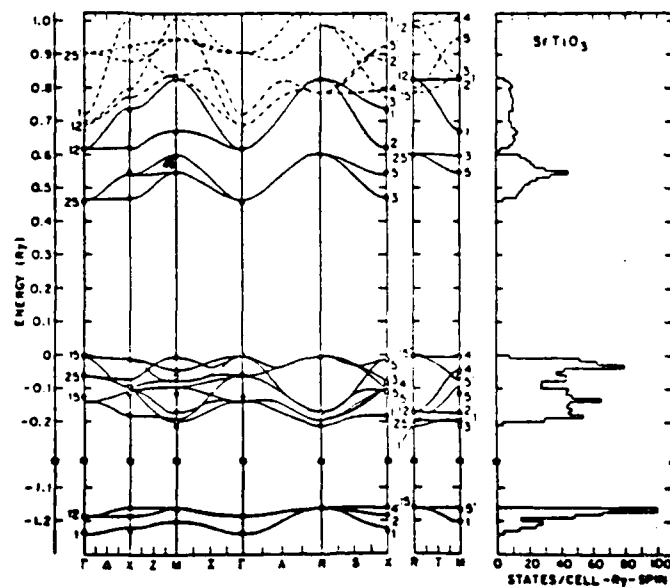


Figure 86. LCAO band structure and density of states for  $\text{SrTiO}_3$ .

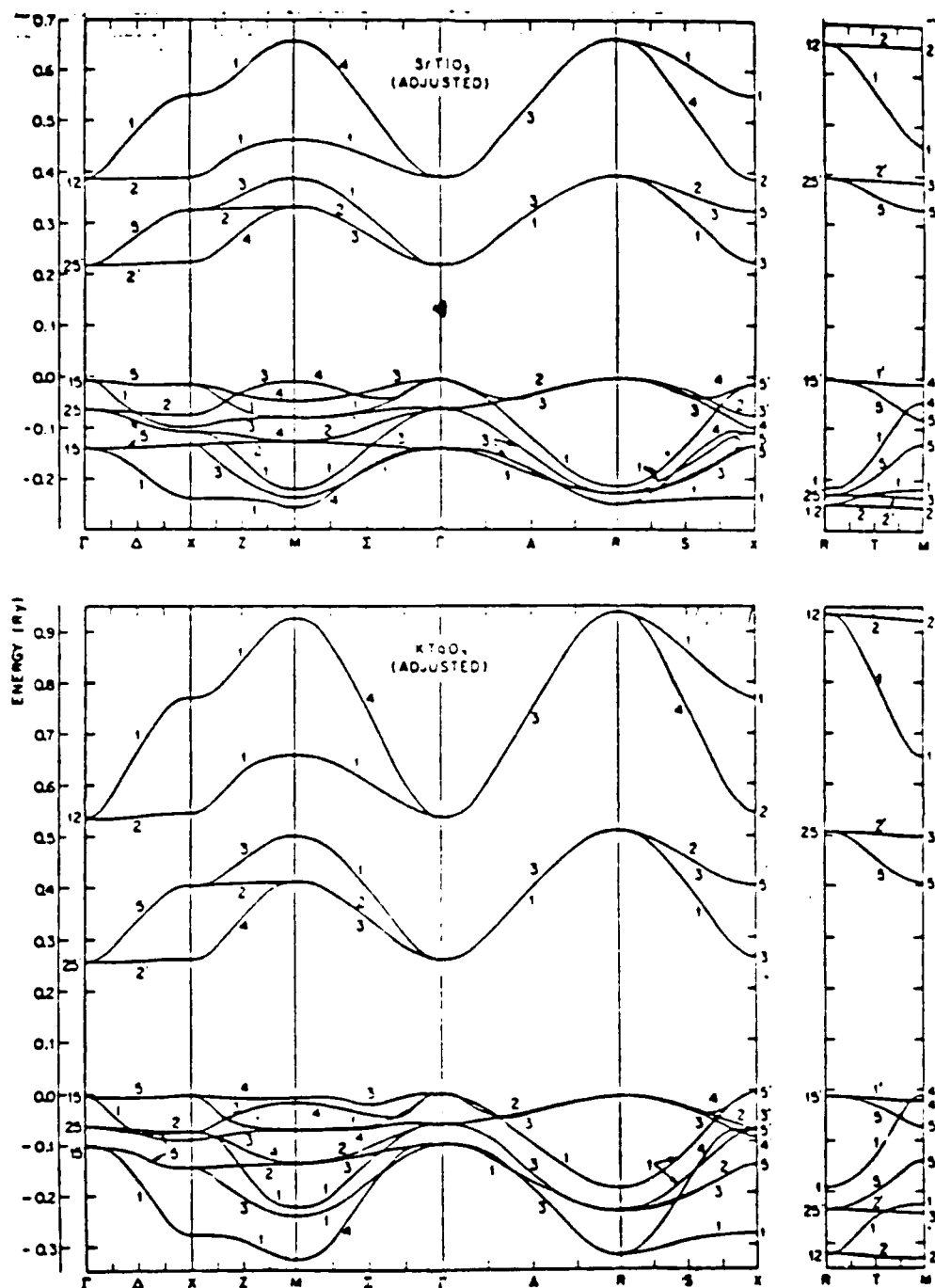


Figure 87. Adjusted LCAO band structures for  $\text{SrTiO}_3$  and  $\text{KTaO}_3$  (adjusted to include optical and cyclotron resonance results).

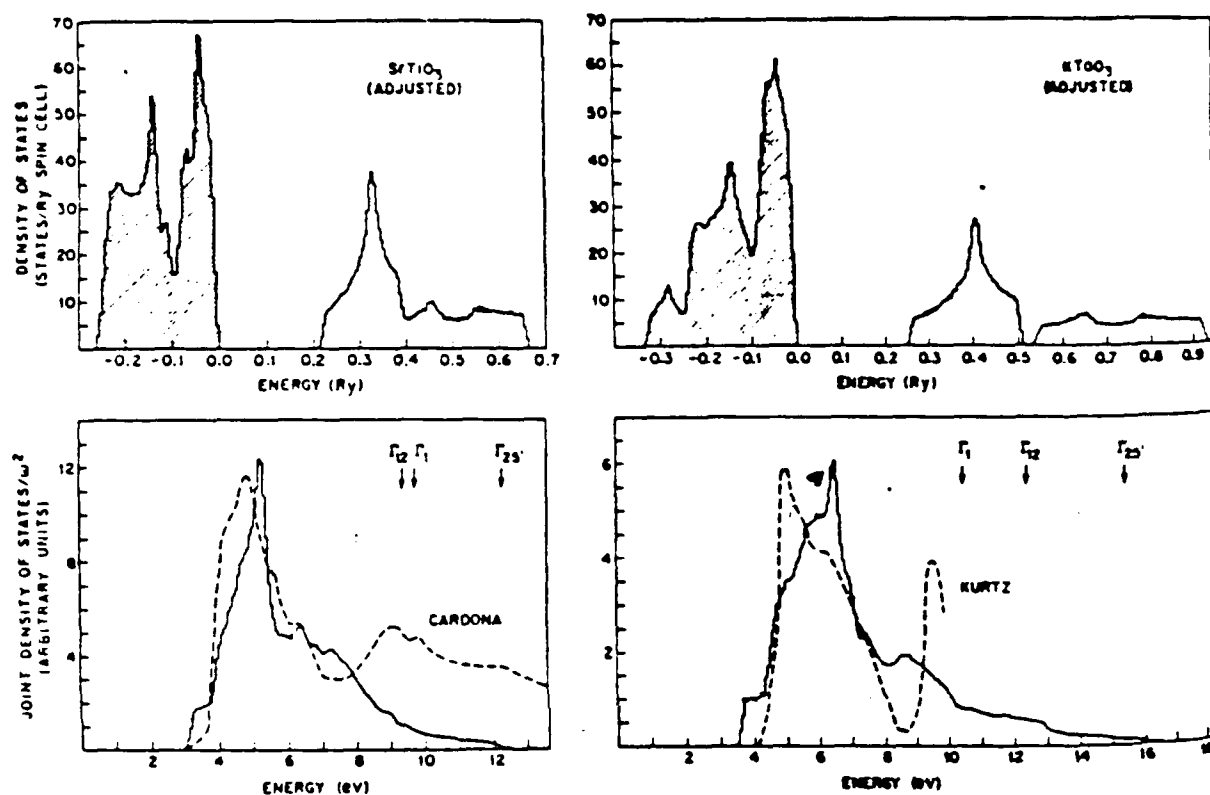


Figure 88. Density of states and joint density of states curves for the adjusted LCAO band-structure models for  $\text{SrTiO}_3$  and  $\text{KTaO}_3$  and a comparison with the experimental  $\epsilon_2$  (dashed curves).

lead 5d-states, etc.

(zirconium, titanium) d-states

oxygen 2p-states

lead 5p-states

oxygen 2s-states

Figure 89. Conceptual model for density of electronic states of PZT.

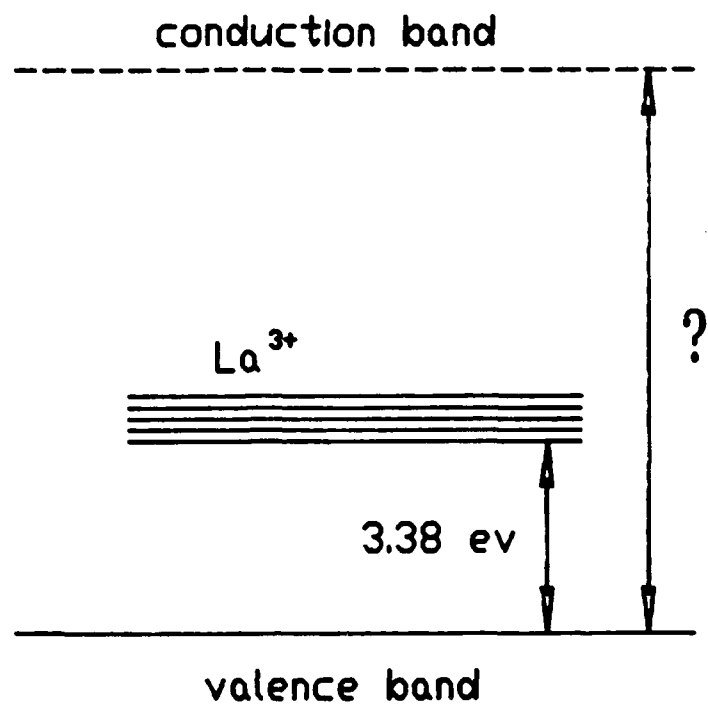


Figure 90. Results for doping PZT with La (Mn removed) (Ref. 7).



PLZT 7/65/35 -- SAMPLE #9/11  
 UNIMPLANTED, UNELECTRODED WAFER  
 FILE --P9/11

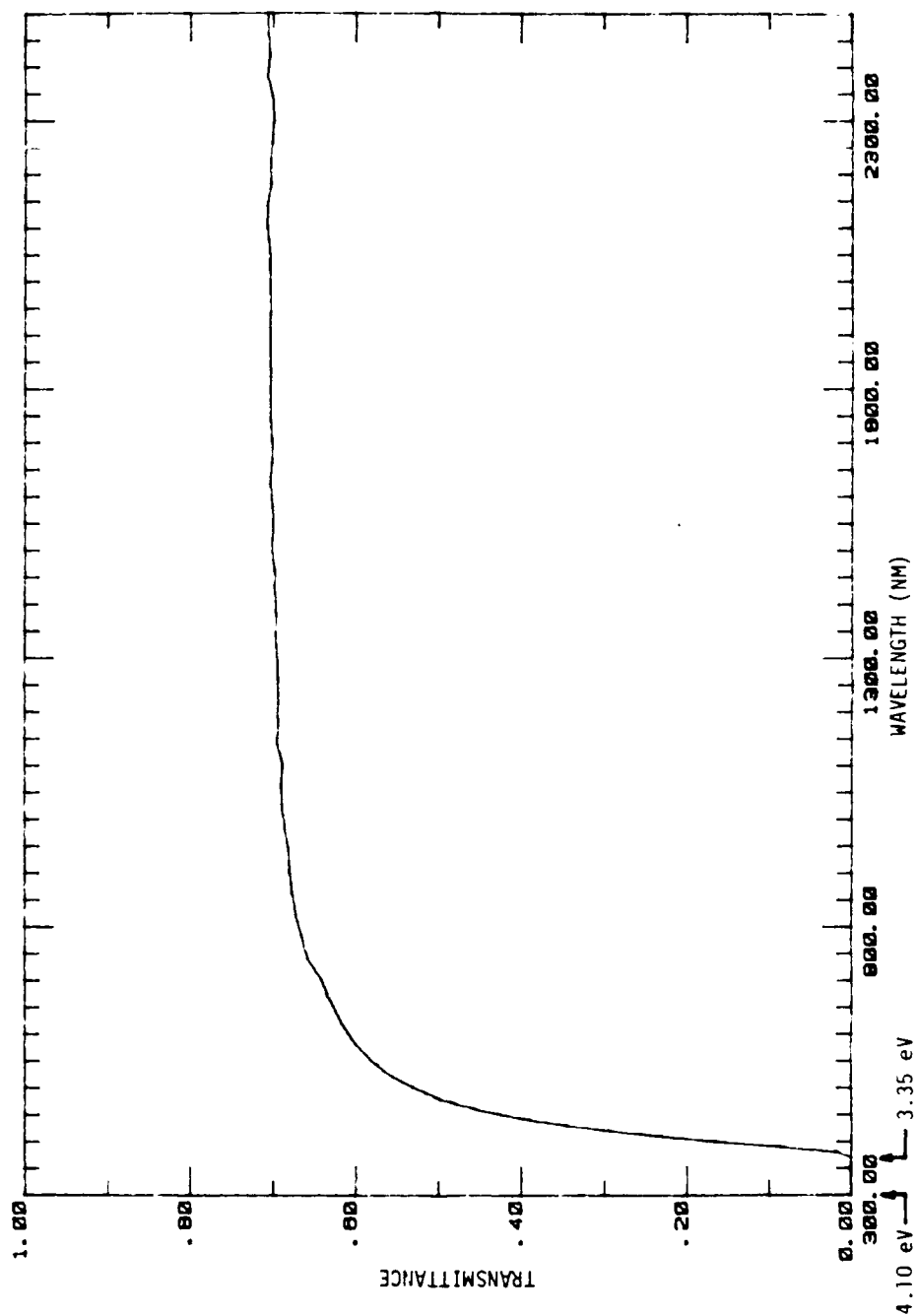
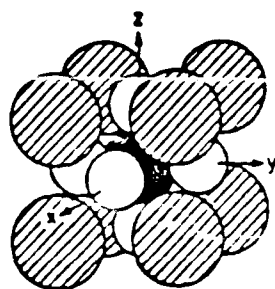
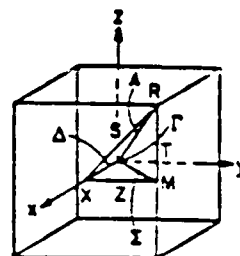


Figure 91. Spectral transmittance of unimplanted PLZT.



(a) Unit cell for the perovskite-type ABC compounds, where the A atoms are shaded, the B atom is filled, and the C atoms are unshaded.



(b) Brillouin zone for the simple cubic Bravais lattice  
For PZT: A = Pb; B = Zr, Ti; C = O.

Figure 92. PZT structure.

# REFERENCES

1. Peercy, P. S. and Land, C. E., "A Model for Ion-Implantation-Induced Improvements of Photoferroelectric Imaging in Lead Lanthanum Zirconate/Titanate Ceramics." Applied Physics Letters 37:815, 1980.
2. Land, C. E. and Peercy, P. S., "A Review of the Effects of Ion Implantation on the Photoferroelectric Properties of PLZT Ceramics." Ferroelectrics 45, 25, 1982. (See also references therein.)
3. Land, C. E., "Photosensitivity and Imaging Characteristics of Ion-Implanted PLZT Ceramics." Proceedings of the Sixth International Meeting on Ferroelectricity, Kobe, 1985; Japanese Journal of Applied Physics 24, Suppl. 24-2, 134, 1985. (See also references therein.)
4. DeHainaut, C., Bullington, J., Mills, R., Carter, R., and Mancha, S., "Holographic correction of aberrations in collimated laser beams using PLZT." SPIE, Spatial Light Modulators and Applications II 825:198, 1987.
5. Manning, I. and Mueller, G., "Depth Distribution of Energy Deposition by Ion Bombardment," Comp. Phys. Comm., Vol. 7, p. 85, 1974.
6. Pawlewicz, W. T., Martin, P. M., Knoll, R. W., and Mann, I.B., "Multilayer Optical Coating Fabrication by DC Magnetron Reactive Sputtering Techniques." SPIE Proceedings, Volume 678, 1986.
7. van der Pauw, L. J., A Method of Measuring Specific Resistivity and Hall Effect of Discs of Arbitrary Shape. Philips Research Reports 13, 1, Philips Research Co., Eindhoven, Netherlands 1958.
8. Kala, T., "Study of the Influence of Manganese and Lanthanum Oxides on the Band Structure of Pb (Zr,Ti)O<sub>3</sub>." Phys. Stat. Sol. (a) 73, 573, 1982.
9. Haertling, G. H. and Land, C. E., "Hot-Pressed (Pb, La) (Zr,Ti)O<sub>3</sub> Ferroelectric Ceramics for Electrooptic Applications," J. Am. Cer. Soc., Vol. 54, No. 1, pp. 1-11, January 1971.
10. Hoffman, R. W. "Mechanical Properties of Non-Metallic Thin Films," in Physics of Non-Metallic Thin Films, Plenum Press, New York, p. 309, 1974.
11. Glang, R., Holmwood, R. A., and Rosenfeld, R. L., "Determination of Stress in Thin Films on Single Crystal Substrates." Review of Scientific Instruments 36(1):7.
12. Manifacier, J. C., Gasiot, J., and Fillard, J. P., "A Simple Method for the Determination of the Optical Constants n, k and the Thickness of a Weakly Absorbing Thin Film." Journal of Physics E9, 1002, 1976.
13. Jacobsson, R., "Inhomogeneous and Coevaporated Homogeneous Films for Optical Applications," Physics of Thin Films, Vol. 8, Academic Press, New York, 1975.

# REFERENCES (Concluded)

14. Seager, C. H., and Land, C. E., "Optical absorption in ion- implanted lead lanthanum zirconate titanate." Applied Physics Letters, 45(4)-:395, 1984.
15. Ashcroft, N. W., and Mermin, N. D., "Solid State Physics." Holt, Rinehart, and Winston, Philadelphia, 1976.
16. Moretti, F., and Michel-Calendini, F. M., "Impurity Energy Levels and Stability of Cr and Mn Ions in Cubic BaTiO<sub>3</sub>." Phys. Rev. B 36, p. 3522, 1987.
17. Jaffe, B., Cooke, W. R., and Jaffe, H., "Piezoelectric Ceramics." Academic Press, London, 1971.
18. Holman, R. L., "The Defect Structure of 8/65/35 PLZT As Determined by Knudsen Effusion." Ferroelectrics 10, p. 185, 1976.
19. Okazaki, K. M. Masuda, Tashiro, S., and Ishibashi, S., "Defect Structure and Properties of Electro-Optic PLZT Ceramics." Ferroelectrics 22, p. 681, 1978.
20. Mattheiss, L. F., "Energy Bands for KNiF<sub>3</sub>, SrTiO<sub>3</sub>, KMoO<sub>3</sub>, and KTaO<sub>3</sub>." Phys. Rev. B 6, p. 4718, 1972.
21. Wolfram, Phys. Rev. Lett., Vol. 29, p. 1383, 1972.

# ACRONYMS

APW	Augmented-Plane-Wave
dpa	displaced atoms
EDEP	Energy Deposition
EDX	Energy Dispersive X-ray
ITO	Indium Tin Oxide
LCAO	Linear Combination of Atomic Orbitals
MSRC	Molecular Sciences Research Center
MTF	Modulation Transfer Function
NBS	National Bureau of Standards
NIR	Near Infrared Region
PLZT	Lead, Lanthanum, Zirconate, Titanate
PNL	Pacific Northwest Laboratory
PZT	Lead Zirconate Titanate
SNL	Sandia National Laboratory
TEM	Transmission Electron Microscope
WL	Weapons Laboratory